ISSN number 0971 - 9709

IGU
Promoting Earth System Sciences

The Journal of Indian Geophysical Union

AN OPEN ACCESS BIMONTHLY JOURNAL OF IGU

VOLUME 28, ISSUE 5, SEPTEMBER 2024

EDITORIAL OFFICE

Indian Geophysical Union, NGRI Campus, Uppal Road, Hyderabad- 500 007

Telephone: 91-4027012739, 27012332; Telefax:+91-04-27171564

Email: jigu1963@gmail.com, website: http://iguonline.in/journal/

The Journal with six issues in a year publishes articles covering

Solid Earth Geosciences; Marine Geosciences; and Atmospheric, Space and Planetary Sciences.

The Journal is Financially supported by MoES, Govt. of India.

Annual Subscription

Individual Rs -1000/- per issue and Institutional Rs- 5000/- for six issues

Payments should be sent by DD drawn in favour of "The Treasurer, Indian Geophysical Union", payable at Hyderabad,

Money Transfer/NEFT/RTGS (Inter-Bank Transfer), Treasurer, Indian Geophysical Union, State Bank of India, Habsiguda Branch,

Habsiguda, Uppal Road, Hyderabad- 500 007

A/C: 52191021424, IFSC Code: SBIN0020087, MICR Code: 500002318, SWIFT Code: SBININBBHO9.

For correspondence, please contact, Hon. Secretary, Indian Geophysical Union, NGRI Campus, Uppal Road,

Hyderabad - 500 007, India; Email: igu123@gmail.com; Ph: 040 27012332

ISSN: 0257-7968 (Clarivate Analytics)
ISSN: 0971-9709 (NISCAIR)
Approved as bimonthly ESCI journal by Clarivate Analytics
Cited in Indian Citation Index (ICI), New Delhi
Evaluated by NISCAIR, New Delhi
UGC Approved Journal

CONTENTS

Research Articles

J. Ind. Geophys. Union, 28(5) (2024), 300-313

Magnetic fabric characteristics of earthquake induced deformation features around Dauki region, Shillong Plateau, India

Md. Mujahed Baba[1,2], B.V. Lakshmi[1*], K. Deenadayalan[1], Pradnya Mohite[1], V.M. Rokade[2], S.N. Patil[2] and A. P. Dimri[1]
[1]Indian Institute of Geomagnetism, New Panvel, Navi Mumbai- 410 218, India
[2] Kavayitri Bahinabai Chaudhari North Maharashtra University, Jalgaon- 425001 India
[*]Corresponding Author: lakshmi.bv@iigm.res.in

ABSTRACT

Characterization of earthquake induced deformational features (seismites) play a significant role in the interpretation of earthquake dynamics and related hazards. In the present study, anisotropy of magnetic susceptibility (AMS) measurements for seismites were carried out at four sites in and around Dauki Fault, Shillong Plateau to define characteristic AMS fabrics of seismites. Rock magnetic measurements show that the magnetite and hematite minerals contribute to AMS fabric. We observed that seismites are characterised by triaxial to prolate fabric shape with low shape parameter and high magnetic lineation values whereas, undeformed sediment layers show oblate shape. The N-S orientation of K_{max} is well developed at all the sites and it is aligned perpendicular to the E-W trending Dauki Fault, suggesting extensional setting. Further, the inferred extensional magnetic lineation from the present study is compatible with the normal faults under extensional stress conditions, predicted by earlier studies in Shillong Plateau. The AMS technique contributes significantly to paleoseismic records for characterising seismites.

Keywords: Seismites, Paleoseismic record, Anisotropy of magnetic susceptibility, Triaxial, Magnetic lineation, Shillong Plateau

INTRODUCTION

Anisotropy of magnetic susceptibility (AMS) is most extensively used in the detection of paleocurrent or wind directions, flow directions in magma, and compressional or extensional strains (MacDonald and Palmer, 1990; Basavaiah et al., 2010; Lakshmi et al., 2020; Li et al., 2020). Many of the works have been presented to decipher the deformational history of sediments in different tectonic regimes (Borradaile and Tarling, 1981; Rochette et al., 1992; Tarling and Hrouda, 1993; Hirt et al., 1995; Pares et al., 2007). Previous studies from extensional basins on the AMS fabric showed that the magnetic lineation (K_{max}) is generally parallel to the stretching direction and perpendicular to the normal faults (Sagnotti et al., 1994; Cifelli et al., 2004; Maffione et al., 2012; Caricchi et al., 2016). In fold-and-thrust belts, studies have clearly demonstrated that the K_{max} trends parallel to fold axes and orthogonal to the maximum horizontal shortening direction (Rochette et al., 1992; Porreca and Mattei, 2012; Caricchi et al., 2016; Li et al., 2020).

The studied region Shillong Plateau, is surrounded by seismogenic faults like Oldham, Dauki, Kopili and Dhubri in the North, South, East and West respectively **(**Figure 1) (Kayal et al., 2006). Shillong Plateau is characterised as a geologically complex and seismically active region. Bilham and England, (2001), opined that the 'pop-up' tectonics between the Dauki Fault and the Oldham Fault was responsible for the Assam earthquake. However many previous studies disagree with the presence of the Oldham Fault (Srinivasan, 2003; Rajendran et al., 2004; Islam et al., 2011a). Furthermore, the proposed Oldham Fault may be bounded to the north by the Shillong Plateau. The uplift of the Shillong Plateau has been attributed by some workers to the India-Eurasia collision, and the resulting N-S to NNE-SSW directed stresses, generated within the Indian shield (Khattri et al., 1992; Mukhopadhyay et al., 1993). In the Shillong Plateau, the drainage pattern has been modified by the tectonics and the direction of flow is controlled by the lineaments and faults. The accelerated uplift detected in the middle segment of the Shillong Plateau is also associated with tectonic instability (e.g., Imsong et al., 2016). Further, this study indicates that the detected deformation is caused due to Dauki Fault. The N-S trending Umngot lineament, travels parallel to the Umngot (Dauki) River, as deciphered from the satellite imagery (Srinivasan, 2003; Duarah and Phukan, 2011). However, many questions still remain unanswered regarding the orientation and dynamics of the Dauki Fault.

The 'pop-up' model proposed by Bilham and England, (2001) created controversy in tectonic studies. Recently, Lakshmi and Gawali (2022) investigated earthquake induced deformation features in the Dauki Fault region characterised with micro faults, sand dykes, isolated blocks suspended in sand, structures for water escape, and pinch-swell features. These formations result from the liquefaction of alluvial sediment caused by intense ground shaking. They reported that the earthquake induced deformation features (seismites) in the southern part of Shillong Plateau and the ^{14}C age constraints on seismites, suggested three seismic events. So far, no AMS study in the Shillong Plateau has been yet conducted to infer tectonic regime and to study the deformation.

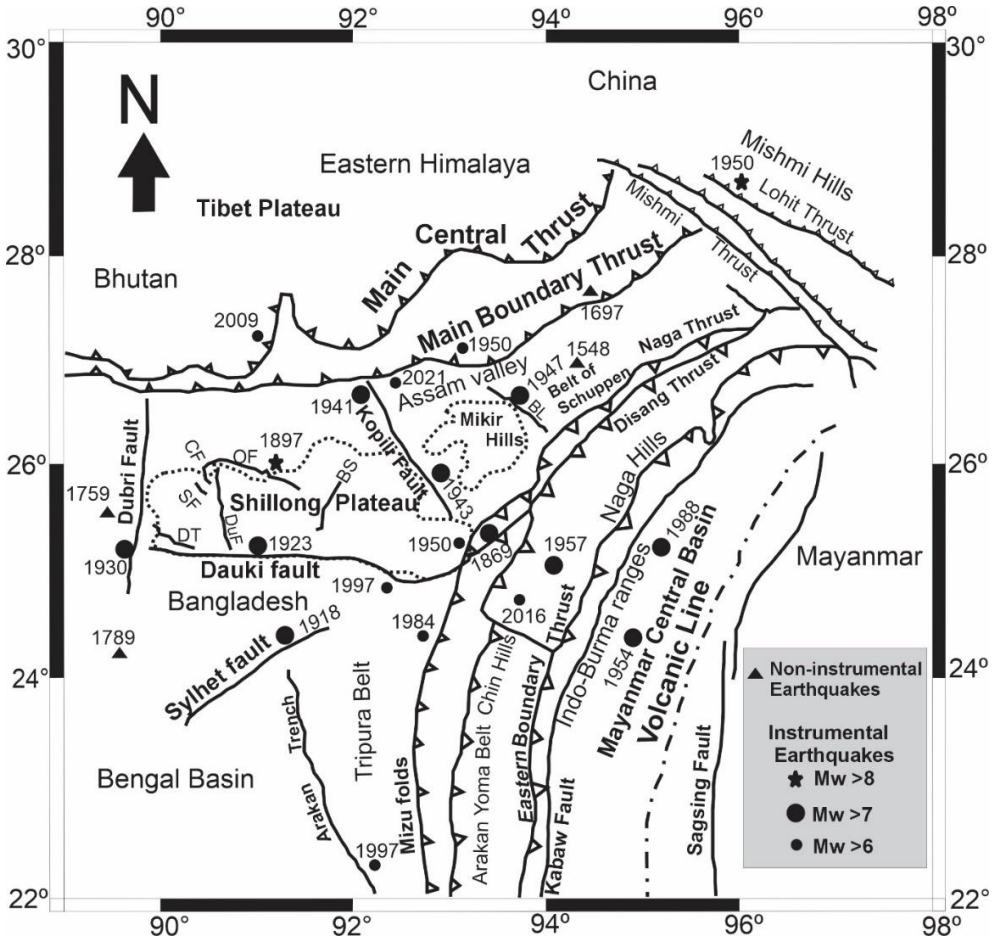

Figure 1. Regional tectonic settings of Northeast India and surrounding regions. CF: Chedrang Fault, OF: Oldham Fault, SF: Samin Fault, DdF: Dhudnoi Fault, DT: Dapsi Thrust, BS: Barapani Shear Zone, BL: Bomdila Lineament (Map sources: Nandy, 2001; Angelier and Baruah, 2009). Black star depicts the two great earthquakes; 1897 Shillong Eq. (Mw-8.1) and 1950 Assam Eq. (Mw-8.3) that occurred in the north east region.

Further, the E-W trending 300 km long Dauki Fault, in Shillong Plateau played an important role as regards to regional deformation in the adjoining regions (Das et al., 1995). There is ongoing discussion regarding issues related to the northern and southern boundary faults. Some authors proposed that Dauki Fault is a normal fault (Hiller and Elahi, 1984; Nandy, 2001) while, some others considered it as a thrust fault (Alam et al., 2003; Srinivasan, 2003; Mitra et al., 2005).

There is no consistent direction of regional NE-SW stress orientation except in the northeastern part of Assam (Rajendran et al., 1992). The focal mechanism solutions suggested N-S, NE-SW and NW-SE compression stresses in the Shillong Plateau (Angelier and Baruah, 2009) and N-S directed compression in the Shillong-Mikir Hills-Assam valley (Chen and Molnar, 1990; Bhattacharya et al., 2008). Gokarn et al. (2008) proposed that the crust in the NE Indian region responds to the compressive forces differently at different depths which is controlled by the rheological considerations. They inferred that at deeper levels, the crustal readjustments take place through the subduction along the Dauki and Brahmaputra thrusts whereas, at the shallow levels the relative deformability of the supracrustal blocks have a strong influence on the tectonics, leading to the strike slip mechanism along the surface expression of the Dauki fault.

In this paper, we report investigations of magnetic analyses performed on fine-grained sediments near the Dauki Fault in the southern sector of the Shillong Plateau, Northeast India (Figures 1 and 2b). Our results permit us to study the magnetic fabric origin in earthquake induced deformed features versus host sedimentary units and to outline the relation between the magnetic lineation and the tectonic structures. In spite of the significance of identifying

seismites, no study has evidently been made to characterise different seismites by magnetic parameters. Except a few, the magnetite fabric in unconsolidated, horizontally stratified clays and other sedimentary deposits, exhibits sensitivity to the minor deformations in tectonic environments (Sagnotti and Speranza, 1993; Sagnotti et al., 1994). AMS investigations have unveiled ~50° successive clockwise rotations in the orientations of compressional strain which occurred in the middle-western Qaidam Basin during the post-mid-Miocene period, shifting from nearly north-south to northeast-southwest (Li et al., 2020).

REGIONAL GEOLOGICAL FRAMEWORK OF SHILLONG PLATEAU

The Dauki River originates from the middle segment of Shillong Plateau and drains into the northern alluvial plains of Bangladesh (Figure 2a, b). The Shillong Plateau contains variety of rock formations. Among them, the Precambrian basement gneissic complex and Proterozoic meta-sedimentary Shillong group constitute the most of it (Figure 2a). In the southern part, Shillong Plateau is surrounded by Tertiary shelf sediments and Cretaceous Sylhet basalt. The mid-Proterozoic Khasi greenstone exposures unconformably overlies the Shillong Group of rocks and granite plutons overlies by Khasi greenstone which is unconformably overlain by Lower Gondwanas. Similarly, Jaintia Group unconformably overlies Khasi Group (Dutta, 1982). Among the five formations of Jaintia Group, Kopili Formation is the youngest formed during Paleocene to Eocene epoch. The Dauki River mainly flow through the Proterozoic granites, Cretaceous-Tertiary sediments, Precambrian banded gneissic complex and Meso-Proterozoic metasediments (GSI, 2009).

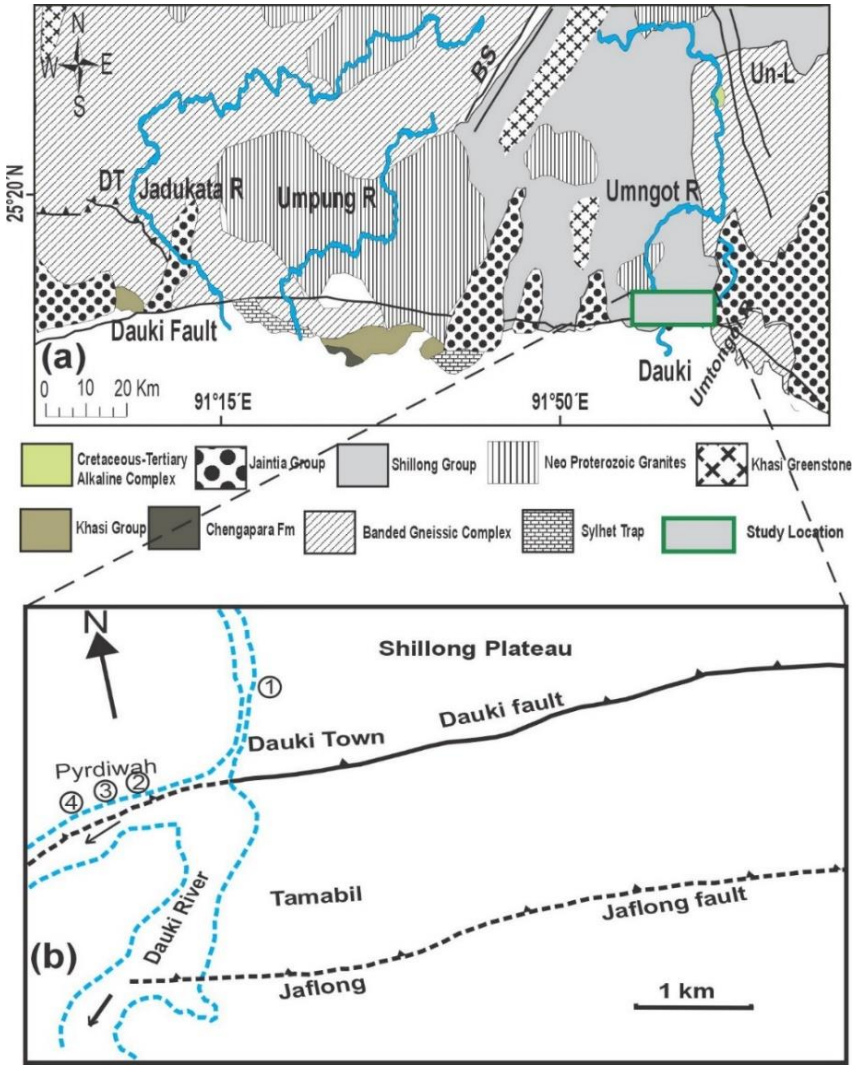

Figure 2. (a) Regional geology map of the study area. (Modified from Imsong et al., 2016 and Lakshmi and Gawali, 2022). DT: Dapsi Thrust, BS: Barapani Shear Zone, Un-L: Umngot Lineament. **(b)** Location map of study area (Lakshmi and Gawali, 2022). Sediment sample collection sites, 1: Dauki, 2, 3 and 4: Pyrdiwah.

SAMPLING AND EXPERIMENTAL METHODS

The area from where the samples have been collected is a watershed area of the Dauki River that has been draining the hinterland and undergoing avulsion from time to time. Sites were selected along the banks of this river such that the sediment section was clearly visible which are away from the anthropogenic influences. For AMS studies, 160 oriented sediment samples from four sites were collected in 8 cm^3 plastic bottles using a portable soft sediment corer and magnetic compass was used for orientation (Figure 2b). The plastic container was sealed tightly so that field in situ arrangement of the sediment particles was not disturbed. All the mineral magnetic measurements were performed at the Indian Institute of Geomagnetism, Navi Mumbai, India. Magnetic mineralogy was deciphered on representative specimens using Isothermal Remanent Magnetization (IRM) acquisition curves, estimation of the remanent coercive force (B_{cr}) and magnetic susceptibility dependence of Temperature curves (χ-T curves). χ-T curves (40°C to 700°C) measured in an argon atmosphere by KLY-4S Kappabridge (AGICO). For IRM measurements, the samples treated to increasing field strengths up to 1 T (SIRM) using a pulse magnetiser (Molspin) and the remanent magnetisation is measured using the spinner magnetometer (Molspin). All the samples were exposed to the back field to estimate B_{cr}. The S ratio was obtained by exposing samples to a back field up to 100 and 300 milli Tesla (mT). S-ratio and Hard isothermal remanent magnetisation (HIRM) were calculated using S-ratio = $IRM_{-300mT}/SIRM_{1T}$ and HIRM = $SIRM_{1T} - IRM_{-300mT}$ (Evans and Heller, 2003). The age of the sediments and the earthquakes affecting them was estimated based on radiocarbon chronology (Lakshmi and Gawali, 2022).

Low-field (300 Am^{-1} at 976 Hz) AMS measured using a multi-function Kappabridge (MFK1-FA-AGICO) for each specimen in 15 directions on three mutually orthogonal planes. The AMS technique represents, second-rank symmetric tensor indicating the principal maximum, intermediate and minimum susceptibility axes $K_{max}>K_{int}>K_{min}$ respectively of the tensor ellipsoid (Hrouda, 1982). SUFAR software supplied by AGICO was used for calculation of different AMS parameters viz. degree of anisotropy (P), magnetic foliation (F), magnetic lineation (L), and shape parameter (T). The T parameter indicates prolate through neutral to oblate when $-1 < T < 0$, $T = 0$ and $0 < T < 1$ conditions respectively (Jelinek, 1981). The mean magnetic susceptibility (K_m) for each specimen is determined from $K_m = (K_{max} + K_{int} + K_{min})/3$.

RESULTS

Magnetic properties

In order to identify magnetic mineralogy, grain size and magnetic concentration, various rock-magnetic experiments were performed. IRM acquisition curves and backfield for representative samples are shown in Figure 3a-b. All samples continue to acquire remanence at greater fields except for sample from site 4 for which the saturation is arrived at < 300 mT, suggesting mostly contribution of magnetite (Figure 3a-b). For samples from sites 1, 2 and 3, saturation is increasing to >300 mT, indicating hard magnetic mineral contribution. The S-ratio and HIRM were used to approximate the relative content of hard magnetic minerals. S-ratio values between 0.80 and 0.99 (mean 0.94) suggested some contribution of hematite in most samples. For most of the samples, the S ratio values ranged from 0.8 to 0.9 for three sites 1, 2 and 3, except site 4 where it is ≥ 0.98 indicating presence of magnetite. However, in site 3, the values from 0.5 to 0.7 suggest contribution from hematite (Robinson, 1986**)**. The HIRM values also support this conclusion. Samples from sites 1, 2, and 3 showing relatively high values of HIRM, coupled with low S-ratio, indicates contribution of hematite. The results of χ–T curves for representative samples are shown in Figure 3c-f. All samples show irreversible thermomagnetic curve due to transformations of magnetic minerals during the laboratory heating processes. During the heating, there is an increase in the magnetic susceptibility up to 300˚C and decrease up to 450˚C. Further it reached minimum value at 580˚C (Figure 3 c-f) suggesting titanomagnetite with a contribution from hematite.

AMS

The K_m values range between 100 and 3610×10^{-6} SI, indicate a prevailing ferromagnetic minerals contribution to the rock matrix (Hrouda and Kahan, 1991; Tarling and Hrouda, 1993). The distribution of K_m values for all the analysed sites are shown in Figure 4. K_m values for sediments from site 1 range between 900 and 3610×10^{-6} SI (Figure 4a) and sediments from site 2 are denoted by K_m values of 100 and 296×10^{-6} SI (Figure 4b).

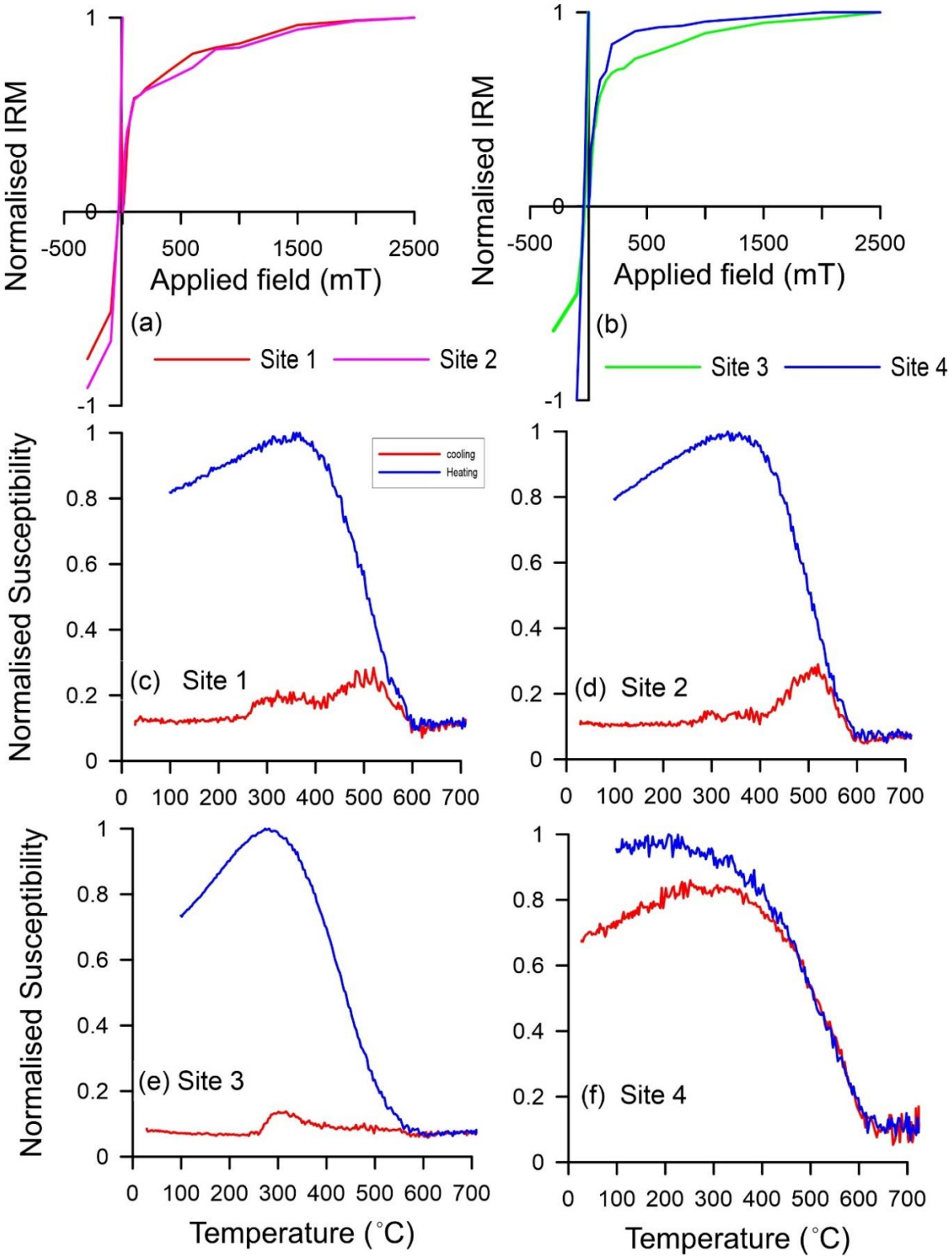

Figure 3. (a-b) Representative Isothermal Remanent Magnetisation (IRM) acquisition curves. **(c-f)** Temperature-dependent magnetic susceptibility curves (χ-T curves) for representative samples. **(c)** Sample DK4 from Site 1, **(d**) Sample BD3 from Site 2, **(e)** Sample MT4 from Site 3 and **(f)** Sample PN3 from Site 4. The red (blue) lines represent heating (cooling) curves.

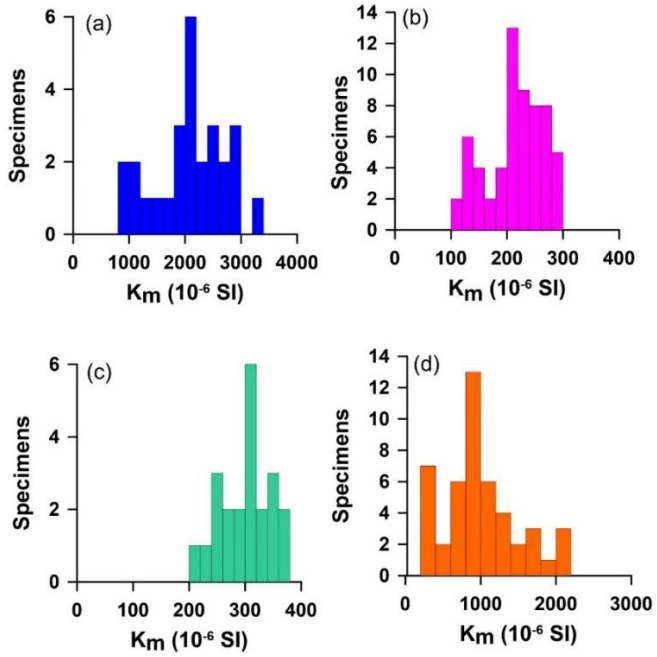

Figure 4. Frequency distribution of mean susceptibility (K_m) values for all the specimens from all the four sites, **(a)** Site 1, **(b)** Site 2, **(c)** Site 3 and **(d)** Site 4.

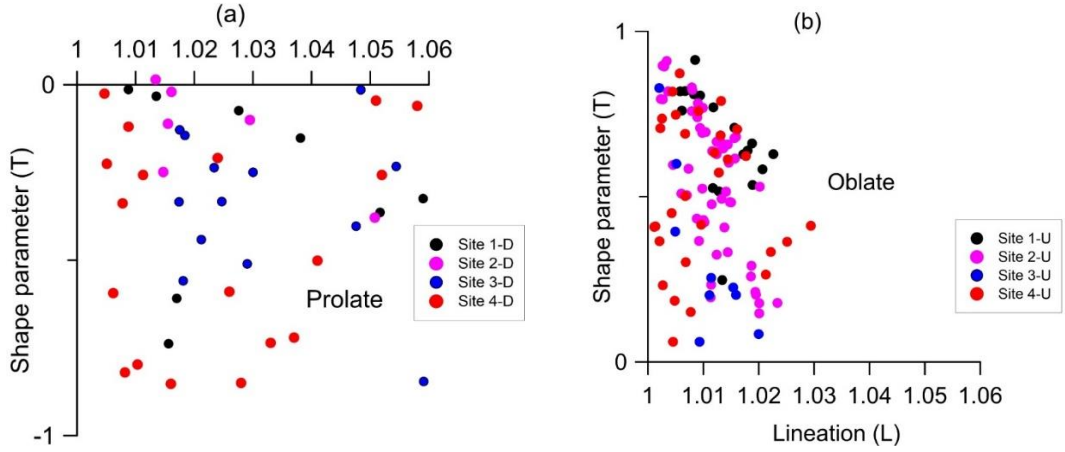

Figure 5. Magnetic lineation (L) vs. shape parameter (T) results of **(a)** deformed (seismites), and **(b)** undeformed, from all the four sites.

The K_m values from site 3 range from 100×10^{-6} to 377×10^{-6} SI (Figure 4c) and Site 4 has a K_m distribution, with a main grouping between 200 and 2110×10^{-6} SI (Figure 4d). Among the all the four sites, sites 2 and 3 are very low as compare to the sites 1 and 4. These low K_m values suggest that the main magnetic carriers of the both rocks are paramagnetic minerals (Rochette et al., 1992) with a little ferromagnetic minerals. The higher K_m values from sites 1 and 4, indicate that the dominant magnetic carriers are paramagnetic mineral but richer in ferromagnetic mineral.

The analysis of T and L are plotted for all four sites with respect to undeformed (depositional) and deformed (earthquake induced) states of the sites (Jelinek, 1981; Hrouda, 1982). At all the sites, the undeformed specimens mostly fall in oblate field and deformed specimens fall under prolate field (Figure 5). The deformed layers show high T and high L values than the depositional sedimentary layers.

Site 1

The site was located on the west bank of the Dauki River near the Dauki town (Figure 2) where the trench was excavated. At site 1, a section of 1.5 m deep and 1 m wide was exposed. In this section, six visually distinguishable fine silt to fine sand beds of varying thickness can be identified and have

been designated as units 1, 2, 3, 4, 5 and 6 from top to bottom (Figure 6). At this site 1, 1.5 m deep sediment section show deformed features covering undeformed layers, interpreted to be caused by earthquake activity (Lakshmi and Gawali, 2022). In this site, the section consists of fine sand and some units are disturbed and displaced with a displacement of 7 cm. The origin of deformation was the large paleoseismic event occurring in modern age. The section was sampled from undeformed covering layer (site1-U) and deformed layers (site1-D) for AMS (Figure 6). At this site, the K_{max} and K_{int} of site1-U specimens form a girdle and K_{min} has formed clustered with vertical to sub-vertical and all the axes of site1-D specimens show triaxial to prolate shape with K_{max} in SE dipping parallel to the strike of the microfault.

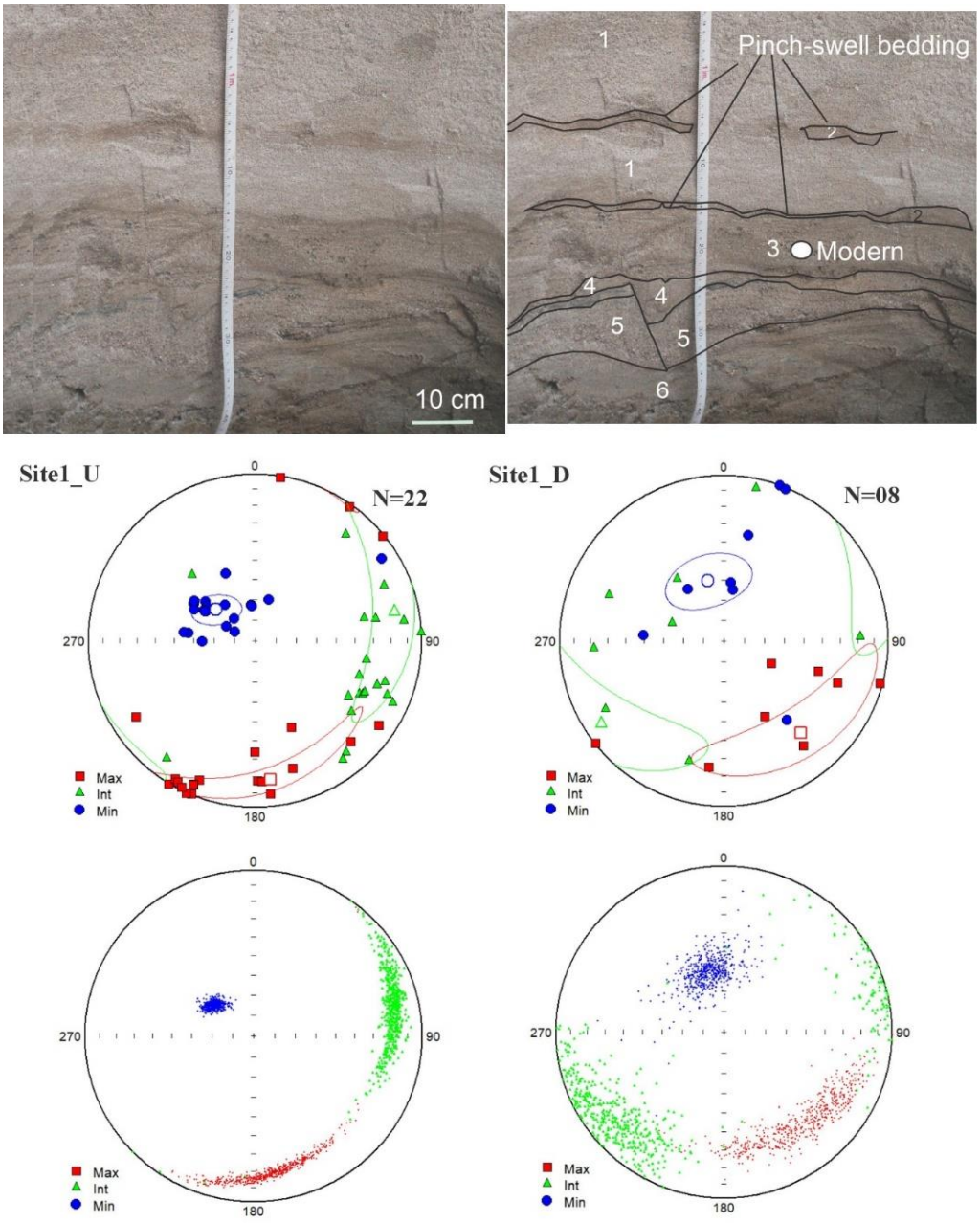

Figure 6. Anisotropy of magnetic susceptibility (AMS) results for undeformed and deformed sediments from Site 1. Top panel: Photograph showing earthquake induced deformation features at Site 1 (Lakshmi and Gawali, 2022). Middle panel: The distribution of the K_{max}, K_{int} and K_{min} parameters plotted on Equal-area lower hemisphere projections and their 95% confidence angles. Bottom panel: Equal-area lower hemisphere projections of bootstrapped AMS principal axes.

Site 2

A 1 m deep and ~1 m wide trench, at site 2 was excavated. The 1 m trench section consists of fine to coarse white and brown sand, with clay overlying it, and clay silt underlying (Figure 7). The top 30 cm consists of clay, underlain by fine sand of 50 cm. The observed deformed feature is fine sand intruded into the host sediment broader towards the top of the section (Figure 7). This site witnessed a liquefaction feature that occurred between 5415±35 BP to 9140±50 BP (Lakshmi and Gawali, 2022). At this site, K_{max} and K_{int} of undeformed layers (site2-U) developed NW-SE girdle in subhorizontal direction and K_{min} is well clustered with SW dipping (Figure 7). The earthquake induced liquefaction feature (site2-D) show clustering however with streaked pattern (Figure 7) and K_{max} is in N-S orientation.

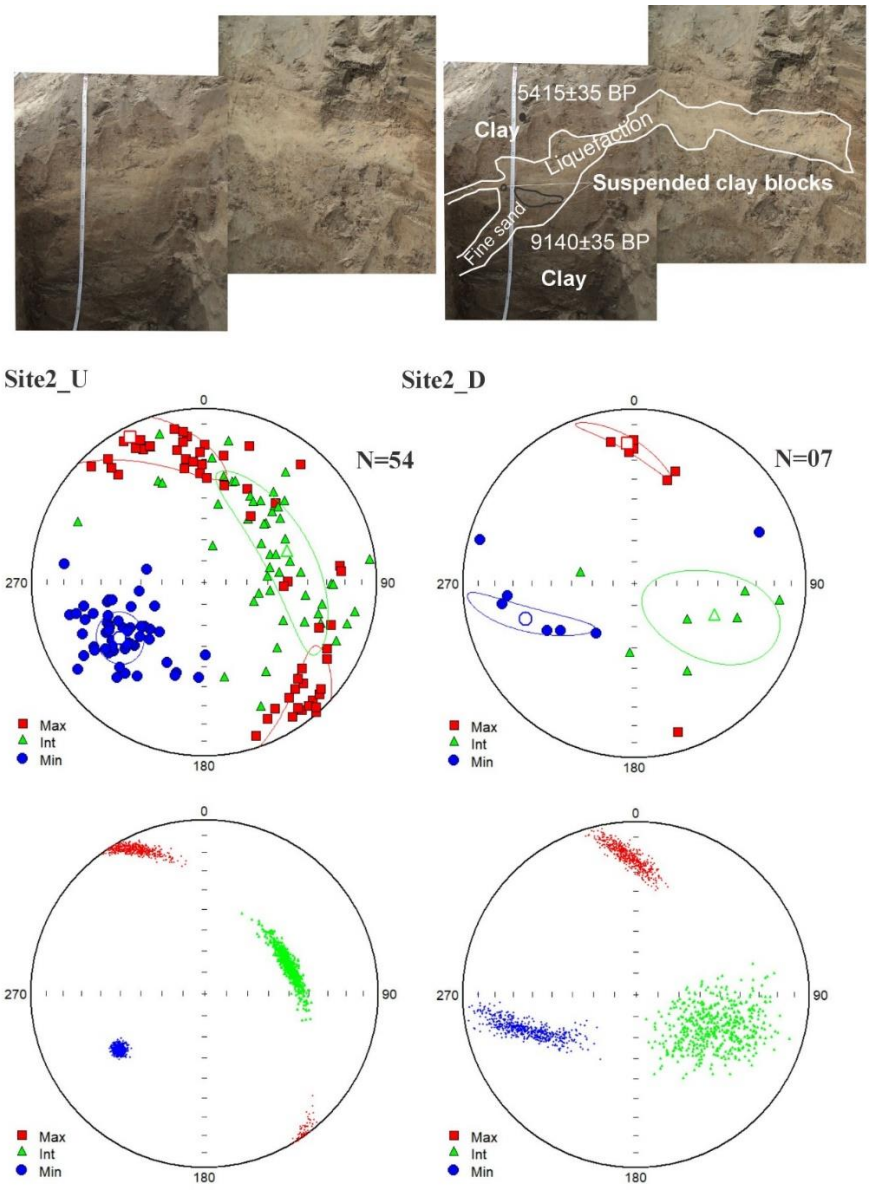

Figure 7. Anisotropy of magnetic susceptibility results for undeformed and deformed sediments from site 2. Top panel: Photograph showing earthquake induced deformation features at site 2 (Lakshmi and Gawali, 2022). Middle panel: The distribution of the K_{max}, K_{int} and K_{min} parameters plotted on equal-area lower hemisphere projections and their 95% confidence angles. Bottom panel: equal-area lower hemisphere projections of bootstrapped AMS principal axes.

Site 3

At this site, a 2.1 m deep and 1 m wide section was exposed consisting of clay and silty sand (Figure 8). Liquefaction dykes have been observed with conical and tubular shape. This area was known to have suffered a major earthquake around 4285±35 BP (Lakshmi and Gawali, 2022). The origin of these liquefaction dykes is assigned to the cause of earthquake induced phenomenon. At this site, undeformed specimens show subvertical K_{min} axes mostly oriented towards NW and horizontal K_{max} axes. In contrast, well clustered all 3 axes with vertical to subvertical K_{min} with westward dipping and K_{int} and K_{max} are well clustered with eastward and southward dipping respectively (Figure 8).

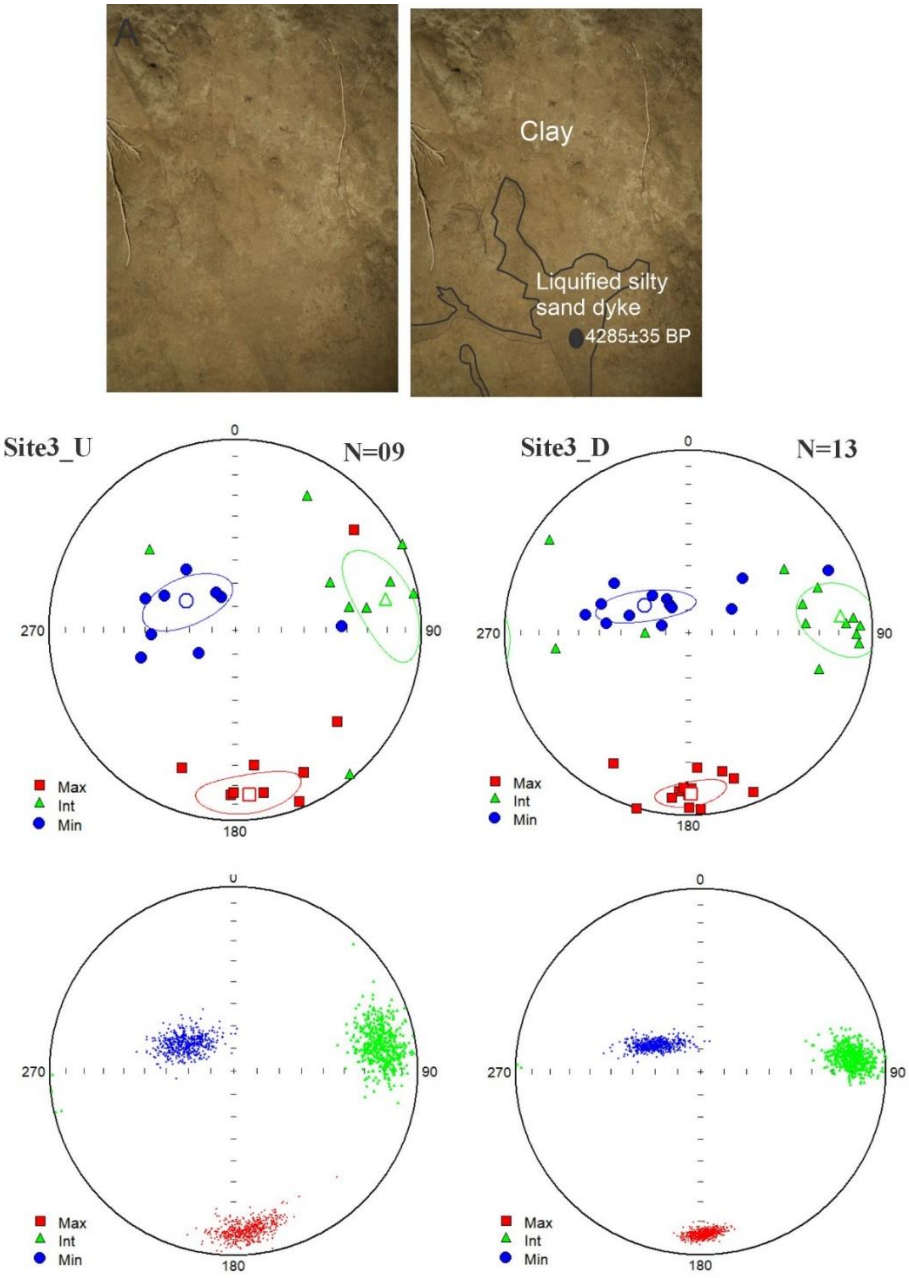

Figure 8. Anisotropy of magnetic susceptibility results for undeformed and deformed sediments from site 3. Top panel: Photograph showing earthquake induced deformation features at site 3 (Lakshmi and Gawali, 2022). Middle panel: The distribution of the K_{max}, K_{int} and K_{min} parameters plotted on equal-area lower hemisphere projections and their 95% confidence angles. Bottom panel: equal-area lower hemisphere projections of bootstrapped AMS principal axes.

Site 4

At this site, the top 1.0 m section of the excavated trench (1.8 m-deep and 1.5m-wide) consists of undisturbed clay and some deformation features present at the bottom 0.7 m (Figure 9). The observed deformation features are displaced silty-clay layer, presence of clasts and fluid escape dish structures. The origin of these deformation features is interpreted to have derived from earthquake induced liquefaction. Age constraints were evolved based on two radiocarbon ages yielding around 130 ± 30 BP and 920 ± 30 BP (Lakshmi and Gawali, 2022). At this site, all the undeformed specimens show well clustered K_{min} axes, horizontal dipping westward and K_{int} and K_{max} formed girdle N-S with sub-horizontal eastward dipping (Figure 9). The three axes of deformed specimens are randomly distributed with K_{max} in N-S orientation.

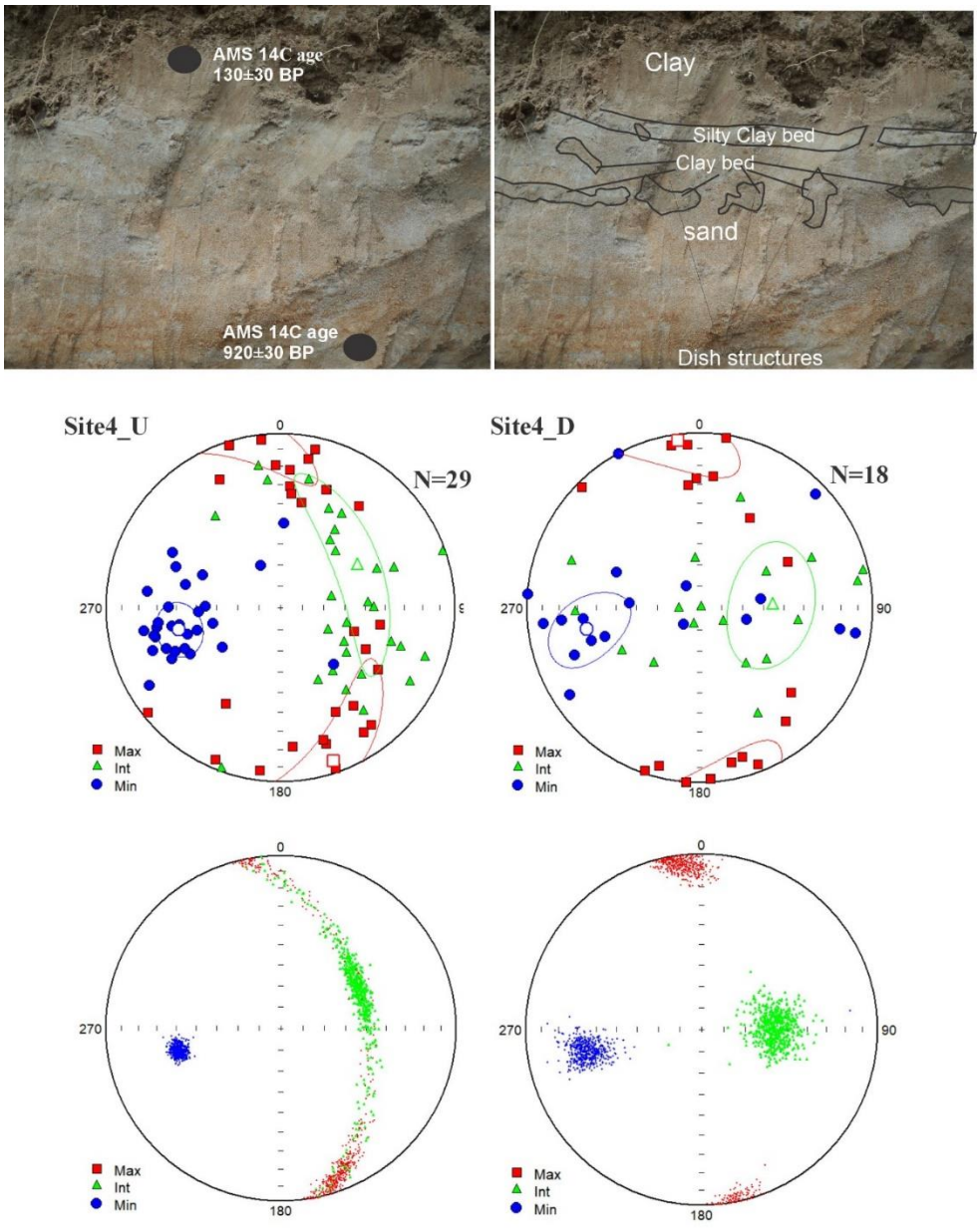

Figure 9. Anisotropy of magnetic susceptibility results for undeformed and deformed sediments from site 4. Top panel: Photograph showing earthquake induced deformation features at site 4 (Lakshmi and Gawali, 2022). Middle panel: The distribution of the K_{max}, K_{int} and K_{min} parameters plotted on equal-area lower hemisphere projections and their 95% confidence angles. Bottom panel: equal-area lower hemisphere projections of bootstrapped AMS principal axes.

DISCUSSION

In sedimentary rocks, the AMS fabric indicated dispersed K_{max} and K_{int} directions within a horizontal plane and well grouped vertical K_{min} with an oblate shape (Tarling and Hrouda, 1993; Liu et al. 2001). The results show that the undeformed layers are characterised by oblate AMS ellipsoids pertinent with the criteria defining sedimentary process and hence depositional fabric, whereas the AMS fabric obtained from seismites are characterised by distinct triaxial to prolate ellipsoids. The clustering of the K_{max} axes, observed at all sites, defines a distinct magnetic lineation that cannot be related to sedimentary processes.

Furthermore, no studies about paleo-current directions were carried out so far from the lithologies of the sampled formations, thus we cannot test the existence of correlation between them and the observed magnetic lineation directions. Conversely, analogously to other weakly deformed sediments in various compressive and extensional settings, the magnetic lineation that we found may rather be interpreted as the first effect of a superimposed stress field. This hypothesis is supported by three lines of evidences: (1) the triaxial to prolate AMS ellipsoid shapes of sites; (2) the correlation between T and L parameters observed at all sites (Figure 5); and (3) the scattering of the K_{int} and K_{min} axes around a plane perpendicular to the cluster of K_{max} axes observed at site 2 (Figure 7). These features are not compatible with an original ‘‘sedimentary’’ fabric and cannot be related to the action of paleo-currents. In particular, the dispersion of the K_{int} and K_{min} axes is a clear tectonic effect that occurs when mineral rotations are developed enough to bring grains to a high angle to the shortening direction and to impart a magnetic fabric (Pares, 2004; Cifelli et al., 2005). On the contrary, the oblate shape of the AMS ellipsoid is strongly indicative of a pure sedimentary fabric, with no effect of water current, as expected for these fine-grained lithologies.

In order to relate sedimentary fabric with earthquake induced deformation we have analysed L versus T plot. The process of deformation of soft sediments can lead to variation of strain ellipsoid associated with formation of a lineation. An increase in the values of L and a change in the value of T can be revealed in this process (Cho et al., 2017). The deformed layers (seismites) show low T values with high K_{max} (Figure 5a) while undeformed layers show high T and low L values. Further, the L-T plot allows seismites of different origins to be correlated with specific types of deformation. Sites 1 and 4 including the faulting, are characterised by a high L (~1.06) and low T (-0.7) values. During the faulting, the damage zones are associated with an inelastic deformation (Levi et al., 2014). This deformation is expressed by the formation of a high magnetic lineation and prolate shape, as identified by the high L (1.06) and low T (-0.7) values. Unlike other seismite types, during the liquefaction process the particles completely lose their cohesion and mobilize away from the source layer, and because the shear rate may change from place to place. Under these conditions, the oblate shape of the magnetic fabric decreases (Levi et al., 2006), and the lineation is relatively low. Figure 5 shows that the range of L (1.03) and T (-0.5) values of the liquefaction features (sites 2 and 3) is almost distinguishable from the range of values of the faulting.

Tectonic implications

The magnetic fabric in deformed sediments, has been established which provide an esteemed strain proxy when visible strain markers are not recognizable in the field and the magnetic lineation will be parallel to the maximum elongation axis of the strain ellipsoid (Hrouda and Kahan, 1991). During the incipient stages of deformation, the magnetic lineation (K_{max}) axes tend to cluster parallel to the direction of the fold axes whereas magnetic foliation maintains parallel to the bedding of the strata in compressive settings, and K_{max} perpendicular to the normal faults in extensional basins (Maffione et al. 2012; Caricchi et al. 2016). Moreover, AMS studies provide pertinent details about the local tectonic regime acting during sedimentation (Mattei et al., 1997; Sagnotti et al., 1994).

The K_{max} generally covers a wider range of azimuths, both within a single layer and throughout a stratigraphic sequence in the current induced magnetic fabrics (Tarling and Hrouda, 1993). Several studies show that, when the K_{max} is controlled by the paleo-flow, K_{max} generally extend over a wide range of azimuths, corresponding to temporal changes of the flow direction within the basin (Hamilton and Rees, 1970; Kissel et al., 1997). On the contrary, in all the deformed sites, the trend of the magnetic lineation is maintained through sequences that differ in sedimentological characters and age. Furthermore, a correlation between the orientation of the tectonic stress and the K_{max} has been noted. These observations support a tectonic origin of the magnetic lineation.

Relying on the correlation between the orientation of the magnetic lineation and regional stress field, the origin of the K_{max} from the four sites, characterized by a well-defined K_{max}, was evaluated. The eastern and western parts of Shillong Plateau is dominated by NNE-SSW and NNW-SSE compressions respectively (Baruah et al., 2016). The uplift of the Shillong Plateau has been attributed by some studies to the India-Eurasia collision, and the resulting N-S to NNE-

SSW directed stresses generated within the Indian shield (Chen and Molnar 1990; Khattri et al. 1992; Mukhopadhyay et al. 1993). Several studies revealed almost NE–SW σH_{max} stress orientation in the Shillong Plateau, the Assam valley, the eastern part of the Bengal basin and the Indo-Burma Ranges (Khan and Chouhan, 1996; Bhattacharya et al., 2008). The observed N–S trending K_{max} in the present study, at all the four sites, is similar to the stretching direction and perpendicular to the E-W trending Dauki Fault as always expected in extensional tectonic settings (Lowrie, 1989). Taking note of that, an extensional magnetic lineation is deduced from the present study sites. This suggests that the present study sites located to the eastern segment of Dauki Fault recorded an N-S extension.

Consequently, this inferred N-S extension by AMS analysis is compatible with the regional stress field controlling fault activity. Lakshmi and Gawali (2022) discussed the occurrence of a seismic event in the form of micro fault at trench site 1. The observed N-S extension in the present study could be thus compatible with the normal fault observed in the trench site 1. Further, the presence of some extensional stresses at shallower depths is envisaged in the Bengal basin, the Shillong plateau, and Assam valley using finite element modelling (Islam and Shinjo, 2012). Furthermore, Islam et al., (2011b) predicted that Dauki as a thrust fault with a few conjugate normal faults at shallower depths <30 km. These results are compatible with extensional magnetic lineation deduced from the present study. The correlation between the orientation of the tectonic stress and the magnetic lineation observed from the four sites along the Dauki Fault, reveals a tectonic origin.

CONCLUSIONS

In the present study, we used AMS data from four sites in the Dauki Fault Zone, Shillong Plateau. The AMS results recorded the existence of different types of magnetic fabrics within the study sites. The undeformed sediment layers are characterized by subvertically clustered K_{min} and streaked K_{max} - K_{int} axes on a nearly horizontal plane with oblate shape, whereas the seismites are characterised by triaxial to prolate shape. The L-T plot shows that the seismites are organised by low T and high L values. The N-S magnetic lineation deduced from the present study is oriented perpendicular to the E-W trend of the Dauki Fault, recommending that it has a tectonic origin. The existence of extensional AMS features near Dauki Fault from the present study is compatible with the normal faults under extensional stress conditions predicted by earlier studies in Shillong Plateau using finite element modelling. The results of the present study substantiate the typical relation between the orientation of magnetic lineation and the main tectonic features and also accentuates the great prospects for inspecting tectonic deformation. The novelty of this AMS approach aids in characterising seismites and thus may provide crucial insights into paleoseismic records.

Acknowledgements

We acknowledge financial support from CLAIMs programme of DST-IIG. We are grateful to the Chief Editor, and two anonymous reviewers for their insightful comments and suggestions that improved this paper.

Author Credit Statement

Md. Mujahed Baba, B.V. Lakshmi and K. Deenadayalan organized field work, sampling, measurement, data analysis and wrote manuscript. Pradnya Mohite did measurements and analysed the data. V.M. Rokade and S.N. Patil took part in geological discussions. A.P. Dimri, Final review and discussion.

Data Availability

The data underlying this article will be shared on reasonable request to the corresponding author.

Compliance with Ethical Standards

The authors declare no conflict of interest and adhere to copy right norms.

References

Alam, M., Alam, M.M., Curray, J.R., Chowdhury, M.L.R. and Gani, M.R., 2003. An overview of the sedimentary geology of the Bengal Basin in relation to the regional tectonic framework and basin-fill history. Sedimentary Geol., 155(3–4), 179–208.

Angelier, J. and Baruah, S., 2009. Seismotectonics in Northeast India: a stress analysis of focal mechanism solutions of earthquakes and its kinematic implications. Geophys. J. Int., 178(1), 303–326.

Baruah, S., Baruah, S., Saikia, S., Mahesh, N.S., Sharma, A., Reddy, C.D. and Kayal, J.R., 2016. State of tectonic stress in Shillong Plateau of northeast India. Phys. Chem. Earth, Parts A/B/C, 95, 36–49.

Basavaiah, N., Appel, E., Lakshmi, B.V., Deenadayalan, K., Satyanarayana, K.V.V., Misra, S., Juyal, N. and Malik, M.A., 2010. Revised magnetostratigraphy and characteristics of the fluviolacustrine sedimentation of the Kashmir basin, India, during Pliocene- Pleistocene. J. Geophys. Res. Solid Earth, 115(B8).

Bhattacharya, P.M., Mukhopadhyay, S., Mazumdar, R. K. and Kayal, J.R., 2008. 3-D seismic structure of the northeast India region and its implications for local and regional tectonics. J. Asian Earth Sci., 33, 25–41.

Bilham, R. and England, P., 2001. Plateau 'pop-up' in the great 1897 Assam earthquake. Nature, 410(6830), 806–809.

Borradaile, G.J. and Tarling, D.H., 1981. The influence of deformation mechanisms on magnetic fabrics in weakly deformed rocks. Tectonophysics, 77, 151–168.

Caricchi, C., Cifelli, F., Kissel, C., Sagnotti, L. and Mattei, M., 2016. Distinct magnetic fabric in weakly deformed sediments from extensional basins and fold-and-thrust structures in the Northern Apennine orogenic belt (Italy). Tectonics, 35(2), 238–256.

Chen, W.P. and Molnar, P., 1990. Source parameters of earthquakes and intraplate deformation beneath the Shillong Plateau and the northern Indoburman ranges. J. Geophys. Res., Solid Earth, 95(B8), 12527–12552.

Cho, H., Son, M., Sohn, Y.K. and Park, M.E., 2017. Magnetic fabric (anisotropy of magnetic susceptibility) constraints on emplacement mechanism of clastic dikes. J. Geophys. Res., Solid Earth, 122, 3306–3333.

Cifelli, F., Mattei, M., Hirt, A.M. and Günther, A., 2004. The origin of tectonic fabrics in "undeformed" clays: the early stages of deformation in extensional sedimentary basins. Geophys. Res. Lett., 31(9). L09604, doi:10.1029/2004GL019609

Cifelli, F., Mattei, M., Chadima, M., Hirt, A.M. and Hansen, A., 2005. The origin of tectonic lineation in extensional basins: combined neutron texture and magnetic analyses on ''undeformed'' clays. Earth Planet Sci Lett., 235, 62–78.

Das, J.D., Saraf, A.K. and Jain, A.K., 1995. Fault tectonics of the Shillong plateau and adjoining regions, north-east India using remote sensing data. Int. J. Remote Sens., 16(9), 1633–1646.

Duarah, B.P. and Phukan, S., 2011. Understanding the tectonic behaviour of the Shillong plateau, India using remote sensing data. J. Geol. Soc. India, 77, 105–112.

Dutta, S.K., 1982. Tertiary stratigraphy of upper Assam. J. Palaeont. Soc. Ind. Spec. Publ, (1), 65–83.

Evans, M.E. and Heller, F., 2003. Environmental Magnetism: Principles and Applications of Enviromagnetics, Academic Press, New York, 1–322.

Gokarn, S. G., Gupta, G., Walia, D., Sanabam, S. S. and Nitu Hazarika., 2008. Deep geoelectric structure over the Lower Brahmaputra valley and Shillong Plateau, NE India using magnetotellurics. Geophys. J. Int., 173, 1, 92-104.

GSI, 2009 Geology and mineral resource of Meghalaya. Geol. Survey India Miscellaneous Publ. no. 30 Part IV v. 2(1).

Hamilton, N. and Rees, A.I., 1970. The use of magnetic fabric in palaeocurrent estimation (445–464). Paleogeophysics, Academic press.

Hiller, K. and Elahi, M., 1984, February. Structural development and hydrocarbon entrapment in the Surma basin/Bangladesh (northwest Indo Burman fold belt). In SPE Offshore South East Asia Show, SPE-12398-MS. SPE. https://doi.org/10.2118/12398-MS

Hirt, A.M., Evans, K.F. and Engelder, T., 1995. Correlation between magnetic anisotropy and fabric for Devonian shales on the Appalachian Plateau. Tectonophysics, 247(1–4), 121–132.

Hrouda, F., 1982. Magnetic anisotropy of rocks and its application in geology and geophysics. Geophys. Surv., 5(1), 37–82.

Hrouda, F. and Kahan, S., 1991. The magnetic fabric relationship between sedimentary and basement nappes in the High Tatra Mts. (N Slovakia). J. Structural Geol., 13, 431–442.

Imsong, W., Choudhury, S. and Phukan, S., 2016. Ascertaining the neotectonic activities in the southern part of Shillong Plateau through geomorphic parameters and remote sensing data. Curr. Sci., 91–98.

Islam, M.S., Shinjo, R. and Kayal, J.R., 2011a. Pop-up tectonics of the Shillong Plateau in northeastern India: Insight from numerical simulations. Gondwana Res., 20(2–3), 395–404.

Islam, M.S., Shinjo, R. and Kayal, J.R., 2011b. The tectonic stress field and deformation pattern of northeast India, the Bengal basin and the Indo-Burma Ranges: A numerical approach. J. Asian Earth Sci., 40(1), 121–131.

Islam, M.S. and Shinjo, R., 2012. The Dauki fault at the Shillong plateau-bengal basin boundary in northeastern India: 2D finite element modeling. J. Earth Sci., 23, 854–863.

Jelinek, V., 1981. Characterization of the magnetic fabric of rocks. Tectonophysics, 79(3–4), T63–T67.

Kayal, J.R., Arefiev, S.S., Barua, S., Hazarika, D., Gogoi, N., Kumar, A., Chowdhury, S.N. and Kalita, S., 2006. Shillong plateau earthquakes in northeast India region: complex tectonic model. Curr. Sci., 109–114.

Khan, A.A. and Chouhan, R.K.S., 1996. The crustal dynamics and the tectonic trends in the Bengal Basin. J. Geodyn., 22(3–4), 267–286.

Khattri, K. N., Chander. R., Mukhopadhyay, S., Sriram, V. and Khanal, K. N., 1992. A model of active tectonics in the Shillong massif region; In: Sinha, A.K. (Ed.). The Himalayan Orogen and Global Tectonics; Oxford and IBH Publ. Co., 205–222.

Kissel, C., Laj, C., Lehman, B., Labyrie, L. and Bout-Roumazeilles, V., 1997. Changes in the strength of the Iceland–Scotland overflow water in the last 200,000 years: evidence from magnetic anisotropy analysis of core SU90–33. Earth Planet. Sci. Lett., 152(1–4), 25–36.

Lakshmi, B.V. and Gawali, P.B., 2022. Soft sediment deformation features in Dauki Fault region: evidence of paleoearthquakes, Shillong Plateau, NE India. Environ. Earth Sci., 81(3), p.58.

Lakshmi, B.V., Deenadayalan, K., Gawali, P.B. and Misra, S. 2020. Effects of Killari earthquake on the paleo-channel of Tirna River Basin from Central India using anisotropy of magnetic susceptibility. Scientific Reports, 10, 20587. https://doi.org/10.1038/s41598-020-77542-9

Levi, T., Weinberger, R., Aïfa, T., Eyal, Y. and Marco, S., 2006. Earthquake-induced clastic dikes detected by anisotropy of magnetic susceptibility. Geology, 34(2), 69–72,

Levi, T., Weinberger, R. and Marco, S., 2014. Magnetic fabrics induced by dynamic faulting reveal damage zone sizes in soft rocks, Dead Sea basin. Geophys. J. Int., 199, 1214–1229.

Li, B., Yan, M., Zhang, W., Parés, J.M., Fang, X., Yang, Y., Zhang, D., Guan, C. and Bao, J., 2020. Magnetic fabric constraints on the Cenozoic compressional strain changes in the Northern Qaidam marginal thrust belt and their tectonic implications. Tectonics, 39(6), e2019TC005989.

Liu, B., Saito, Y., Yamazaki, T., Abdeldayem, A., Oda, H., Hori, K. and Zhao, Q., 2001. Paleocurrent analysis for the Late Pleistocene–Holocene incised-valley fill of the Yangtze delta, China by using anisotropy of magnetic susceptibility data. Marine Geol., 176(1–4), 175–189.

Lowrie, W., 1989. Magnetic analysis of rock fabric, In: Geophysics. Encyclopedia of Earth Science. Springer, Boston, MA. https://doi.org/10.1007/0-387-30752-4_87.

MacDonald, W.D. and Palmer, H.C., 1990. Flow directions in ash-flow tuffs: a comparison of geological and magnetic susceptibility measurements, Tshirege member (upper

Bandelier Tuff), Valles caldera, New Mexico, USA. Bulletin volcanology, 53, 45–59.

Maffione, M.S., Pucci. L., Sagnotti. and Speranza.F., 2012. Magnetic fabric of Pleistocene continental clays from the hanging-wall of an active low-angle normal fault (Altotiberina Fault, Italy); Int. J. Earth Sci., 101, 849–861, doi:10.1007/s00531-011-0704-9.

Mattei, M., Sagnotti, L., Faccenna, C., Funiciello, R., 1997. Magnetic fabric of weakly deformed clay-rich sediments in the Italian peninsula: relationship with compressional and extensional tectonics. Tectonophysics, 172, 107122.

Mitra, S., Pristley, K., Bhattacharya, A. and Gaur, V. K., 2005. Crustal structure and earthquake focal depths beneath northeastern India and southern Tibet. Geophys. J. Int., 160 227–248.

Mukhopadhyay, S., Chander, R. and Khattri, K.N., 1993. Fine structure of seismotectonics in western Shillong massif, north east India. Proc. Indian Acad. Sci., Earth and Planetary Sciences, 102, 383–398.

Nandy, D.R., 2001 Geodynamics of Northeastern India and the adjoining region. Scientific Book Centre.

Pares, J.M., 2004. How deformed are weakly deformed mudrocks? Insights from magnetic anisotropy. Geol. Soc. Lond. Spec Publ, 238, 191–203.

Pares, J.M., Hassold, N.J.C., Rea, D.K. and Van der Pluijm, B.A., 2007. Paleocurrent directions from paleomagnetic reorientation of magnetic fabrics in deep-sea sediments at the Antarctic Peninsula Pacific margin (ODP Sites 1095, 1101). Marine Geol., 242(4), 261–269.

Porreca, M. and Mattei, M., 2012. AMS fabric and tectonic evolution of Quaternary intramontane extensional basins in the Picentini Mountains (southern Apennines, Italy). Int. J. Earth Sci., 101, 863–877.

Robinson, S.G., 1986. The late Pleistocene palaeoclimatic record of North Atlantic deep-sea sediments revealed by mineral-magnetic measurements. Phys. Earth Planet. Int., 42(1–2), 22–47.

Rajendran, C.P., Rajendran, K., Duarah, B.P., Baruah, S. and Earnest, A., 2004. Interpreting the style of faulting and paleoseismicity associated with the 1897 Shillong, northeast India, earthquake: Implications for regional tectonism. Tectonics, 23(4).
https://doi.org/10.1029/2003TC001605

Rajendran, K., Talwani, P. and Gupta, H.K., 1992. State of stress in the Indian subcontinent: a review. Curr. Sci., 62(1–2), 86–93.

Rochette, P., Jackson, M. and Aubourg, C., 1992. Rock magnetism and the interpretation of anisotropy of magnetic susceptibility. Rev. Geophys., 30(3), 209–226.

Sagnotti, L. and Speranza, F., 1993. Magnetic fabric analysis of the Plio-Pleistocene clayey units of the Sant'Arcangelo basin, southern Italy. Phys. Earth Planet. Int., 77(3–4), 165–176.

Sagnotti, L., Faccenna, C., Funiciello, R. and Mattei, M., 1994. Magnetic fabric and structural setting of Plio-Pleistocene clayey units in an extensional regime: the Tyrrhenian margin of central Italy. J. Structural Geol., 16(9), 1243–1257.

Srinivasan, V., 2003. Deciphering differential uplift in Shillong Plateau using remote sensing. J. Geol. Soc. India, 62(6), 773–777.

Tarling, D. H. and Hrouda, F., 1993. The Magnetic Anisotropy of Rocks; Chapman and Hall London, 217 p.

Received on: 29-04-2024 ; Revised on: 26-07-2024; Accepted on: 29-07-2024

J. Ind. Geophys. Union, 28(5) (2024), 314-328

Identification of airborne magnetic and radiometric anomalies to locate probable kimberlite zones associated with other intrusive rocks in Panna Diamond Belt, Madhya Pradesh, India

Jale Lingaswamy[1] and Ram Raj Mathur[2]
[1]Central Soil and Materials Research Station, New Delhi- 110016, India
[2]Centre of Exploration Geophysics, Osmania University, Hyderabad- 500007, India
Corresponding Author: ramrajmathur@gmail.com

ABSTRACT

The Panna Diamond Belt of Madhya Pradesh, India, lies in the Baghain formations of Kaimur and Rewa group of rocks. To delineate the kimberlite zones, airborne magnetic and radiometric surveys were carried out by the Geological Survey of India (GSI) in this belt that cover an area of about 378 km². From the total magnetic anomaly map of the processed aeromagnetic data, as obtained from Geological Survey of India, maps related to reduce-to-pole (RTP), upward continuation, first vertical derivative and analytical signal were generated and subjected to a detailed study in a reduced scale to understand the anomalies. The near circular anomalies and the Euler solutions in the aeromagnetic maps at Hatinitor Pahar, Kadwara and Kishangar areas, showed a probable indication of the occurrence of kimberlites. Modeling of the aeromagnetic anomalies along selected lines was carried out to infer the depth of the kimberlite pipes. At Hantinitor Pahar, a high magnetic intrusive in the central part of the study area was deciphered with a probable magnetic reversal from 2-D modelling of aeromagnetic data. The airborne radiometric surveys showed high thorium anomaly at Kishangar, Kadwara and Moharkuwa in the ternary plot for potassium, uranium and thorium elements, which is thought to be deposited in the fractures associated with kimberlite pipes. The present paper has attempted to study and correlate the airborne magnetic and radiometric data to identify newly discovered kimberlite pipes in Kadwara, Hatinitor Pahar and Kishagar areas of the Panna Diamond Belt. Also, a magnetic intrusive body with a polarity reversal is suggested by 2-D modelling of magnetic data.

Key words: Kimberlite, Aeromagnetic, Airborne radiometric, 2-D modelling, Panna Diamond Belt, Baghain formations,

INTRODUCTION

Kimberlites are ultramafic intrusive rocks that host precious diamonds, which are normally present as xenoliths. Among the cratons of Indian subcontinent, Bundelkhand craton is overlined by Vidhyan group of rocks in Panna Diamond Belt region which is one of the major sources of diamonds in Madhya Pradesh, India. The identification of kimberlite in this Belt is a challenging effort due to their nature and the presence of other intrusive structures, massive heterogeneous crystalline basements and recent alluvium formations in the Vindhyan group of rocks. The kimberlite system shows crater, diatreme and hypabyssal geometries with respect to depth. A possibility exists for identifying kimberlite/ lamproite by their geometry and structural features associated with the formations.

The well-known Majhgawan kimberlite pipes are located in Panna district of Madhya Pradesh at latitude of 24°38'30" N and longitude of 80°02' E as reported in 1827 by Captain J Franklin (Halder and Ghosh, 1978; Sarma, et al., 1999). Earlier, kimberlites were recognized as a separate rock in peridotite (Lewis, 1887). These kimberlites are intruded into Kaimur sandstone. The Hinota pipe was identified 3 km away from the Majhgawan by Geological Survey of India during 1956-1959 with the help of magnetic and electrical surveys (Kailasam, 1971). Several such pipes were identified lying under the younger rocks and the alluvium in the Panna Diamond Belt (Mathur, 1962). Similarly, Rio Tinto identified the exposed Saptarshi field of kimberlite pipes lying approximately 80 km WSW of Majhgawan with the help of ground geophysical, geological and geochemical surveys (Masun et al., 2009).

Aeromagnetic studies have been utilized to understand the nature of the basement structure and estimate the sedimentary thickness and to study the structural features of the intrusive bodies associated with kimberlite/lamproite (Keating, 1995; Sharma et al., 2007). The Madhya Pradesh State Department of Geology and Mining proposed a systematic exploration programme for locating the mineralized zones. Airborne magnetic and radiometric surveys in parts of Tikkamgarh, Panna and Chhatarpur districts in 1968 were initiated under this programme. The survey was carried out by National Geophysical Research Institute (NGRI), Hyderabad along an east-west profile with an interval of 1 km and flying height 150 m. Rao and Narayan (1981) utilized the aeromagnetic data to understand the anomalies associated with the Majhgawan kimberlite.

Geological Survey of India (GSI) conducted aerial surveys with a profile interval of 300 m and flying height 80 m over the Panna Diamond Belt under National Aero Geophysical Mapping Program (NAGMP) over the Obvious Geological Potential (OGP) areas in India in 2018. On a regional scale, GSI located probable kimberlite from aeromagnetic data in

this belt under the National Aero Geophysical Mapping Program programme (Raynes et al., 2018). These kimberlites were reported as B108 and B125 in this Diamond Belt (Kumar et. al., 2020). Apart from these, a few probable kimberlite pipes were also identified by ground gravity and magnetic surveys in Baghain and Rampura-Motwa areas of the belt (Mukherjee et al., 2021).

Earlier, remote sensing and geochemical studies have also been used for the identification of kimberlite /lamproite over this region (Tessema et al., 2012; Mukherjee et al., 2014; Guha et al., 2018; Kusuma and Ram Prasath, 2021). Besides, the aeromagnetic data in the Dharwar craton was analyzed over the known Wajrakarur Kimberlite Field (Rao and Srinivasulu, 1999; Sarma, and Verma, 2001; Rao et al., 2011) on a regional scale to delineate the sub-surface geology with associated intrusive bodies. Airborne radiometric surveys were carried out over lamproite bodies to ascertain the structural trends in parts of eastern Dharwar craton (Ramadass et al., 2015).

An attempt has been made in the present study to delineate kimberlite / lamproite pipes in the Panna Diamond Belt from the airborne magnetic and radiometric surveys carried out by GSI as they reported locations for their probable occurrence. GSI reported anomalies (marked with an arrow) with a diameter of more than 500 m in the present study area (Raynes et al., 2018). From the total magnetic field map and the radiometric data of GSI, reduced-to-pole (RTP) and derivate maps were prepared on a reduced scale to enhance the low amplitude and short wavelength anomalies and understand their nature for identification of kimberlite probable zones. In the present paper, unreported anomalies associated kimberlite pipes have been marked and modelled in the Kadwara, Hatinitor Pahar and Kishangar areas. Modelling carried out across these areas have revealed magnetic intrusive with a reversal of polarity.

GEOLOGY OF THE STUDY AREA

The Vindhyan basin comprises Mesoproterozoic (Ray et al., 2003) to mid NeoProterozoic (Crawford and Compston, 1970) age rocks of Semri, Kaimur, Rewa, and Bhander group that overlies the Bundelkhand basement gneissic complex dated about 3.5 Ga (Sarkar et al., 1984) and the Bundelkhand granite dated 2.4–2.5 Ga (Singh and Slabunov, 2016) which are the oldest geological formations in the area of study. Bundelkhand coarse grained, porphyritic granites are exposed in northern part of the study area. The granitic composition changes from plagioclase to orthoclase feldspar with or without ferro-magnesian minerals. Ultramafic volcanic pipes (kimberlites) and diamond bearing conglomerates beds (Krishnan and Swaminath, 1959) occur in these formations. In the presently studied area, the reported age of the Majhgawan pipe is 974–1170 Ma (Paul et al., 1975) based on K-Ar method. Similarly, Hinota pipe is dated at 1170 ± 46 Ma (Paul et al, 1975). Kimberlites have intruded through Semri and Kaimur group of rocks belonging to Vindhyan supergroup (1599±8 Ma; Rasmussen et al., 2002). The Kaimur group of rocks is mainly comprised of sandstones dated around 910 ±39Ma (Vinogradav et al, 1964). The Rewa group of rocks (710 Ma±120Ma; Srivatava and Rajgopalan, 1988) overlie the kimberlites. Rao (2006) explained that the Majhgawan and Hinota pipes belong to a ‘transitional kimberlite–orangeite–lamproite’ rock type since these pipes have the petrological, geochemical and isotope characteristics of kimberlite, orangeite (Group II kimberlite) and lamproite. Table 1 shows the stratigraphic succession of the Vindhyan super group in the study area.

The study area lies between 24º 27' 24.04" to 24º 37' 49.64" N 79º 40' 14.59" to 79º 51' 43.78" E, which is in SW direction to the Majhgawan pipe. Shales, limestone, sandstone and orthoquartzites are spatially distributed across the study area. The trend of exposed sedimentary rock formations is in NE-SW direction (Figure 1) and they dip towards the SE direction. The thickness of the sediments increases from north to south. The thickness of the Vindhyan group of rocks in Panna Diamond Belt is about 600 m (Bhattacharya et al., 1995). An inferred fault is located by GSI having NW-SE trend (Figure 1). Elevation in the study area varies between 495 to 158 m from mean sea level (Figure 2). The steep sloping area with low elevation is covered by shale rock formation.

Table 1. Stratigraphic succession of the Vindhyan Super Group in the study area (Bhattacharya et al., 1995)

S.No.	Group	Formation	Rock unit
1	Vindhyan Super Group	Rewa	Gahadara sandstone Jihri shale Itwa sandstone Panna shale
2		Kaimur	Baghain sandstone Pipertola conglomerate
3		Semri	Palkawan shale Pandav Fall sandstone

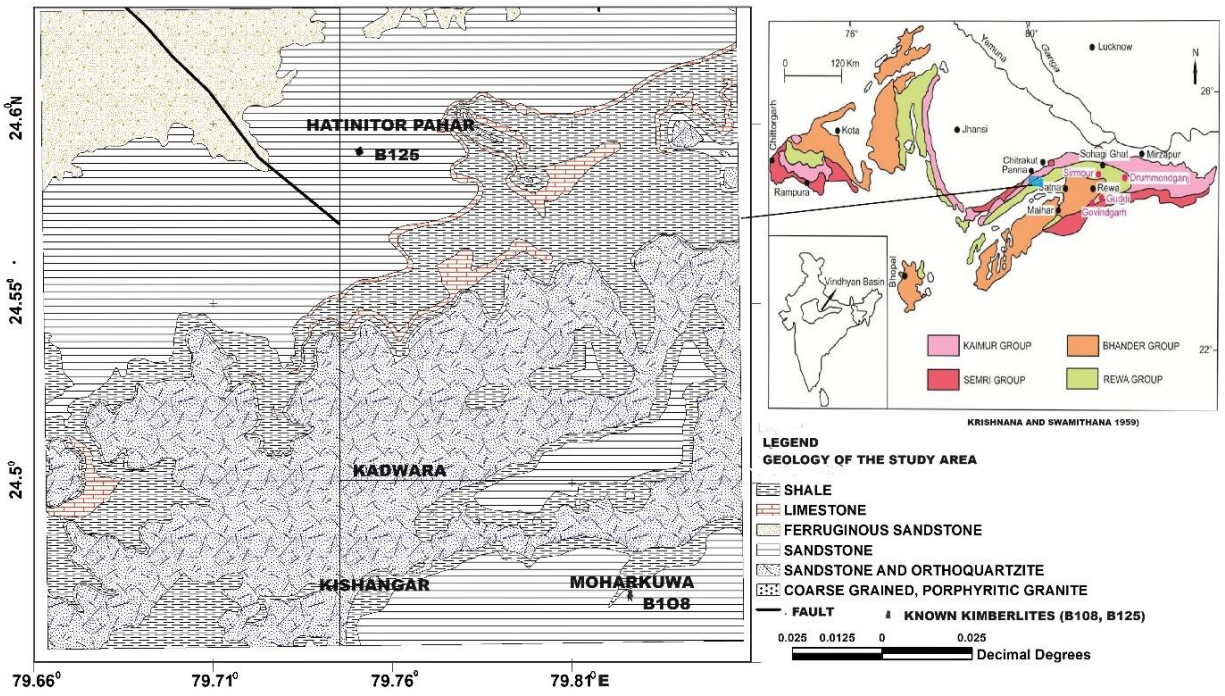

Figure 1. Geological map of the study area (https://bhukosh.gsi.gov.in)

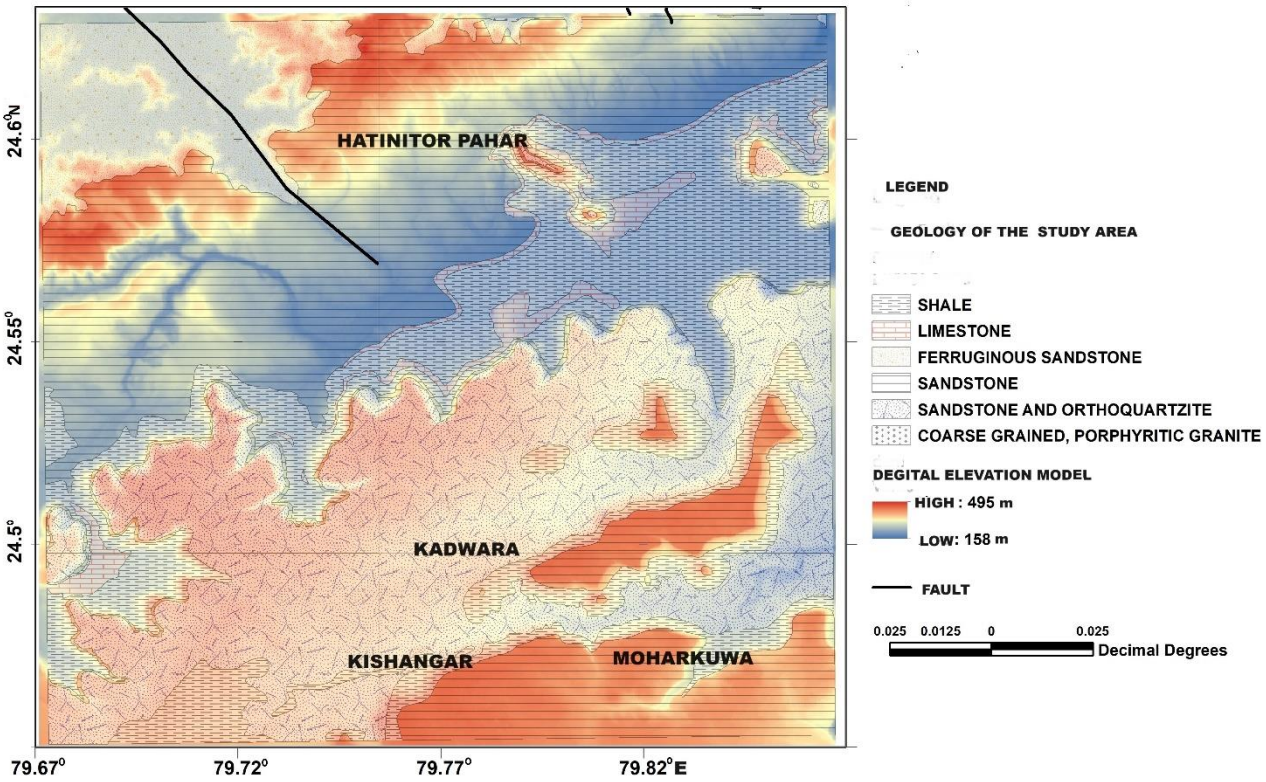

Figure 2. Geological map combined with Digital Elevation Model (DEM) (https://bhuvan-app3.nrsc.gov.in)

AEROMAGNETIC AND RADIOMETRIC SURVEYS

The aeromagnetic and radiometric data was acquired using multi-sensor airborne identification system by GSI under the Obvious Geological Potential (OGP) programme and the authors were given access to the processed data by the Remote Sensing and Aerial Surveys (RSAS), GSI, Bangalore. The study area is a part of the Block-2 of GSI, falling in the Chhatarpur and Sagar regions of Madhya Pradesh and Uttar Pradesh states. The total area of the survey block is 43,814km^2 and total line km is 160,680 km and 3,000 m for the tie-lines. Direction of the survey lines was 135°/315° for the traverse lines and 45°/225° for the tie lines. The aircraft was flown with a speed of 65-85 m/s. The survey was conducted with fixed-wing airborne combined gamma-ray spectrometric and magnetic survey. The aeromagnetic data were sampled with frequency of 10 Hz and radiometric data with a frequency of 1Hz.

A 3X Scintrex make Cs-3 / 4 X GEM System cesium vapor magnetometers (gradient method) were used for the aeromagnetic surveys. A digital 1024-channel spectrometer RSX-500 (Radiation Solution Inc., Canada) including three blocks of polyscine detectors NaI (Tl) for radiometry surveys. I-NEWT mounted 2 RSX-5 and 1 RSX-4 of 50.4 litres total capacity for the downward looking detectors and upward looking detectors of 8.4 litres capacity were used for the airborne radiometric surveys.

The authors re-analyzed the aeromagnetic data of GSI (Raynes et al., 2018). The International Geomagnetic Reference Field (IGRF) flight heading, elevation, and lag corrected airborne magnetic and cosmic, radon, height attenuation corrected airborne radiometric data with coordinates of the flight lines obtained from GSI was formatted to suit Oasis Montage Geosoft software and processed for upward continuation, analytical signal, Euler deconvolution and 2-D modelling.

AEROMAGNETIC DATA INTERPRETATION

The total field magnetic intensity (TMI) map was computed from the aeromagnetic data as shown in Figure 3. A fault was identified GSI (https://bhukosh.gsi.gov.in**)** in the study area which is shown as a thick dark line from north western part to the central portion of the map. Figure 3 depicts a magnetic high that could be attributed to exposed formations in the area. These formations have been correlated with buried intrusive bodies and ferruginous sandstone in the north and north western region of the study area. Sharp linear gradients in the contours can be observed which could be inferred as lineaments at the contact of the formations. In addition, asymmetric anomalies are also present that could be interpreted as intrusive bodies. It can be observed from the total field magnetic intensity map (Figure 3) that the magnetic field intensity decreases gradually from north to south, which is the varying topography of the exposed formations and the underling sedimentary formation indicating a slope towards the southern region with increase in sedimentary thickness. The GSI reported probable near circular anomalies associated with kimberlite pipes in this area (marked with an arrow; Raynes et al., 2018).

The reduced-to-pole (RTP) (Figure 4) was computed from the TMI map (Figure 3) so that the asymmetrical nature of the anomaly would be converted to vertical magnetization for interpretation (Baranov, 1957; Baranov and Naudy, 1964; Silva, 1986; Hansen and Pawlowski, 1989; Telford et al., 1990; Mendonca and Silva 1993). Figure 4 shows an anomalous behavior in the magnetic field in the central part of the study area, which is probably depicting a reversal in the magnetic anomaly. This could probably be thought as a high magnetic mineral composite body (Raynes et al., 2018). It is also observed that at Hatnitor Pahar, the RTP map shows near circular anomalies in the RTP map (Figure 4). These near circular anomalies observed in the RTP map have been brought out when the map resolution was increased to highlight the anomalous zones.

The RTP map (Figure 4) has brought out the intrusive anomalies associated with kimberlites at Hatinitor Pahar, Kadwara, Kishangar, Moharkuwa and in the north-eastern part of the study area. The RTP map has enhanced the anomalies in the southern region of the map and also the central circular anomalies have been enhanced. A circular anomaly on the eastern side has been clearly brought out in the RTP map. These anomalies are presented superimposing the geological map on RTP map (Figure 5). The aeromagnetic anomalies in the north-eastern part (marked with a star; Figure 5) are associated with sedimentary formations, while the other anomalies are in hard rock terrain.

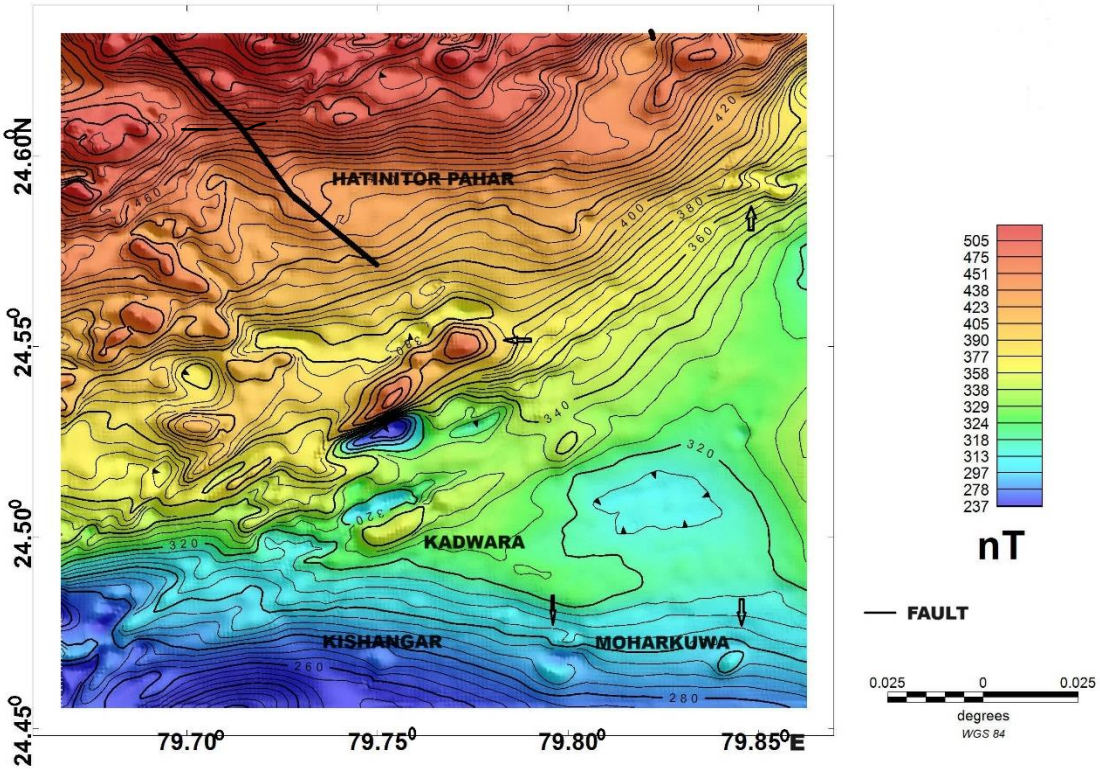

Figure 3. Total magnetic field anomaly (TMI) map as obtained from the aeromagnetic data of the study area

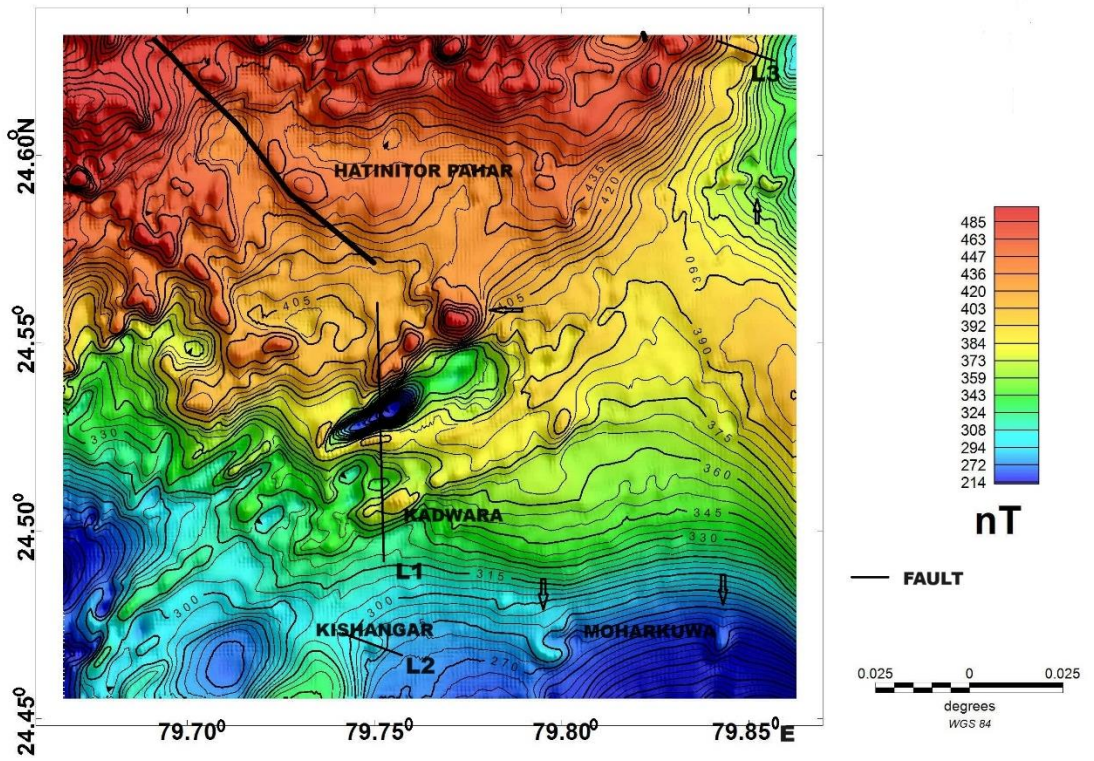

Figure 4. Reduce-to-pole map as obtained from aeromagnetic data of the study area

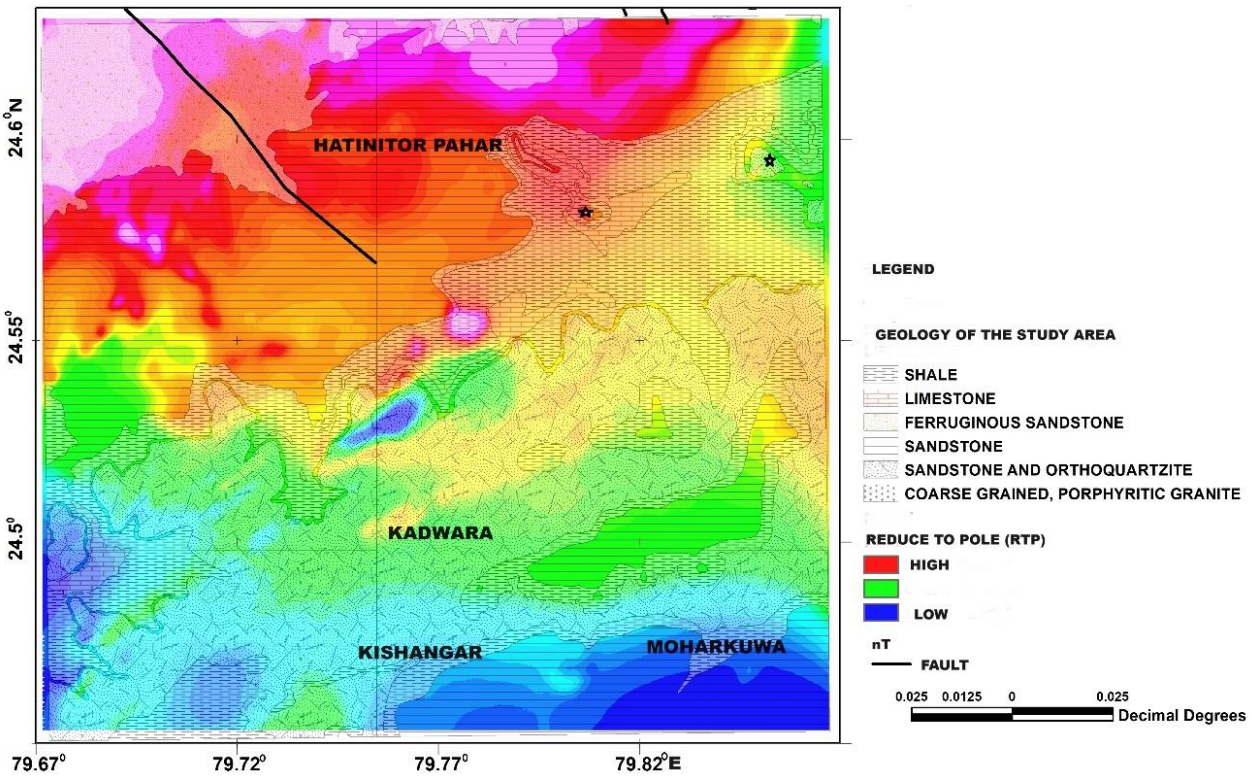

Figure 5. Geological map superimposed on RTP map of the study area

In order to further justify the interpretation of the anomalies inferred from the RTP map (Figure 4) upward continuation map was prepared at 100 m to ascertain the nature of the anomalies. The upward continuation map would help understand the anomalies as it would reduce the effects of cultural noise and long wavelength anomalies would be enhanced (Henderson and Zietz, 1949; Dean, 1958; Telford et al., 1990; Blakely, 1995). The depth of the kimberlite computed from Euler depth and inferred from drill logs is in the range of 60 m and 150 m in the Panna Diamond Belt (Mukherjee et. al., 2021). The depth to the probable kimberlite anomalies from magnetic modeling was found to be more than 150 m (Raynes et. al., 2018). In the present work, a depth of 100 m was chosen to compute the upward continuation map (Figure 6). Though the near circular anomalies represent the probable kimberlite pipes to have a deeper source than 100 m, however in order to identify the probable locations the upward continuation map was computed at 100 m.

To delineate the boundaries of magnetic sources (Nabighian, 1972; Keating and Sailhac, 2004) and for a higher resolution of magnetic sources (Roest et al., 1992; Rajagopalan, 2003) the analytical signal map was computed (Figure 7), which indicate a central high due to the presence of a probable magnetic intrusion and near circular anomalies surrounding this anomaly indicating probable kimberlite / lamproite pipe (Figure 7). In the north and western parts of the study area, the higher magnetic values are an indication of the presence of a shallow basement covered by sediments and intrusive bodies.

The Euler deconvolution solution (Figure 8) with a structural index (SI) of 2 shows a higher anomalous concentration at Hatinitor Pahar in the north-central region. The anomalous zone in the central part (Figure 7) is not associated with a SI for a pipe structure (Figure 8) and could be associated with a high magnetic intrusive source which was revealed in 2-D modeling presented in the next section.

The trend of the intrusive bodies was observed in the first vertical derivative map of aeromagnetic data (Figure 9). The strike direction is parallel to the strike direction of the contact zones (Figure 1). Along the fault the magnetic amplitudes are high at the Hatinitor Pahar and delineated as near circular anomalies in the RTP map (Figure 4). The near circular anomalies depicting the probable kimberlite pipes are also clearly brought out in the first vertical derivative map of the study area (Figure 9).

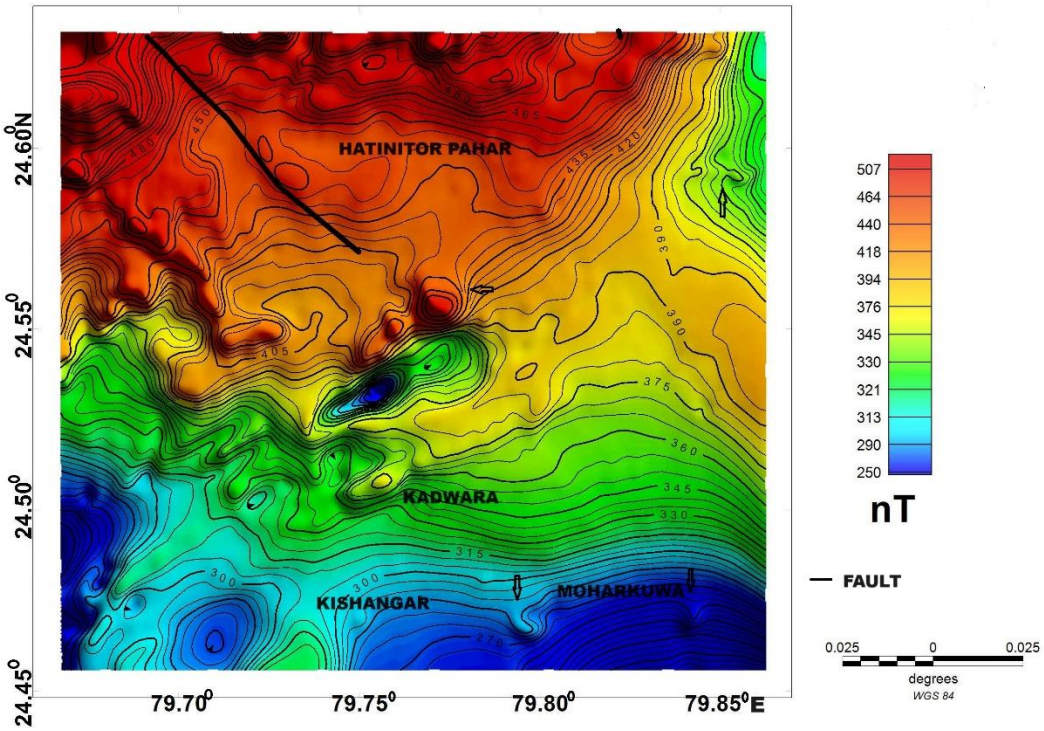

Figure 6. Upward continuation map at 100 m from aeromagnetic data of the study area

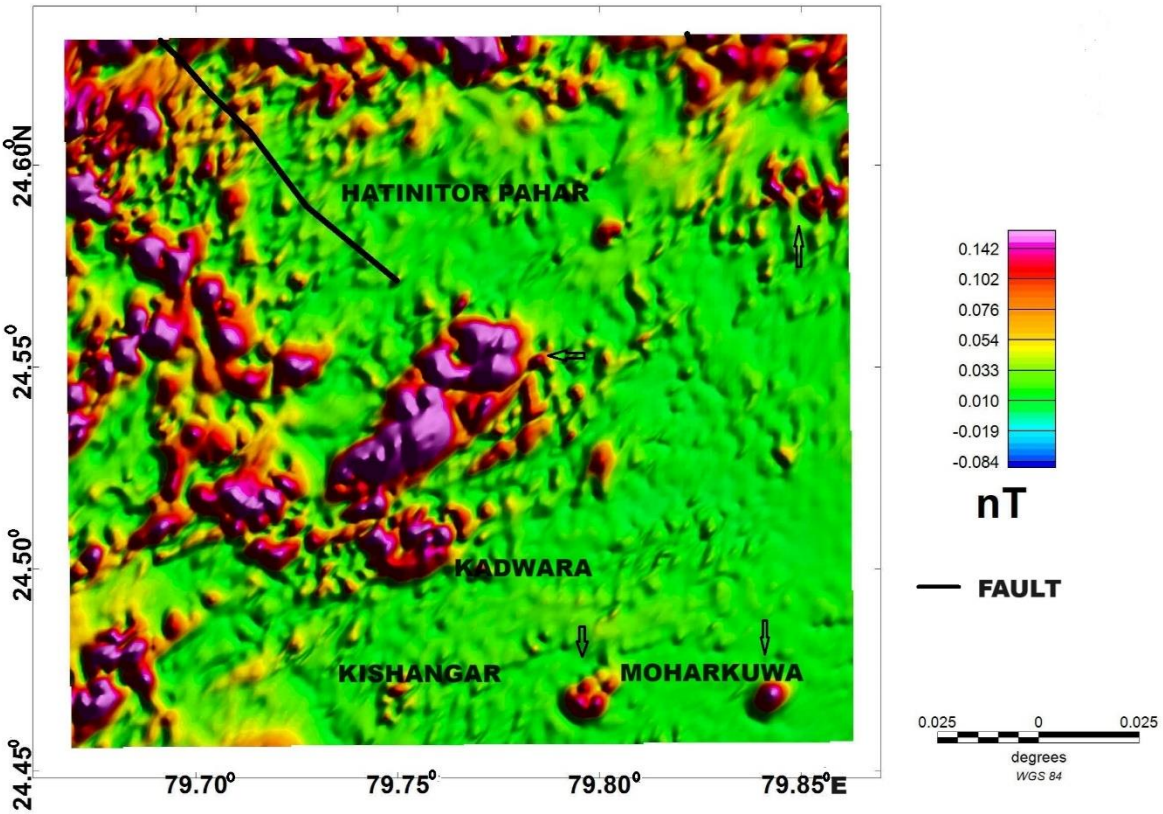

Figure 7. Analytical signal map of the study area

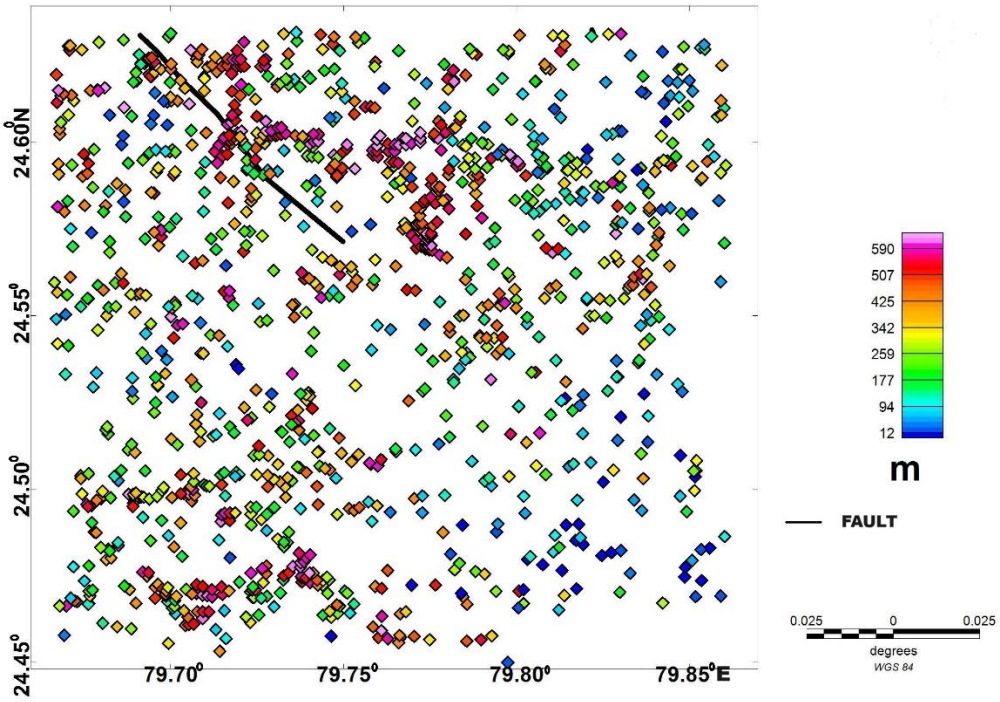

Figure 8. Euler deconvolution solutions with structural index of 2 for the study area

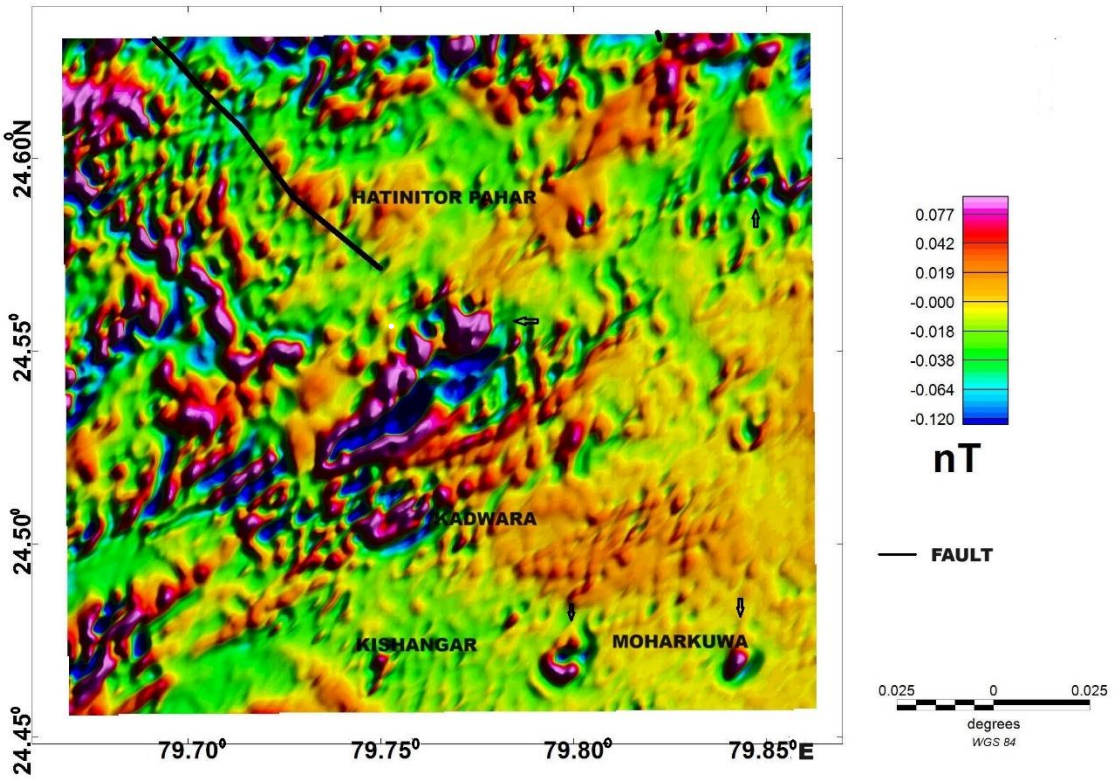

Figure 9. First vertical derivative map of the study area

MODELING OF AEROMAGNETIC ANOMALIES

A 2-D model (Figure 10) was generated across the central high magnetic anomalous zone as observed in the RTP map (Figure 4; Traverse L1) in north-south direction. A magnetic inclination of 50□, magnetization 0.0015 emu/cc and declination 5□ was considered for the 2-D model (Pradhan et al., 2012). A susceptibility of 0.025 SI for the sedimentary formations, 0.075 SI for the granitic basement and 0.052 SI units for the intrusive bodies was considered. The estimated depth of the central high magnetic and other intrusive bodies is observed to be approximately 350 m and 400 m respectively from the 2-D model (Figure 10).

For the near circular anomalies observed in the RTP map (Figure 4; Traverses L2 and L3) 2-D models (Figures 11 and 12) were prepared. The magnetic susceptibility range of 0.043 SI to 0.047 SI was considered for the probable kimberlites and the depth obtained was in the range of 200 to 250 m.

AIRBORNE RADIOMETRIC DATA ANALYSIS

Airborne radiometric surveys involve measuring the variation in percentage of elements such as uranium, thorium, and potassium in rock formations by spectral gamma ray detectors. Gamma ray penetration depth is less, hence the depth of investigation of this survey is not more than 30 cm so that the airborne radiometric data is useful for geological mapping (Kamara, 1981; Graham and Bonham-carter, 1993; Andrson and Nash, 1997; Charbonneau et al., 1997; Jaques et al.1997), soil mapping (Cook et al., 1996) and environmental radiation monitoring.

The potassium dissolved from the formation by weathering and erosional process is transported and accumulated in the surrounding formations. thorium and uranium elements are associated with oxide minerals in the rock formations. The percentage of these three elements may be high when the formation is rich in clay. Kimberlites can weather easily since kimberlites are ultrabasic intrusive rocks. The buried kimberlites fracture the overlying formation at the time of emplacement and these elements may accumulate in these fractures if pH is favorable for their deposition (Serra, 1984). A NE-SW anomalous trend was observed in the potassium anomaly map (Figure 13) in the study area, which is due of the exposed shale and alluvium deposits. The concentration of potassium is low at Hatinator Pahar and Moharkuwa (Figure 13) where thick sandstone formation was observed with a gentle slope, which is suitable for transporting the dissolved elements from the formations.

The trend of thorium anomalies (Figure 14) is similar to potassium anomalies but the anomalies of thorium are high in SW regions around Kadwara and Kishangar areas. Uranium anomalies (Figure 15) are behaving differently and which are sparse over the study area. The fault trend is well defined for all the element (potassium, uranium and thorium) concentrations. Kishangar, Kadwar, and Moharkuwa shown low concentration of these elements as the area may be disturbed by intensive fractures and these elements can easily be transported out from the formations.

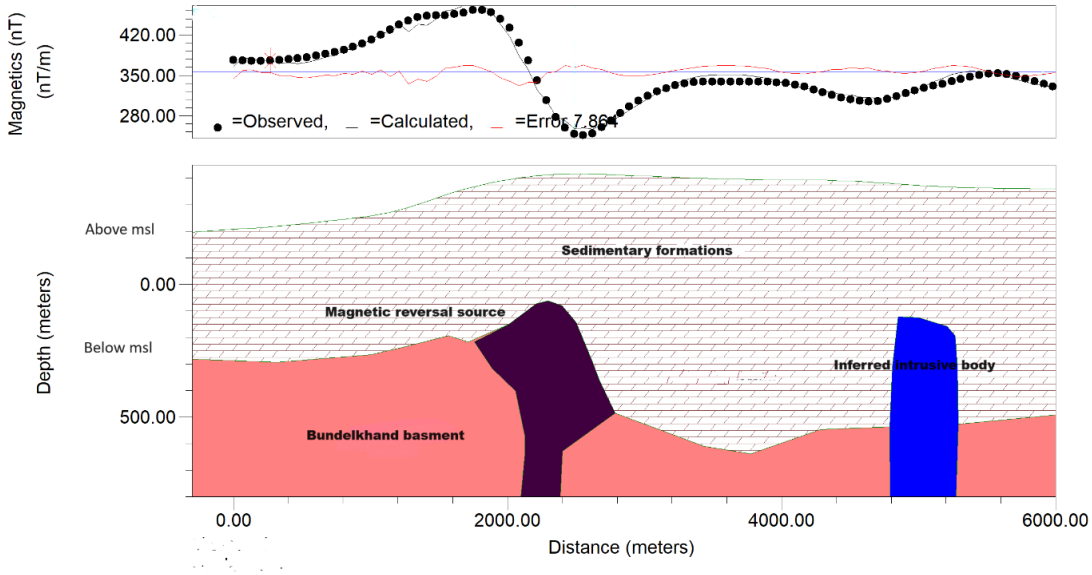

Figure 10. 2-D model across central magnetic high anomalous zone (Figure 4; L1)

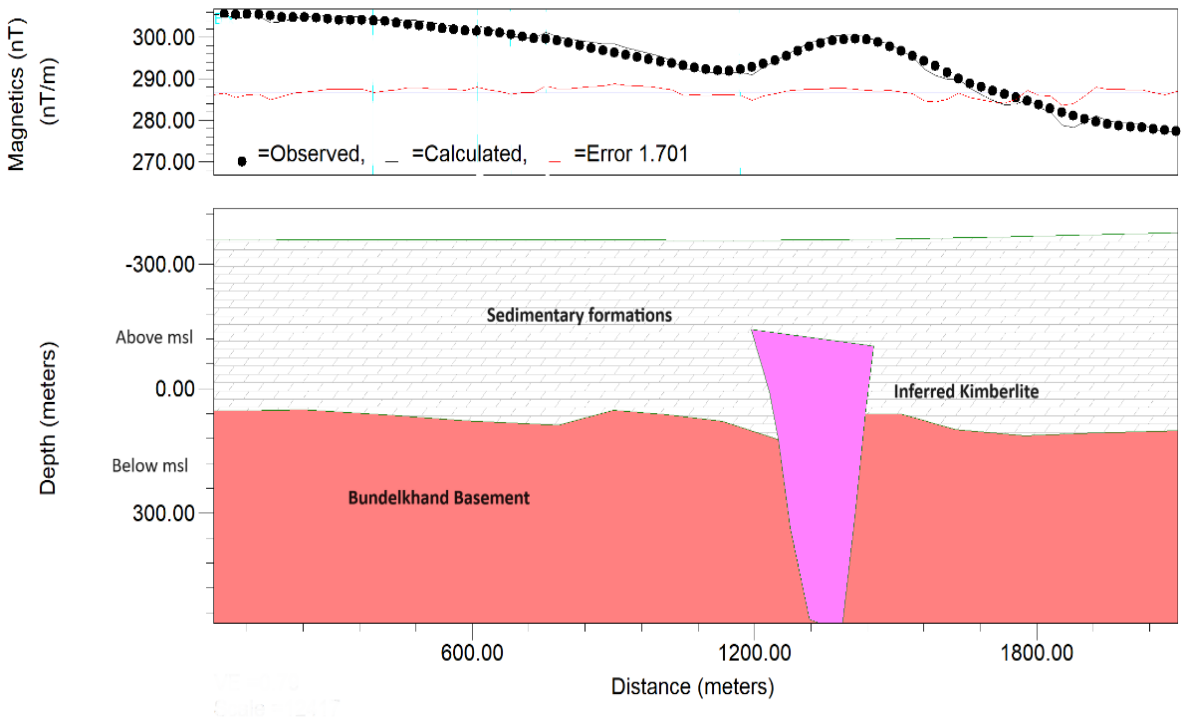

Figure 11. 2-D model across near circular magnetic anomaly (Figure 4; L2)

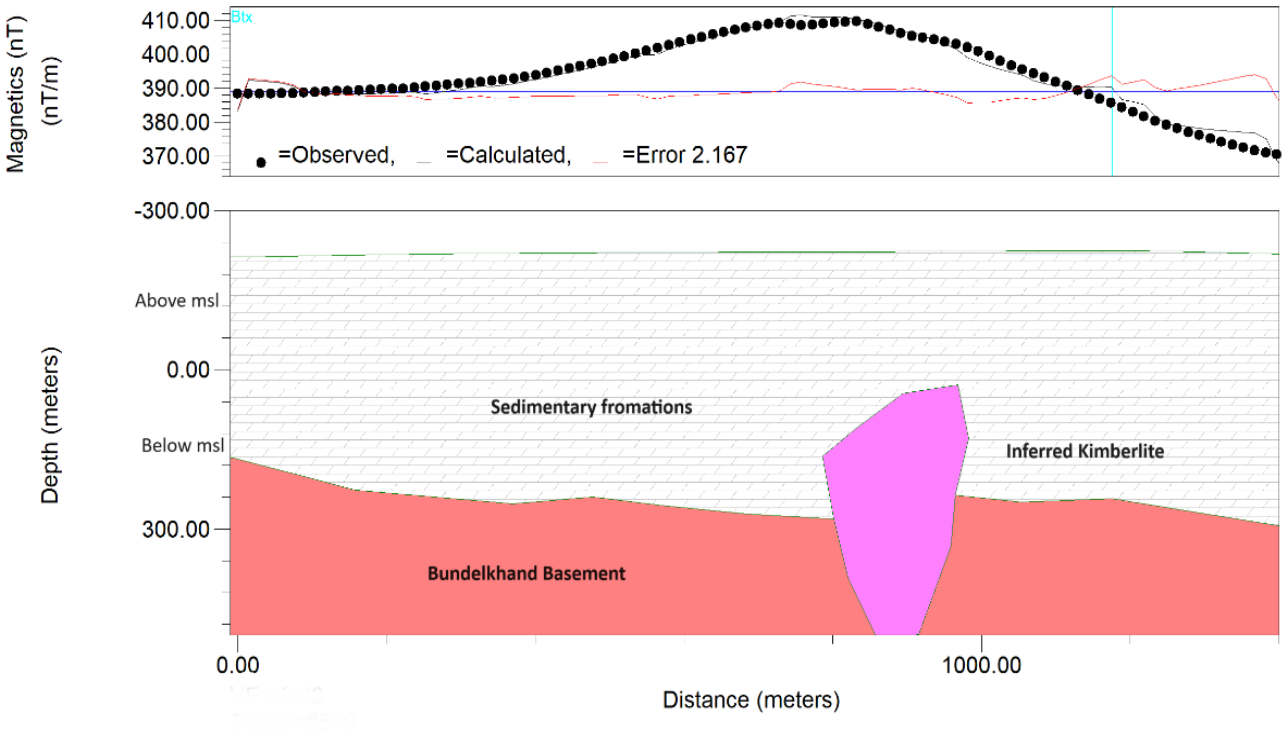

Figure 12. 2-D model across near circular magnetic anomaly (Figure 4; L3)

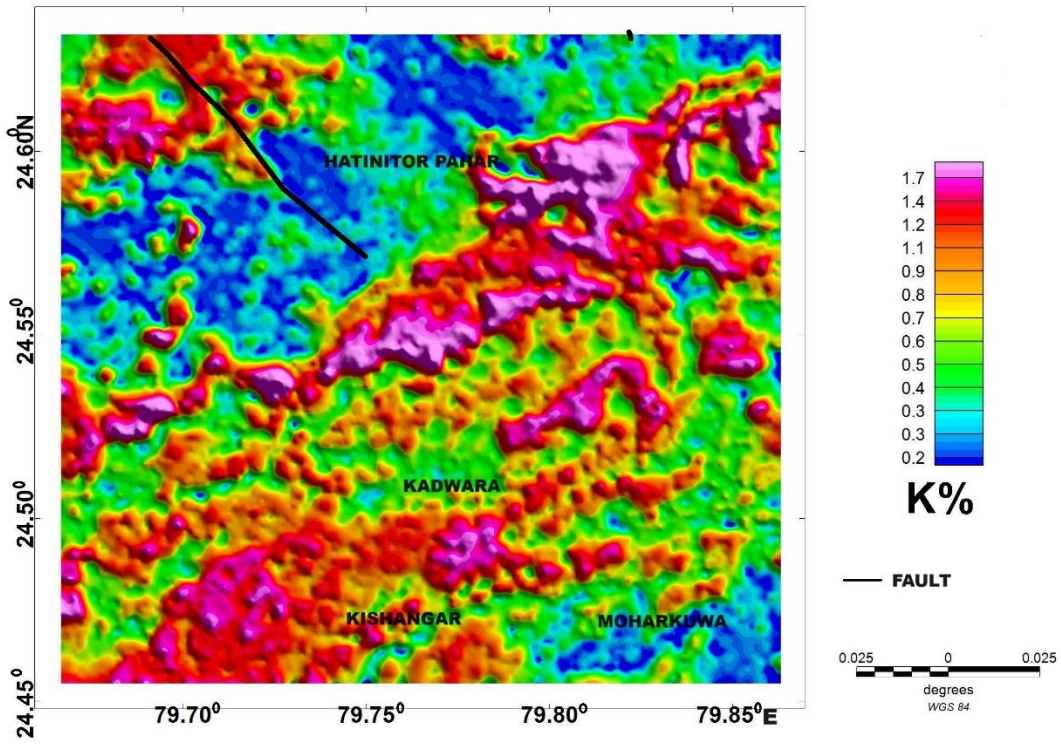

Figure 13. Potassium anomalies in the study area

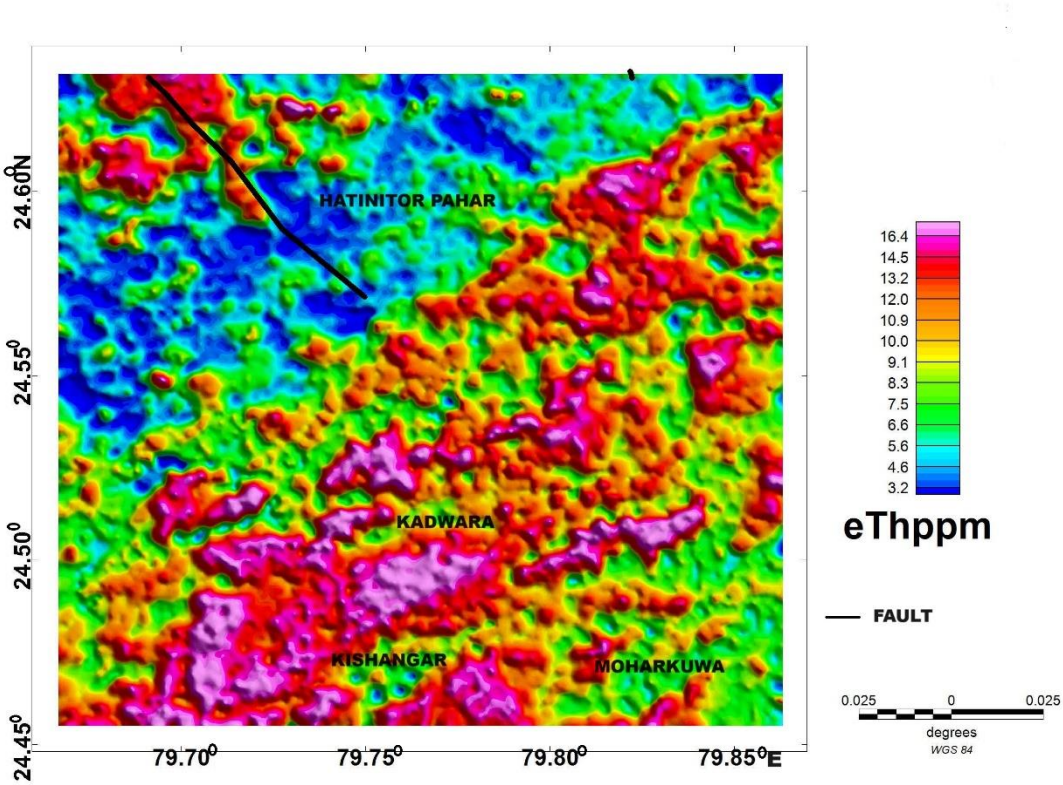

Figure 14. Thorium anomalies in the study area

The Ternay plot (Figure 16) shows the type of exposed formations and their trend as delineated by the element (potassium, uranium and thorium) concentrations. The anomalous behavior of these elements resembles the trend of the geological formations as observed in the geological map (Figure 1), though the thorium anomalies are strong at Kadwara, Moharkuwa and Kishangar areas.

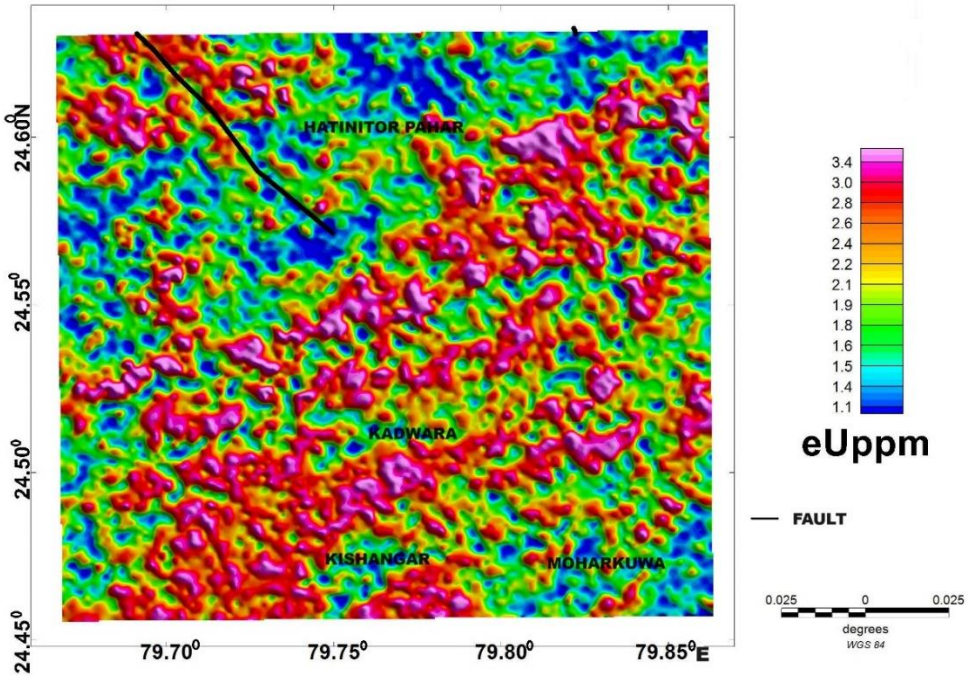

Figure 15. Uranium anomalies in the study area

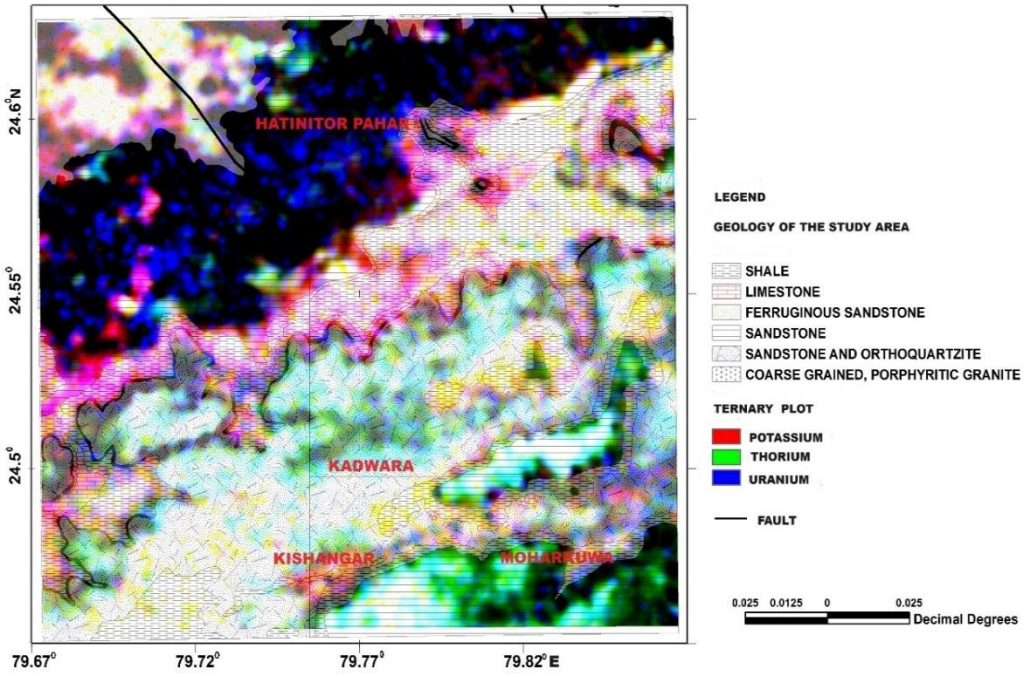

Figure 16. Ternary plot of the uranium, thorium and potassium anomalies superimposed on the geological map of the study area

DISCUSSION

The scale reduced aeromagnetic and airborne radiometric surveys have helped in identification of probable kimberlite zones with resemblance to kimberlite anomalies in the Panna Diamond Belt, at Kishangar, Kadwara and Hatinitor Pahar, which were not reported earlier by GSI. The Kishangar anomaly (Figure 3) shows an individual asymmetry which is deformed as a circular anomaly in the RTP map (Figure 4) with a diameter of around 350 m. Some near circular anomalies are enhanced in RTP map around the Hatinitor Pahar area. Analytical signal map (Figure 7) enhanced and separated the circular anomalies from the long wavelength anomalies. The aeromagnetic anomaly at Moharkuwa was marked (with an arrow) as a probable kimberlite zone with near circular anomalies (Raynes et al., 2018) by GSI. The 2-D modeling along profiles L2, L3 (Figure 4) across the two anomalies (Figures 11 and 12) have shown a depth of about 200 to 250 m with a diameter of about 250 m. The 2-D model along line L1 (Figure 4) was prepared across the central high magnetic anomaly, which was modelled as a high magnetic intrusive associated with a reversal.

In the ternary plot of the radiometric data (Figure 16), thorium anomalies show higher amplitudes at Kishangar, Kadwara, Moharkuwa where aeromagnetic data has shown probable locations for kimberlites (Figure 4). The presence of iron oxide on the surface or in deep fractures at Kishangar, Moharkuwa, Kadwara, could be the cause for the thorium anomalies.

CONCLUSIONS

From the observation of both reduced scale of aeromagnetic and airborne radiometric data, Hatinitor Pahar, and Kishangar in the Panna diamond belt have shown near circular anomalies with less than 500 m diameter in the RTP aeromagnetic map depicting locations of probable kimberlites which are not reported earlier by GSI. At Kadwara, a highly disturbed zone with intrusive bodies in magnetic data and with high thorium concentrations in the sandstone formation depicts the existence of a deep fracture that indicates the probable occurrence of kimberlite pipe. Also, the 2-D modelled data from the aeromagnetic map have revealed a high magnetic anomaly in the central region depicting a probable magnetic reversal.

ACKNOWLEDGEMENT

The authors express their thanks to Director General, Geological Survey of India (GSI), Kolkata and Deputy Director General, Remote Sensing Aerial Surveys, GSI, Bangalore for providing Diurnal and International Geomagnetic Reference Field (IGRF), flight heading, elevation, and lag corrected aeromagnetic and cosmic, radon, height attenuation corrected airborne radiometric data. Authors are thankful to the reviewers for their valuable comments for improving the article. Special thanks to chief editor of the journal Dr. O. P. Pandey for suggestions for improving the article.

Author Credit Statement

Jale Lingaswamy carried out the re-analysis of the airborne data. Ram Raj Mathur conceptualized the re-analysis of the geophysical data acquired from GSI and designed the study. He also contributed to the preparation of the manuscript. The findings were mutually discussed and analyzed by both the authors.

Data Availability Statement

The Diurnal, International Geomagnetic Reference Field (IGRF), flight heading, elevation, and lag corrected airborne magnetic and cosmic, radon, height attenuation corrected radiometric data is available with Director General, Geological Survey of India (GSI), Kolkata and Deputy Director General, Remote Sensing Aerial Surveys, GSI, Bangalore and can be made available on request. The data processed by the authors can be made available on reasonable request.

Compliance with Ethical Standards

The authors declare that they have no conflict of interest and adhere to copy right norms.

REFERENCES

Andrson, H. and Nash, C., 1997. Integrated litho-structural mapping of the Rossing area, Namibia using high resolution aeromagnetic, radiometric, Landsat data and aerial photographs. Expl. Geophys., 28, 185-191.

Baranov, V., 1957. A new method for interpretation of aeromagnetic maps: pseudo□gravimetric anomalies. Geophys., 22, 359-382.

Baranov, V. and Naudy, H., 1964. Numerical calculation of the formula of reduction to the magnetic pole. Geophys., 29, 67-79.

Bhattacharya, B., Raj J., Pimprikar S. D., Srivastava J. K., Tiwari M. and Ramtake P. F., 1995. Final report on special thematic mapping of Panna Diamond Belt, District Chhatarpur, Panna and Satna, Madhya Pradesh. GSI, Field Season Rep. 1990-95.

Blakely, R.J., 1995. Potential Theory in Gravity and Magnetic Applications, Cambridge University Press.

Charbonneau, B.W., Holman, P.B. and Hetu, R.J., 1997. Airborne gamma spectrometer magnetic-VLF survey of northeastern Alberta, In: Exploring for minerals in Alberta. Geological Survey of Canada Geoscience contributions, edited by MacQueen, Canada-Alberta agreement on mineral development. Geol. Sur. Can. Bulletin, 500, 107-132.

Cook, S.E., Corner, R.J., Groves, P.R. and Grealish, G.J., 1996. Use of airborne gamma radiometric data for soil mapping. Aust. J. Soil Res., 34, 183-194.

Crawford, A. R. and Compston W., 1970. The age of the Vindhyan system of peninsular India. J. Geol. Soc. Lond., 125, 351–371.

Dean, W.C., 1958. Frequency analysis for gravity and magnetic interpretation. Geophys., 23, 97–127.

Graham, D.F. and Bonham-carter, G.F., 1993. Airborne radiometric data: A tool for reconnaissance geological mapping using a GIS. Photogrammetric Engineering and Remote Sensing, 58, 1243-1249.

Guha, A., Rani, K., Varma, C. B., Sarwate, N. K., Sharma, N., Mukherjee, A., Kumar, K. V., Pal, S. K., Saw, A. K. and Jha, S. K., 2018. Identification of potential zones for kimberlite exploration – an earth observation approach. Int. Arch. Photogram. Remote Sens. Spatial Inf. Sci., XLII-5, 239–250.

Halder, D. and Ghosh D. B., 1978. Tectonics of kimberlites around Majhgawan, M.P., India. Geol. Surv. Ind. Misc. Publ., 34(3), 1–13.

Hansen, R.O. and Pawlowski, R. S., 1989. Reduction to the pole at low latitudes by Weiner filtering. Geophys., 543, 1607–1613.

Henderson, R.G. and Zietz, I., 1949. The upward continuation of anomalies in total magnetic intensity fields. Geophys., 14, 517–534.

Jaques, A.L., Wellman, P., Whitaker, A. and Wyborn, D., 1997. High resolution geophysics in modern geological mapping. AGSO J. Aus. Geol. and Geophys., 17, 159-174.

Kailasam, L. N., 1971. Geophysics in diamond exploration. Geol. Surv. Ind. Misc. Publ., 19, 60–68.

Kamara, A.Y.S., 1981. Review: Geophysical methods for kimberlite, prospecting. Expl. Geophys., 12, 43-51.

Keating, P.,1995. A simple technique to identify magnetic anomalies due to kimberlite pipes. Expl. and Min. Geol., 4(2), 121-125.

Keating, P. and Sailhac, P., 2004. Use of the analytic signal to identify magnetic anomalies due to kimberlite pipes. Geophys., 69(1), 180-190.

Krishnan, M. S. and Swaminath, J., 1959. The Great Vindhyan Basin of Northern India. J. Geol. Soc. Ind., 1959.

Kumar, S., Pal, S. K., Guha, A., Sahoo, S. D. and Mukherjee, A., 2020. New insights on Kimberlite emplacement around the Bundelkhand Craton using integrated satellite-based remote sensing, gravity and magnetic data. Geocarto. Int., 1–23.

Kusuma, K. N. and Ram Prasath, H.L, 2021. Application of Feature Based Principal Component Analysis (FPCA) technique on Landsat8 OLI multispectral data to map Kimberlite pipes. Ind. J. Sci. and Tech., 14(4), 361-372.

Lewis, H. C., 1887. On a diamondiferous peridotite and the genesis of the diamond. Geol. Mag., 4, 22–24.

Masun, K., Sthapak A.V., Singh A., Vaidya A. and Krishna C., 2009. Exploration history and geology of the diamondiferous ultramafic Saptarshi intrusions, Madhya Pradesh, India. Lithos, 112, 142-154.

Mathur, S.M., 1962. Geology of the Panna Diamond Deposits. Rec. Geol. Surv. Ind., 87, 4.

Mendonca, C. A. and Silva, B.C., 1993. A stable truncated series approximation of the reduction-to-the-pole operator. Geophys., 58, 1084–1090.

Mukherjee, A., Jha, S., Babu, E.V.S.S.K. and Verma, C.B., 2014. Discovery of a kimberlite pipe near Budikonda, Dharwar craton, south India: Field approaches, preliminary petrography and mineral chemistry. Ind. J. Geol. Soc., 84, 633-644.

Mukherjee, A., Mathur, R.R., Verma, C.B. and Tiwari, P.K., 2021. Gravity and magnetic surveys for kimberlite structures in Baghain and Rampura-Motwa, Panna Diamond Belt, Madhya Pradesh, India. Arab. J. Geosci., 14, 414, https://doi.org/10.1007/s12517-021-06760-w.

Nabighian, M. N., 1972. The analytic signal of two-dimensional magnetic bodies with polygonal cross-section: its properties and use for automated anomaly interpretation. Geophys., 37(3), 507-517.

Paul, D. K., Rex D. C. and Harris P. G., 1975. Chemical characteristics and K-Ar ages of Indian kimberlites. Amer. Geol. Soc. Bull., 86, 364–366.

Pradhan, V. R., Meert, J. G., Pandit, M. K., George, K. and Mondal, M. E. A., 2012. Paleomagnetic and geochronological studies of the mafic dyke swarms of Bundelkhand craton, central India: Implications for the tectonic evolution and paleogeographic reconstructions. Precam. Res., 198, 51-76.

Rajagopalan, S., 2003. Analytic signal vs. reduction to pole: solutions for low magnetic latitudes. ASEG Extended Abstracts, 2003(2),1 4. https://doi.org/ 10.1071/ ASEG 2003ab136.

Ramadass, G., Subhash Babu A. and Udaya Laxmi, G., 2015. Structural analysis of airborne radiometric data for identification of kimberlites in parts of Eastern Dharwar Craton. Int. J. Sci. and Res., 4(4), 2375-2380.

Rao, A. D. and Narayan, S. P. V., 1981. Structural control of emplacement of Kimberlite Pipes at Panna - A Suggestion from Aeromagnetic. Geo-exploration, 19, 207-228.

Rao, B. V. and Srinivasulu, T., 1999. Where and how of prospecting for diamonds in Andhra Pradesh, South India. J. Geophys., 20, 103-116.

Rao N. V. C., 2006. Mesoproterozoic diamondiferous ultramafic pipes at Majhgawan and Hinota, Panna area, central India: Key to the nature of sub-continental lithospheric mantle beneath the Vindhyan basin. J. Earth. Syst. Sci., 115, 161–183.

Rao, R. C., Kishore, R. K., Kumar, V. P. and Babu, B. B., 2011. Delineation of intra crustal horizon in Eastern Dharwar Craton–Aeromagnetic evidence. Asian. J. Earth. Sci., 40(2), 534-541.

Rasmussen, B., Bose P. K., Sarkar, S., Banerjee S., Fletcher, I. R. and McNaughton N. J., 2002. 1.6 Ga U-Pb zircon age for the Chorhat Sandstone, lower Vindhyan, India: Possible implications for early evolution of animals. Geol., 30 (2) 103–106.

Ray, J. S., Veizer J. and Davis W. J., 2003. C, O, Sr and Pb isotope systematics of carbonate sequences of the Vindhyan Super Group, India: age, diagenesis, correlations and implications for global events. Precamb. Res., 121, 103–140.

Raynes, C., Allois, C., Kozhamsugirov, D., Makhmuduly, M.and Poletti, A., 2018. Multi-sensor Aerogeophysical Surveys over Obvious Geological Potential (OGP) Areas of India, Block-2, Data Interpretation Report submitted by Geoken-Helica-Secon for Geol. Sur. Ind., December 2018.

Roest, W. R., Verhoef, J., and Pilkington, M., 1992. Magnetic interpretation using the 3-D analytic signal. Geophys., 57, 116–125.

Sarkar, A., Trivedi, J. R., Gopalan, K., Singh, P. N., Das, A. K. and Paul, D. K., 1984. Rb-Sr geochronology of the Bundelkhand granitic complex in the Jhansi-Babina-Talbehat sector, India. Ind. J. Earth. Sci., UP, 64–72.

Sarma, B.S.P., Verma, B. K. and Satyanarayana, S, V., 1999. Magnetic mapping of Majhgawan diamond pipe of Central India. Geophys., 64 (6), 1735-1739.

Sarma, B. S. P. and Verma, B. K., 2001. Aeromagnetic lineaments, basement structure and Kimberlite emplacement in Andhra Pradesh, India. Geophys. Res. Lett., 28(22), 4307-4310.

Serra, O., 1984. Fundamentals of well- log interpretation, Developments in Petroleum Science,15A, University of Illinois at Urbana-Champaign. Elsevier, 95-106

Sharma, R., Murthy, Ch.V.V.S., Nagaraju, B. V., Gouda, H.C. and Singh, R. K., 2007, Interpretation of Aeromagnetic data of Panna and adjoining area, parts of M.P. & U.P., for evaluation of structural patterns favourable for emplacement of kimberlite clan of rocks and estimation of magnetic bodies. Ind. J. Geol. Surv., 69 (3) 653-663.

.Silva, J. B. C., 1986. Reduction to the pole as an inverse problem and its application to low-latitude anomalies. Geophys., 51,369–382.

Srivastava, A. P. and Rajagopalan, G., 1988. FT ages of Vindhyan glauconitic sandstone beds exposed around Rawatbhata area, Rajasthan. J. Geol. Soci. Ind., 32(6), 527-529.

Singh, V.K. and Slabunov, 2016. A Two types of Archaean supracrustal belts in the Bundelkhand craton, India: geology, geochemistry, age and implication for craton crustal evolution. J. Geol. Soc. Ind., 88, 539.

Telford, W. M., Geldart, L. P. and Sheriff, R. E., 1990. Applied geophysics. Cambridge University Press, Cambridge, 2nd Edition, 109.

Tessema, A., Nefale, N. and Sebake, D., 2012. The use of high-resolution airborne magnetic, ASTER and Landsat 7 ETM+ images for identification of kimberlite pipes in the northwestern Free State Province, South Africa. Int. J. Remote. Sens., 33(14), 4356-4373.

Vinogradov, A.P., Tugarinov, A.I., Zhykov, C., Stapnikova, N., Bibikova, E. and Khorre, K., 1964. Geochronology of Indian Pre-Cambrian: Int. Geol. Cong., 22nd, 10, 553–567.

Received on: 12-06-2024 ; Revised on: 06-08-2024; Accepted on: 07-08-2024

J. Ind. Geophys. Union, 28(5) (2024), 329-340

Ascertaining erosion potential of watersheds by utilizing Fuzzy Analytical Hierarchy Process (FAHP) and morphometric parameters of the Savitri River basin (Maharashtra), India

Durugwar Yogeshkumar*, Pekam Swapnil and Kulkarni Dhaval
School of Earth Sciences, Punyashlok Ahilyadevi Holkar Solapur University, Solapur-413255, India
*Corresponding author: yogesh.durugwar@gmail.com

ABSTRACT

Weathering and erosion are geological phenomenon carried out by different geological agents. In the context of peninsular India, where aeolian and fluvial erosion processes exert significant influence within river basins, the assessment of erosion risk factors necessitates a methodical approach. Prioritizing watersheds based on morphometric parameters emerges as a crucial method, serving as a proficient pre-requisite for implementing effective conservation measures. In Western Ghat, Savitri River basin originates from the Sahyadri mountain range which merges into the Arabian Sea. It is west flowing river having small catchment area and rapid water movement due to high relief. In the present study, prioritization of sub-watersheds in the Savitri River basin has been done using morphometric parameters and a multi-criteria decision support model. The MCDSM used fuzzy analytical hierarchy process to categorize and prioritize land erosion. The morphometric parameters of Savitri River's six sub-watersheds with respect to their linear, areal, and relief characteristics have been quantified. Further, FAHP weights were applied to such parameters for ranking of the sub-watersheds in order to work out their hydrological and topographical attributes. Subsequently, FAHP scores were employed to categorize the sub-watersheds into three priority levels (high, medium, and low) for soil conservation and management within the Savitri River basin, encompassing an area of approximately 2268.92 Km^2. Utilizing the FAHP model in conjunction with drainage morphometry and Geographic Information System techniques, enabled the effective identification and prioritization of critical sub-watersheds, thereby enhancing overall watershed management strategies.

Keywords: Morphometric parameters, Prioritization, Fuzzy Analytical Hierarchy Process, Savitri River basin, Soil erosion.

Abbreviations: AHP: Analytic Hierarchy Process, DEM: Digital Elevation Model, FAHP: Fuzzy Analytical Hierarchy Process, GIS: Geographical Information System, IDW: Inverse Distance Weighting, IMD: Indian Meteorological Department, MCDSM: Multicriteria decision support model, MSL: Mean Sea Level, NRSC: National Remote Sensing Centre, TFN: Triangular Fuzzy Numbers

INTRODUCTION

It has become increasingly apparent that ensuring food security in the future is imperative, given the continuous growth of the global population. Effectively developing, utilizing, and managing water and land resources must be undertaken in a comprehensive and integrated manner to ensure effective development, utilization, and management. Watershed conservation measures can play a crucial role in holistic management of land and water resources, which have been widely, accepted (Biswas et al., 1999). In developed countries like India, where a significant portion of the population relies on agriculture, the management and development of watersheds to prevent soil erosion are crucial. River basin studies play a vital role in this regard, employing quantitative morphometric parameters, as outlined by Strahler (1964).

In contemporary times, GIS offer a more efficient and time-saving method for analyzing the characteristics of surface drainage networks, utilizing a numerical physiographic methodology (Horton, 1945; Abrahams, 1984; Thakkar and Dhiman, 2007; Aher et al., 2013; Rahaman et al., 2015; Mishra and Siddi Raju, 2024). The river basin, delineated by natural boundaries and regarded as a geomorphological unit, presents a rational selection for conducting morphometric analysis. These analyses are pivotal for quantifying and elucidating the hydrological and geological attributes inherent to watersheds. Hence, morphometric investigation contributes significantly to tasks such as watershed demarcation, modeling, prioritization, river basin assessment, and the management of natural resources (Khan et al., 2001; Suresh et al., 2004; Magesh et al., 2010; Thomas et al., 2012; Tiwari and Srinivas, 2023).

In any given region, drainage basin configurations are shaped by a variety of factors, including the topography, bedrock lithology, geological formations, and prevailing climate, all of which collectively determine their distinctive characteristics. In order to inform decision-making within various domains, it is necessary to conduct quantitative analyses and explore their interrelationships. In addition, these domains include the management and assessment of water resources, as well as their use for soil conservation on a watershed scale (Ogunkoya and Jeje, 1987). It is relatively straightforward to describe basin features using hydro-morphometric descriptors, and understand their impact on erosion processes. As a result of these descriptors, basin characteristics can be compared, shedding light on the geomorphic history of the drainage basin (Strahler, 1964; Biswas et al., 1999;). Horton (1945) formulated the first quantitative analysis of drainage basins, and Strahler (1964) refined it. Further, spatial information analysis and

representation are made easier with GIS (Das and Mukherjee, 2005, Manjare et al., 2014, Shrivatra et al., 2021). In recent years, researchers have also attempted to prioritize watersheds through multi-criteria assessment using the fuzzy analytical hierarchy process (Aher et al., 2013). When evaluating susceptibility contributing factors within a result obtaining process, multiple criteria and alternatives must be taken into account.

The present research has been undertaken keeping in view the dire need for efficient management of water and land resources to achieve soil conservation. In a country like India, wherein a good percentage of its economy is agrarian, the potential for erosion can only be understood and reduced by conserving watersheds. The techniques developed so far for estimating erosion have lots of scope for improvement; thus, this study presents a novel approach for the same through the study by Fuzzy Analytical Hierarchy Process (FAHP) with the help of GIS. This methodology is undertaken basically for the prioritization of the Savitri River basin and its sub-watersheds with a view to erosion potential assessment and resource conservation.

STUDY AREA

Savitri River basin is located at the base of the Sahyadri mountain escarpment. It extends between 17°51'N to 18°26N and 73°1'E to 73°41'E encompassing an area of 2268.92 km^2 with perimeter 305.36 km as shown in Figure 1. It includes two districts Raigad and Ratnagiri covering 7 talukas. The watershed exhibits elevations from 3 meter to a maximum of 1317 meters from MSL. Study area relates to toposheets 47F/03, 47F/04, 47F/07, 47F/08, 47F/11, 47F/12, 47G/05, 47G/09, and 47G/11 of the Survey of India at a scale of 1:50000. Hydrological boundaries, which include watershed and sub-watershed boundaries, have been defined based on the drainage network and the data given in Table-1. Savitri River originate from Savitri Point, Mahabaleshwar, which is one of the top of Sahyadri mountain range and fed at Bankot creek, Near Harihareshwar, Konkan, Arabian Sea, having an average length of 110 km. The basin's geographical region experiences a tropical climate typified by a dominant monsoon phase spanning approximately four months, from June to October. The monsoon season is the wettest time of the year, with little precipitation observed in other months.

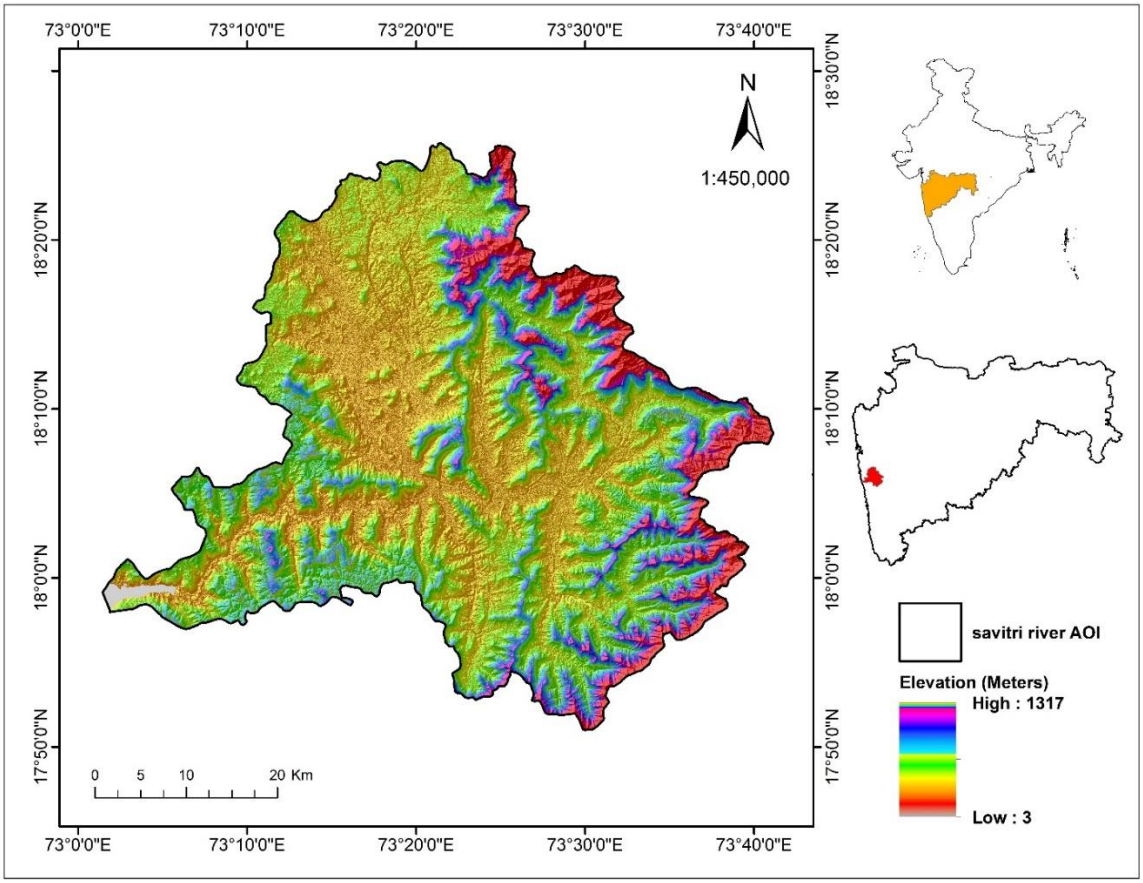

Figure 1. Map showing location of the Savitri River basin in Maharashtra (India)

Table 1. Sub-watershed of Savitri River basin

Savitri subbasin	Area (km^2)	Perimeter (km)	Tributaries
SSB1	457.22	124.8	Kalbhaoviranadi
SSB 2	363.17	99.3	Upper Savitri river
SSB 3	150.42	62.5	Nageshrinadi
SSB 4	208.94	76.0	Gandhari river
SSB 5	691.07	139.2	Kal nadi
SSB 6	398.10	121.1	Savitri river higher order
Total Area	2268.92 Sq. km.		

Table 2. Monthly rainfall (in mm) recorded at the Savitri River basin rain gauge stations between 2016 and 2021

Months/Year	2016	2017	2018	2019	2020	2021
January	0	0	0	0	0	9.58
February	0.01	0	0	0	0	20.2
March	4.25	0	0.09	0.03	6.13	3.03
April	1.09	0.03	8.66	4.68	2.6	5.06
May	11.77	36.74	5.62	0	9.08	104.4
June	569.1	901.24	811.3	628.52	510.58	770.52
July	1470.06	1445.55	1564.71	2015.44	583.74	1463.83
August	1173.17	922.27	795.11	1400.36	1783.43	384.14
September	753.16	540.56	162.8	1218.71	376.97	683.12
October	112.44	172.17	60.48	213.32	233.52	104.85
November	0	2.27	29.5	35.2	1.11	38.38
December	0	21.91	0	0.35	10.59	11.92

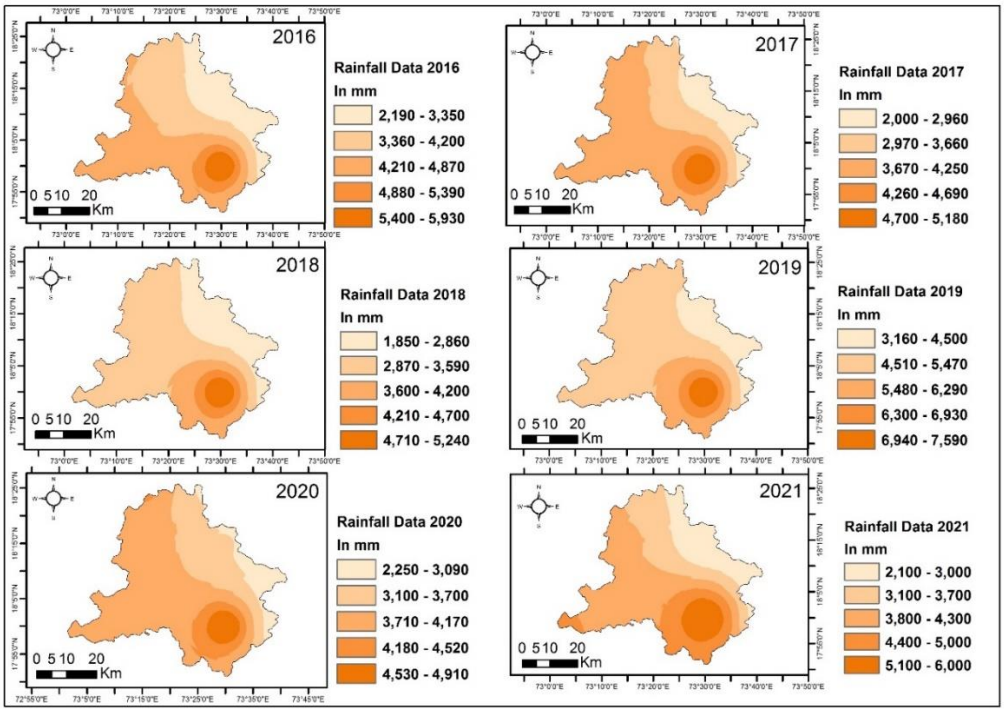

Figure 2. Map showing rainfall intensity of the study area.

METHODOLOGY

Morphometric Analysis

In this study, we performed drainage morphometry using geospatial techniques. The drainage network was delineated using Survey of India topographic maps (47F/03, 47F/04, 47F/07, 47F/08, 47F/11, 47F/12, 47G/05, 47G/09, and 47G/11). The Savitri River basin was divided into six sub-watershed (Kalbhaovira nadi, Upper Savitri River, Nageshri nadi, Gandhari river, Kal nadi and Savitri River higher order) namely, SSB1, SSB 2, SSB 3, SSB 4, SSB 5 and SSB 6, the details of which being given in Table 1.

A Digital Elevation Model (DEM) of Cartosat-1, with a spatial resolution of 10 m, was obtained from NRSC Hyderabad. Data from this source was used to create raster layers pertaining to the study area. The rainfall data was taken from Indian Meteorological department (IMD) for the period 2016 to 2021 as given in Table 2, which was converted into Inverse Distance Weighting (IDW) grid data, as shown in Figure 2. The DEM data was used for the determination of flow direction at the surface and accumulation of water using hydrological tools. Figure 3 shows the drainage order and drainage density of the study area. In this research work, the drainage morphometry parameters like linear, aerial, and relief have been calculated using the standard formulae as mentioned in Table 3. Using the contour lines and the flow direction of drainage, the sub-watershed boundaries were demarcated. Utilizing ArcGIS 10.0 software, non-spatial attributes of the sub-watersheds were computed, encompassing parameters such as stream order, stream length, area, perimeter, basin length, etc. Microsoft Excel was used to calculate morphometric parameters. A Fuzzy-AHP was used to manually calculate weights for the morphometric parameters. Detailed morphometric characteristics of each sub-watershed, including areal, linear, and relief, are presented in Table 4. In order to assess erosion risk, the FAHP method was used to weight the morphometric parameters of the sub-watersheds.

Table 3. Equation used to calculate morphometric parameters.

Count	Morphometric parameters	Definition/Formula/ Methods	Source
Linear			
1.	Stream order	Hierarchical rank	Strahler (1964)
2.	Stream no. (Nu)	Total number of streams in each order within a basin	Horton (1945)
3.	Stream length (Lu)	Length of the stream	Strahler (1964)
4.	Mean stream length	Lsm = Lu/Nu (Lsm = mean stream length; Lu = total stream length of a given order; and Nu = total no. of stream segments of a given order)	Horton (1945)
5.	Stream length ratio	RL = Lu/Lu-1 (RL = stream length ratio; Lu = total stream length of a given order; and Lu-1=total stream length of its next lower order)	Schumm (1956)
6.	Bifurcation ratio	Rb = Nu/Nu + 1 (Rb = bifurcation ratio; Nu = total no. of stream segments of a given order; and Nu + 1=no. of segments of the next higher order)	Strahler (1957)
7.	Mean bifurcation ratio	Rbm = average of bifurcation ratios of all orders	Strahler (1964)
Areal			
8.	Drainage density	Dd = Lu/A (D = drainage density; Lu = total stream length of all orders; and A = area of the Basin)	Horton (1932)
9.	Stream frequency	Fs = Nu/A (Fs = drainage frequency; Nu = total no. of streams of all orders; and A = area of the basin)	Horton (1932)
10.	Drainage texture	Rt = Nu/P (Rt = drainage texture; Nu = total no. of streams of all orders; and P = perimeter of the basin)	Horton (1945)
11.	Infiltration no.	If = Rt X Fs (If = infiltration no.; Rt = drainage texture; and Fs = drainage frequency)	Faniran (1969)
12.	Length of overland flow	Lg = 1/Dd (Lg = length of overland flow and Dd = drainage density)	Horton (1945)
13.	Circulatory ratio	$Rc = 4pA/P^2$ (Rc = circularity ratio. p = 3.14; A = area of the basin; and P^2 = square of the perimeter)	Miller (1953)
14.	Form factor	$Rf = A/Lb^2$ (Rf = form factor; A = area of the basin; and Lb^2 = square of basin length)	Horton (1932)
15.	Elongation ratio	$Re = 2* (A/p)^{0.5}/Lb$ (Re = elongation ratio; A = area of the basin; p = 3.14; and Lb = basin length)	Schumm (1956)
Relief			
16.	Relief	(Elevation of basin mouth) - (Elevation of highest point on the basin)	Strahler (1952)
17.	Relief ratio	Rh = H/Lb (Rh = relief ratio; H = total relief (relative relief) of the basin in km; and Lb = basin length)	Schumm (1956)
18.	Ruggedness no.	Rn = Dd*H/1000 (Rn = ruggedness no.; Dd = drainage density; and H = watershed relief)	Strahler (1964)

Table 4.Findings from the morphometric analysis of the sub-watershed

Morphometric Factors	SSB 1	SSB 2	SSB 3	SSB 4	SSB 5	SSB 6	Savitri River basin
Stream order	6th	6th	5th	7th	7th	8th	8th
Stream no. (Nu)							
1st order	1841	1457	519	2179	2232	1219	8547
2nd order	426	339	120	326	537	267	2015
3rd order	85	79	29	73	117	66	449
4th order	21	17	8	12	27	16	101
5th order	4	3	1	3	8	2	21
6th order	1	1	-	1	2	-	5
7th order	-	-	-	1	1	-	2
8th order	-	-	-	-	-	1	1
Stream length (Lu) km							
1st order	1073.63	787.95	276.67	641.40	1333.88	653.85	4767.38
2nd order	254.45	201.61	68.14	161.05	402.81	196.67	1284.73
3rd order	118.98	98.77	51.96	78.34	195.66	98.46	642.17
4th order	73.06	71.14	19.43	40.85	100.79	49.19	354.46
5th order	34.02	20.13	21.37	18.94	62.32	11.96	168.75
6th order	29.24	27.17	-	2.32	15.90	-	74.63
7th order	-	-	-	15.90	20.99	-	36.89
8th order	-	-	-	-	-	43.95	43.95
Overall mean stream length (Lsm)	7.30	6.74	5.34	4.26	6.21	9.29	11.44
Stream Length Ratio (Rl)							
2/1	1.02	1.10	1.07	1.68	1.26	1.37	1.14
3/2	2.34	2.10	3.16	2.17	2.23	2.03	2.24
4/3	2.49	3.35	1.36	3.17	2.23	2.06	2.45
5/4	2.44	1.60	8.80	1.85	2.09	1.95	2.29
6/5	3.44	4.05	-	0.37	1.02	-	1.86
7/6	-	-	-	6.85	2.64	-	1.24
8/7	-	-	-	-	-	-	2.38
Bifurcation Ratio (Rb)							
1/2	4.32	4.30	4.33	6.68	4.16	4.57	4.24
2/3	5.01	4.29	4.14	4.47	4.59	4.05	4.49
3/4	4.05	4.65	3.63	6.08	4.33	4.13	4.45
4/5	5.25	5.67	8.00	4.00	3.38	8.00	4.81
5/6	4.00	3.00	-	3.00	4.00	-	4.20
6/7	-	-	-	1.00	2.00	-	2.50
7/8	-	-	-	-	-	-	2.00
Mean bifurcation ratio (Rbm)	4.53	4.38	5.02	4.21	3.74	4.55	3.81
Perimeter (P) (km)	124.8	99.26	62.48	76	139.16	121.05	305.36
Area (A) (Sq.km)	457.22	363.17	150.42	208.94	691.07	398.1	2268.92
Drainage density (Dd)	3.46	3.32	2.91	4.59	3.09	2.54	3.23
Stream frequency (Fs)	5.20	5.22	4.50	12.42	4.23	3.95	4.91
Drainage texture (Rt)	19.05	19.10	10.84	34.14	21.01	12.98	36.48
Infiltration no. (If)	99.10	99.72	48.77	424.07	88.90	51.21	179.15
Length of overland flow (Lg)	0.29	0.30	0.34	0.22	0.32	0.39	0.31
Circulatory ratio (Rc)	0.37	0.46	0.48	0.45	0.45	0.34	0.31
Form factor (Rf)	0.37	0.63	0.29	0.25	0.55	0.30	0.44
Elongation ratio (Re)	0.69	0.90	0.61	0.57	0.84	0.62	0.75
Relative relief	1065	1280	1295	754	952	402	1297
Relief ratio (Rh)	30.25	53.33	57.05	26.26	0.45	11.10	17.98
Ruggedness no. (Rn)	3.68	4.25	3.77	3.46	2.94	1.02	4.19

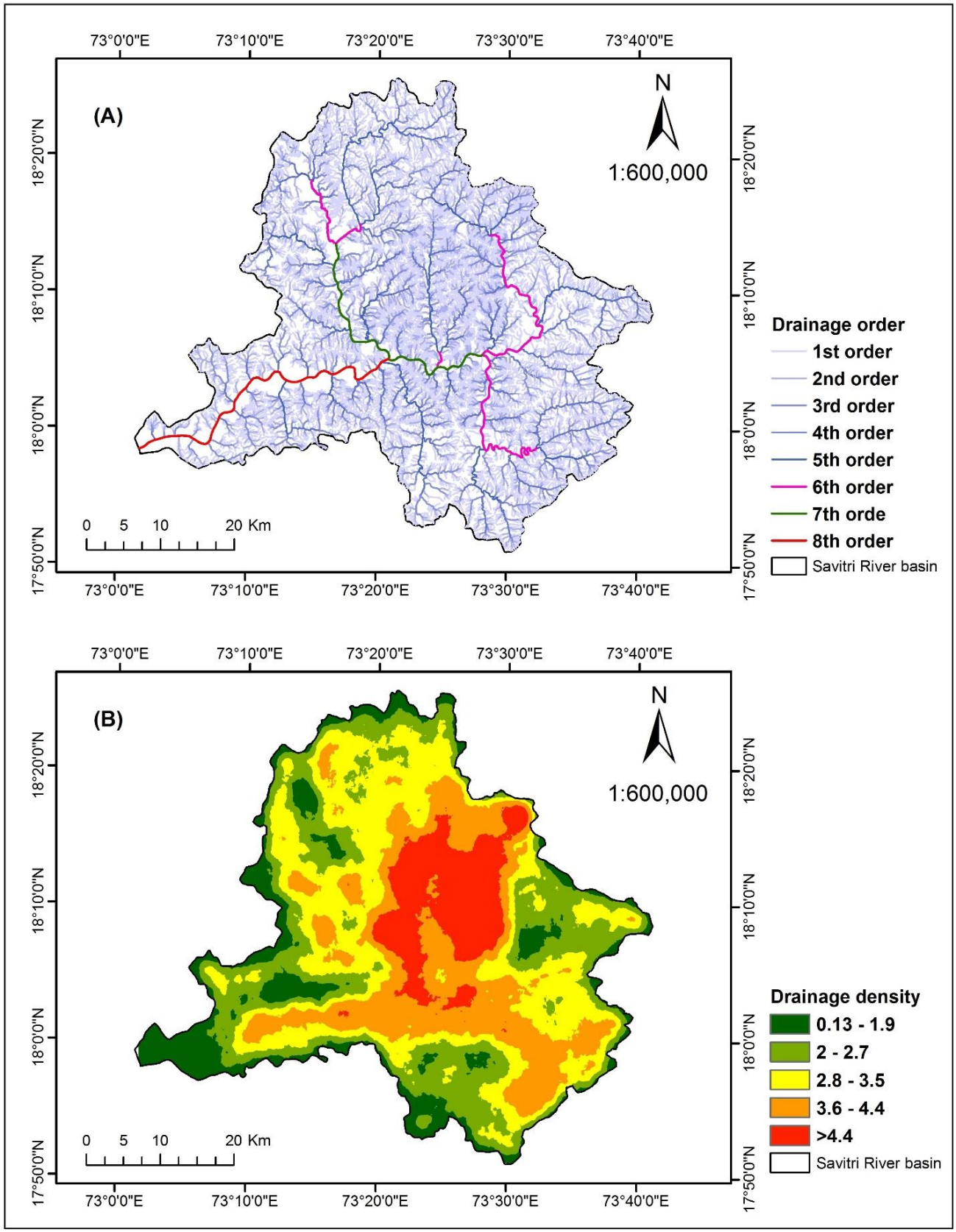

Figure 3. Map showing **(A)** drainage order and **(B)** drainage density in the study area.

Prioritization of sub-watershed using FAHP

Different methods were used by several researchers to prepare the prioritized watershed, including quantitative, fuzzy logic, statistic methods, and Analytical Hierarchy Process (AHP). To prioritize watersheds, Fuzzy Analytical Hierarchical Process (FAHP) was used with extent analysis. Specifically in spatial and GIS-based problems, the Analytical Hierarchy Process (AHP) can be used as a decision-making tool based on multiple criteria developed by Saaty(1980) by using a subjective approach where weights are allocated based on pair-wise comparisons of diverse criteria. In MCDSM (Multicriteria Decision Support Model), multiple criteria are evaluated in order to achieve an optimal solution while addressing the uncertainties inherent to the criterion evaluation process. The application methodology, strengths, and weaknesses of AHP are deliberated upon, alongside the introduction of the Fuzzy Modified Analytical Hierarchy Process. This modification is proposed subsequent to the incorporation of concepts related to fuzziness, uncertainty, and vagueness into the analytical framework (Chang, 1996). Using a triangular fuzzy comparison matrix, we describe FAHP to produce a crisp priority vector. Despite the popularity of AHP, it is often criticized for its inability to adequately handle the inherent uncertainty and imprecision that comes from mapping the decision maker's perception to exact numbers (Deng, 1999; Manjare 2015; Manjare et al., 2019).

A method of extent analysis is used to apply the process in accordance with the specified hierarchy. To do this, each criterion within the hierarchy is subjected to extent analysis, called gi. Accordingly, 'M' extent analysis values can be determined for each criterion that can be obtained using following notation.

$$M_{gi}^{1}, M_{gi}^{2}, M_{gi}^{3}, M_{gi}^{4} \ \ldots\ldots\ldots\ldots\ldots\ldots\ldots\ldots M_{gi}^{n}$$

where gi is the goal set (i = 1, 2, 3, 4 … n) and all the M_{gi}^{j}(j = 1, 2, 3, 4…m) are Triangular Fuzzy Numbers (TFNs).The procedural stages for this study can be outlined as follows.

In step 1, in the initial phase, calculate the fuzzy synthetic extent value (Si) concerning the criterion using the following formula:

$$S_i = \sum_{j=1}^{m} M_{gi}^{j} \odot \left[\sum_{i=1}^{n}\sum_{j=1}^{m} M_{gi}^{j}\right]^{-1} \qquad (1)$$

It is an initial step which involves the finding of

$$\sum_{j=1}^{m} M_{gi}^{j} \qquad (2)$$

Analyze "fuzzy addition operation" values up to m degree for a specific matrix as provided in equation (3) below. In the final step of the computing, derive a new set of values (u, v, w), which is then utilized in the subsequent iteration.

$$\sum_{j=1}^{m} M_{gi}^{j} = \left(\sum_{j=1}^{m} u_j, \sum_{j=1}^{m} v_j, \sum_{j=1}^{m} w_j\right) \qquad (3)$$

To obtain the preferred result, calculation process involves determining (u, v, w) variables where "u" is lower limit value, "v" is most hopeful value and "w" upper limit value.

$$\left[\sum_{i=1}^{n}\sum_{j=1}^{m} M_{gi}^{j}\right]^{-1} \qquad (4)$$

"Fuzzy addition operation" calculated to $M_{gi}^{j}(j = 1, 2, 3, 4 \ldots\ldots\ldots m)$ for given value

$$\sum_{i=1}^{n}\sum_{j=1}^{m} M_{gi}^{j} = \left(\sum_{j=1}^{m} u_i, \sum_{j=1}^{m} v_i, \sum_{j=1}^{m} w_i\right) \qquad (5)$$

After deriving result inverse of the vector from equation (5) then following equation is obtained

$$\left[\sum_{i=1}^{n}\sum_{j=1}^{m} M_{gi}^{j}\right]^{-1} = \left[\frac{1}{\sum_{j=1}^{m} w_i}, \quad \frac{1}{\sum_{j=1}^{m} v_i}, \quad \frac{1}{\sum_{j=1}^{m} u_i}\right] \qquad (6)$$

In further step, the degree of possibility of $M_2 = (u_2, v_2, w_2) \geq M_1 (u_1, v_1, w_1)$ is demarcated as equation (7)

$$V\ (M_2 \geq M_1)\ = \sup_{x \geq y} \left[min\left(\mu_{M1}(x), \mu_{M2}(y)\right)\right] \qquad (7)$$

There are two values on the axis of each criteria's membership function x and y. equation (8) gives an equivalent expression for this expression.

$$V(M_2 \geq M_1) = hgt(M_1 \cap M_2) = \mu_{M2}(d) = \begin{cases} 1, if\ v_2 \geq v_1, \\ 0, if\ u_1 \geq w_2 \\ \frac{u_1 - w_2}{(v_2 - w_2) - (v_1 - u_1)}, \ otherwise \end{cases} \qquad (8)$$

In the above equation, d represents the ordinate of the highest point of intersection between μ_{m1} and μ_{m2}. In addition, the extent to which a convex fuzzy number M_i can be larger than

k convex fuzzy numbers Mi for i = 1, 2…..k can be estimated as:

$$V(M \geq M_1, M_2, M_3 \ldots\ldots\ldots M_k)$$
$$= V(M \geq M_1)\ and (M \geq M_2) \ldots\ldots\ldots and (M \geq M_k)$$
$$= \min V(M \geq M_i)\ \ for\ (i = 1,2,3, \ldots\ldots k) \quad (9)$$

Assume that above equation is

$$d'(A_i) = \min V\ (S_i \geq S_k)$$

For k = 1, 2, 3 ……..…n; k≠i. Then the weight vector is given by equation

$$W' = (d'(A_1), d'(A_2), \ldots\ldots d'(A_n))^T \quad (10)$$

where A_i (i = 1, 2, 3…….n) are n elements

After normalization of above equation, a non-fuzzy number (W) is represented as given below:

$$W = \left(d(A_1), d(A_2), d(A_3), d(A_4), d(A_5) \ldots\ d(A_n)\right)^T \quad (11)$$

The Savitri River basin sub-watersheds were assigned priority ratings based on the FAHP analysis method.

RESULTS AND DISCUSSION

An analysis of the morphometric parameters of the watershed under study reveals relevant information about erodibility, which can be used to manage the watershed natural resources effectively. The watershed was characterized morpho-metrically by examining linear, aerial, and relief aspects. Using the terminology scheme presented by Horton (1932), a stream network drainage system was constructed that was described as dendritic in nature and of the 8th order in Savitri River basin.

Table 5. Pair-wise matrix of morphometric parameters on the basis of erosion risk

	Lsm	Rbm	Dd	Fs	Rt	If	Lg	Rc	Rf	Re	Rh	Rn	Wc
Lsm	1, 1, 1	1, 1.5, 2	0.4, 0.5, 0.67	1, 1.5, 2	0.5, 0.67, 1	1, 1.5, 2	2, 2.5, 3	0.33, 0.4, 0.5	1, 1.5, 2	0.33, 0.4, 0.5	1, 1.5, 2	1, 1.5, 2	0.09
Rbm	0.5, 0.67, 1	1, 1, 1	0.5, 0.67, 1	2, 2.5, 3	0.33, 0.4, 0.5	2, 2.5, 3	0.4, 0.5, 0.67	1, 1.5, 2	1, 1, 1	0.33, 0.4, 0.5	0.33, 0.4, 0.5	0.33, 0.4, 0.5	0.08
Dd	1.5, 2, 2.5	1, 1.5, 2	1, 1, 1	1, 1, 1	0.4, 0.5, 0.67	2, 2.5, 3	0.33, 0.4, 0.5	0.5, 0.67, 1	1, 1.5, 2	0.33, 0.4, 0.5	1, 1, 1	0.33, 0.4, 0.5	0.08
Fs	0.5, 0.67, 1	0.33, 0.4, 0.5	1, 1, 1	1, 1, 1	0.33, 0.4, 0.5	0.4, 0.5, 0.67	1.5, 2, 2.5	0.4, 0.5, 0.67	0.4, 0.5, 0.67	1, 1.5, 2	0.4, 0.5, 0.67	1.5, 2, 2.5	0.07
Rt	1, 1.5, 2	2, 2.5, 3	1.5, 2, 2.5	2, 2.5, 3	1, 1, 1	1, 1.5, 2	1.5, 2, 2.5	0.4, 0.5, 0.67	1.5, 2, 2.5	1, 1.5, 2	2, 2.5, 3	0.4, 0.5, 0.67	0.12
If	0.5, 0.67, 1	0.33, 0.4, 0.5	0.33, 0.4, 0.5	1.5, 2, 2.5	0.5, 0.67, 1	1, 1, 1	0.4, 0.5, 0.67	1, 1.5, 2	0.5, 0.67, 1	1, 1.5, 2	0.5, 0.67, 1	1, 1.5, 2	0.07
Lg	0.33, 0.4, 0.5	1.5, 2, 2.5	2, 2.5, 3	0.4, 0.5, 0.67	0.4, 0.5, 0.67	1.5, 2, 2.5	1, 1, 1	0.5, 0.67, 1	1, 1.5, 2	0.5, 0.67, 1	1.5, 2, 2.5	0.5, 0.67, 1	0.09
Rc	2, 2.5, 3	0.5, 0.67, 1	1, 1.5, 2	1.5, 2, 2.5	1.5, 2, 2.5	0.5, 0.67, 1	1, 1.5, 2	1, 1, 1	0.5, 0.67, 1	1.5, 2, 2.5	1.5, 2, 2.5	0.4, 0.5, 0.67	0.11
Rf	0.5, 0.67, 1	1, 1, 1	0.5, 0.67, 1	1.5, 2, 2.5	0.4, 0.5, 0.67	1, 1.5, 2	0.5, 0.67, 1	1, 1.5, 2	1, 1, 1	1, 1.5, 2	0.5, 0.67, 1	1, 1.5, 2	0.08
Re	2, 2.5, 3	2, 2.5, 3	2, 2.5, 3	0.5, 0.67, 1	0.5, 0.67, 1	0.5, 0.67, 1	1, 1.5, 2	0.4, 0.5, 0.67	0.5, 0.67, 1	1, 1, 1	0.5, 0.67, 1	1, 1.5, 2	0.10
Rh	0.5, 0.67, 1	2, 2.5, 3	1, 1, 1	1.5, 2, 2.5	0.33, 0.4, 0.5	1, 1.5, 2	0.4, 0.5, 0.67	0.4, 0.5, 0.67	1, 1.5, 2	1, 1.5, 2	1, 1, 1	1, 1.5, 2	0.09
Rn	0.5, 0.67, 1	2, 2.5, 3	2, 2.5, 3	0.4, 0.5, 0.67	1.5, 2, 2.5	0.5, 0.67, 1	1, 1.5, 2	1.5, 2, 2.5	0.5, 0.67, 1	0.5, 0.67, 1	0.5, 0.67, 1	1, 1, 1	0.10

Table 6. Normalized morphometric parameters matrix of Savitri watersheds

Sub-basin	Lsm	Rbm	Dd	Fs	Rt	If	Lg	Rc	Rf	Re	Rh	Rn
SSB 1	0.786	0.902	0.754	0.419	0.558	0.234	0.744	0.771	0.587	0.767	0.530	0.866
SSB 2	0.726	0.873	0.723	0.420	0.559	0.235	0.769	0.958	1	1	0.935	1
SSB 3	0.575	1	0.634	0.362	0.318	0.115	0.872	1	0.460	0.678	1	0.887
SSB 4	0.459	0.839	1	1	1	1	0.564	0.938	0.397	0.633	0.460	0.814
SSB 5	0.668	0.745	0.673	0.341	0.615	0.210	0.821	0.938	0.873	0.933	0.008	0.692
SSB 6	1	0.906	0.553	0.318	0.380	0.121	1	0.708	0.476	0.689	0.195	0.240

According to linear parameter study, Stream no. (Nu), Mean stream length (Lsm) and Bifurcation ratio (Rb) shows importance for study in risk of erosion. It is observed that SSB 5 has max number of drainages which drain max surface water and erode surface rapidly compare to other followed through SSB 4 and SSB 1, while SSB 3 has less drainages that resulted into less erosion. Many smaller streams had a larger coverage area, leading to a higher likelihood of erosion. SSB 5, SSB 4, SSB 1, and SSB 2 has maximum number of lower order drainages and cover large area. SSB 6 has max overall mean stream length (Lsm) followed through SSB 1 and SSB 2 though SSB 4 has less Lsm. As mean stream length is large, it will influence erosion. Sub-watershad SSB 3, SSB 5 and SSB 1 has higher values of mean bifurcation ratio (Rbm) which indicate greater risk of erosion.

During the morphometric analysis of erosion risk assessment, it was observed that parameters such as drainage density (Dd), stream frequency (Fs), drainage texture (Dt), circularity ratio (Rc), relief ratio (Rr), ruggedness number (Rn), basin relief (Rh), and basin shape (Bs) are positively correlated with erosion risk assessment. An increase in values of these parameters is associated with a greater likelihood of erodibility. It has been found that circularity ratio and basin shape interacts inversely with erodibility, with lower values having a greater influence on it. The values of these properties were therefore inversed in morphometric properties matrix table. According to the erosion risk of each sub-basin, morphometric parameters of each sub-basin were compared with criterion weights (Table 5).

The utilization of triangular fuzzy numbers (TFN) for quantifying the erosion impact of morphometric parameters, helped address uncertainties associated with these parameters. To assign weights to the identified parameters, four triangular fuzzy numbers were employed: very strongly important (VSI-2, 5/2, 3), strongly important (SI-3/2, 2, 5/2), weakly more important (WMI-1, 3/2, 2), and just equal (JE-1, 1, 1). Sub-basins were prioritized by combining normalized weights derived from morphometric parameter values (Table 6) with criterion weights obtained through FAHP (Table 5). These normalized morphometric parameter weights were then multiplied by the FAHP weights to generate non-spatial data for the spatial layer of sub-watersheds. The resulting values, ranging from 0.046 to 0.065, were utilized to assign ranks to sub-watersheds based on their analytical values from highest to lowest (Table 7, Fig. 4a).

In this analysis, sub-watersheds SSB 2 and SSB 4 were designated as the highest priority due to their FAHP values of 0.065 and 0.063, respectively, followed by SSB 1, SSB 3, SSB 5, and SSB 6, which were categorized as the least priority in the watershed (Table 7). The prioritized FAHP scores were divided into three priority classes, ranging from low to high, based on their overall weights (Table 8). Within the Savitri watershed, the low priority classes encompass SSB 6 and SSB 5, covering an area of 1089.17 km^2, while the high priority class includes SSB 2 and SSB 4, covering an area of 572.11 km^2 (Table 8, Fig. 4b). SSB 2, situated in the high priority category near the reservoir, experiences significant erosion and necessitates immediate attention for erosion control and protection. SSB 1 and SSB 3, covering an area of 607.64 km^2, are classified under the medium priority category. Notably, SSB 1, SSB 2, SSB 3, and SSB 4 are situated in high-altitude regions with substantial population density, falling within highly hazardous landslide zones, requiring urgent environmental sustainability measures. Such measures should include,(i) Afforestation and reforestation which will include planting trees to stabilize soil and reduce surface runoff, (ii) Soil surface protection by grasses and other low-lying vegetation, (iii) Establishment of vegetative buffers of plants along the edges of flowing water bodies to filter runoff and stabilize banks, (iv) Construction of terraces on slopes to reduce runoff velocity and increase water infiltration, (v) Plowing along contours of land to create natural barriers against the flow of water, which in turn helps reduce soil erosion, (vi) Construction of small dams and basins which slow down the flow of water that will capture sediments, (vii) Filling and stabilizing gullies using materials like rocks or vegetation so that it doesn't undergo further erosion, and (viii) Construction of bunds, trenches, contour bunding, etc. to regulate the flow of water and thereby reduce erosion.

Table 7. Fuzzy-AHP ranks of the sub-watersheds

Sub-basin	SSB 1	SSB 2	SSB 3	SSB 4	SSB 5	SSB 6
FAHP Score	0.056	0.065	0.055	0.063	0.053	0.046
Rank	3	1	4	2	5	6
Area (Km^2)	457.22	363.17	150.42	208.94	691.07	398.1

Table 8. Prioritization of sub-basin based on erodibility through FAHP score

Sr. No	Fuzzy AHP Score	Priority Class	Sub Watersheds	Area (Km^2)
1	< 0.053	Low	SSB 6, SSB 5	1089.17
2	0.0531-0.056	Medium	SSB 3, SSB 1	607.64
3	> 0.0561	High	SSB 2, SSB 4	572.11

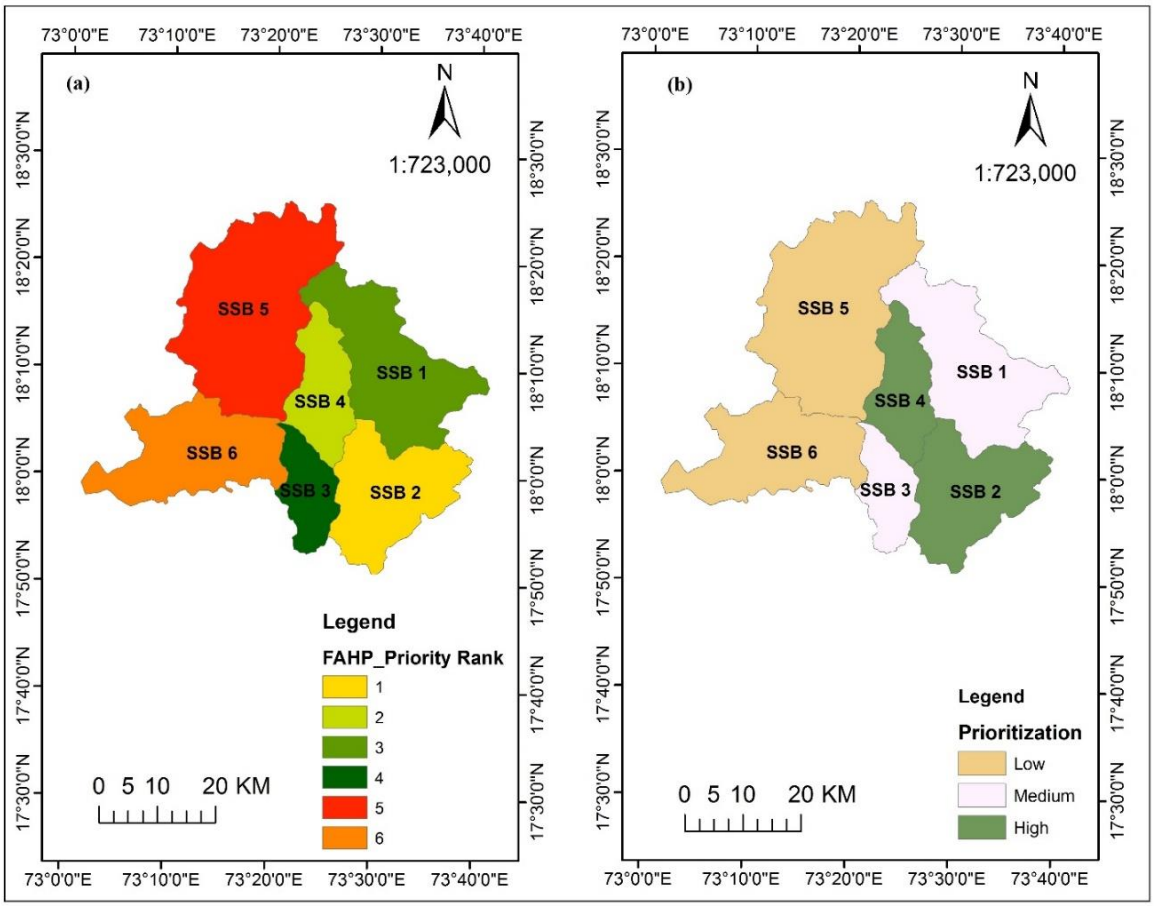

Figure 4. Savitri River basin.**(a)** FAHP rank map, **(b**) Prioritization map.

CONCLUSIONS

This study has ably portrayed the possibility of erosion within the Savitri River basin by undertaking in-depth morphometric analysis, which can aid in prioritizing sub-watersheds for remedial measures. Through this research, FAHP with GIS provided a strong framework for assessing and managing erosion risks, distinctly outlining areas that require immediate attention. Inclusion of triangular fuzzy numbers obviated the uncertainties of parameter weightings and increased the accuracy of erosion risk assessment. The remedial measures, such as afforestation, terracing, contour plowing, check dams, and structures for soil conservation, would therefore be targeted on high-priority areas like SSB 2 and SSB 4. These can stabilize the soil, reduce runoff, and capture sediment, mitigating in large measure the erosion processes. Vegetative cover and gully plugging will further enhance the stability of soils and reduce the risk of landslides in the high-altitude regions. Community participation in erosion control works and education on sustainable land management practices will make the communities self-supporting and therefore create a long-lasting effect of such measures. Improved watershed management will result in increased agricultural productivity, better water quality, reduced risk of natural disasters; hence, better health, well-being, and economic stability of the population concerned. These methodologies and findings therefore have huge potential applications in basin management and hydrological research in the future. In this respect, the integrated approach of FAHP and GIS used can be replicated in other watersheds to give a relative ranking of those areas requiring erosion

control and resource management. Future research may, therefore, be aimed at assessing the impacts of climate change on watershed dynamics and further refining this morphometric analysis with more advanced technologies. On the other hand, this would require continuous monitoring and updating of data so that adjustment in management strategies with changing environment could be included, enabling watershed management to be continued without erosion and other hydrological problems.

ACKNOWLEDGEMENTS

The authors extend their heartfelt thanks to the Rajiv Gandhi Science & Technology Commission (RGST), a Government of Maharashtra initiative, for approving and financially supporting our research, analysis, and assistance efforts. We are grateful to the National Remote Sensing Centre (NRSC) Hyderabad for providing high-resolution data and invaluable guidance. Special thanks go to Mr. Atish Dhende, PAH Solapur University, Solapur, for his tremendous help during fieldwork.

Author credit statement

Y. W. Durugwar: Conceptualization, model runs, formal analysis, validation, manuscript writing and editing. D. D. Kulkarni: Formal analysis, validation, manuscript review and editing. S. S. Pekam: conceptualization, rainfall map preparation, fieldwork, data collection and review.

Data Availability

The monthly rainfall data of Raigad and Ratnagiri district, India are available from

https://www.imdpune.gov.in/cmpg/Griddata/Rainfall_25_NetCDF.html. The toposheet map were sourced from the Survey of India, Department of Science & Technology, Government of India. The digital elevation model data were sourced from the National Remote Sensing Centre (NRSC) Hyderabad, India.

Compliance with Ethical Standards

The author declare that they have no conflict of interest and adhere to copy right norms

REFERENCES

Abrahams, A. D., 1984. Channel Networks: A Geomorphological perspective. Water Res. Res., 20(2), 161–188.

Aher, P., Adinarayana, J. and Gorantiwar, S. D., 2013. Prioritization of watersheds using multi-criteria evaluation through fuzzy analytical hierarchy process. CIGR, 15(1), 11–18.

Biswas, S., Sudhakar, S. and Desai, V. R., 1999. Prioritisation of subwatersheds based on morphometric analysis of drainage basin: a remote sensing and gis approach. J. Indian Soc. Remote Sens., 27(3), 155–166.

Chang, D., 1996. Applications of the extent analysis method on fuzzy AHP. European J. Operational Res., 95(3), 649–655.

Das, A. K. and Mukherjee, S., 2005. Drainage morphometry using satellite data and GIS in Raigad District, Maharashtra. J. Geol. Soc. India, 65(5), 577–586.

Deng, H., 1999. Multicriteria analysis with fuzzy pairwise comparison. In: IEEE international fuzzy systems conference proceedings. August 22–25, 1999, Seoul, Korea. http://dx.doi.org/10.1109/FUZZY.1999.793038

Faniran, A., 1969. The index of drainage intensity : a provisional new drainage factor. Austral. J. Sci., AUS, 31 (9), 328 A 330. http://pascal-francis.inist.fr/vibad/index.php?action=getRecordDetail&idt=GEODEBRGM6918018443

Horton, R. E., 1932. Drainage-basin characteristics. Trans. Am. Geophys. Union, 13(1), 350–361.

Horton, R. E., 1945. Erosional development of streams and their drainage basins; hydrophysical approach to quantitative morphology. Geol. Soc. Am. Bull., 56(3), 275. https://doi.org/10.1130/0016-7606(1945)56

Khan, M., Gupta, V. and Moharana, P., 2001. Watershed prioritization using remote sensing and geographical information system: a case study from Guhiya, India. J. Arid Environments, 49(3), 465–475.

Magesh, N. S., Chandrasekar, N. and Soundranayagam, J. P., 2010. Morphometric evaluation of Papanasam and Manimuthar watersheds, parts of Western Ghats, Tirunelveli district, Tamil Nadu, India: a GIS approach. Environ. Earth Sci., 64(2), 373–381.

Manjare, B. S., 2015. Prioritization of Sub-Watersheds for Sustainable Development and Management of Natural Resources: An Integrated Approach Using Remote Sensing, GIS Techniques. Proc. GIS Creating Our Future, 16th ESRI India User Conference, New Delhi, pp.1-13.

Manjare B.S., Padhye, M. and Girhe, S., 2014. Morphometric Analysis of Lower Wardha River sub Basin of Maharashtra, India Using ASTER DEM Data and GIS, pp. 2-7

Manjare, B. S., Paunikar, S.K. and Shrivatra, J.R., 2019. Prioritization of Sub-Watersheds of Chandrabhaga River from Purna River Basin, Maharashtra, Using Geospatial Techniques. J. Geosci. Res., Special Volume No.2, pp. 111.

Miller, V. C., 1953. Quantitative geomorphic study of drainage basin characteristics in the Clinch Mountain area, Virginia and Tennessee. Department of Geology Columbia University, New York, 389-402. https://agris.fao.org/agris-search/search.do?recordID=US201400058936

Mishra, S. and Siddi Raju, S., 2024. Morphological and hydrological analysis of Kantamal sub-basin of the Mahanadi River Odisha(India), using QSWAT model. J. Indian Geophys. Union, 28(3), 194-206

Ogunkoya, O. and Jeje, L., 1987. Sediment yield from some third order basins on the basement complex rocks in southwestern Nigeria. CATENA, 14(5), 383–396.

Rahaman, S. A., Ajeez, S. A., Aruchamy, S. and Jegankumar, R., 2015. Prioritization of sub watershed based on morphometric characteristics using fuzzy analytical hierarchy process and geographical information system – A Study of Kallar Watershed, Tamil Nadu. Aquatic Procedia, 4, 1322–1330.

Saaty, T. L. 1980. The analytic hierarchy process. New York, U.S.: Mc Graw Hill.

Schumm, S. A., 1956. Evolution of drainage systems and slopes in badlands at Perth Amboy, new jersey. Geol. Soc. Am. Bull., 67(5), 597. https://doi.org/10.1130/0016-7606(1956)67

Shrivatra, J., Manjare, B. and Paunikar, S., 2021. A GIS-based assessment in drainage morphometry of WRJ-1 watershed in hard rock terrain of Narkhed Taluka, Maharashtra, Central India. Remote Sensing Appl. Soc. Environ., 22, 100467. https://doi.org/10.1016/j.rsase.2021.100467

Strahler, A. N., 1952. Hypsometric (area-altitude) analysis of erosional topography. Geol. Soc. Am. Bull., 63, 1117–1142.

Strahler, A. N., 1957. Quantitative analysis of watershed geomorphology. Trans. Am. Geophys. Union, 38(6), 913–920.

Strahler, A. N., 1964. Quantitative geomorphology of drainage basin and channel networks. Handbook of Applied Hydrology, McGraw Hill, New York, 439-476. http://ci.nii.ac.jp/naid/10021229789/

Suresh, M., Sudhakar, S., Tiwari, K. N. and Chowdary, V. M., 2004. Prioritization of watersheds using morphometric parameters and assessment of surface water potential using remote sensing. J. Indian Soc. Remote Sensing, 32(3), 249–259.

Thakkar, A.K. and Dhiman, S.D., 2007. morphometric analysis and prioritization of mini watersheds in mohr watershed. Gujarat using remote sensing and GIS techniques. J. Indian Soc. Remote Sensing, 35, 313-321.

Tiwari, V.M. and Srinivas, N., 2023. Surface and ground water studies in India during 2019-2022. J. Indian Geophys. Union, 27(5), 377-391

Thomas, J., Joseph, S., Thrivikramji, K. P., Abe, G. and Kannan, N., 2012. Morphometrical analysis of two tropical mountain river basins of contrasting environmental settings, the southern Western Ghats, India. Environ. Earth Sci., 66(8), 2353–2366.

Received on: 29-04-2024 ; Revised on: 14-08-2024; Accepted on: 15-08-2024

J. Ind. Geophys. Union, 28(5) (2024), 341-349

Improving CO_2 monitoring accuracy in the Sleipner Area with seismic attribute techniques

G. Hema*, S.P. Maurya, Nitin Verma, Ravi Kant and Ajay P. Singh
Department of Geophysics, Banaras Hindu University, Varanasi, India-221005
Corresponding Author : gopalhema96@gmail.com

ABSTRACT

Monitoring CO_2 in the subsurface is a crucial aspect of long-term storage in any carbon capture and storage (CCS) project. This process involves the continuous measurement and tracking of carbon dioxide (CO_2) concentrations and the evaluation of its behavior within geological formations and storage sites situated beneath the Earth's surface. The key objectives of CO_2 monitoring in the subsurface include ensuring that injected CO_2 is securely contained, detecting any potential leaks or breaches early on to prevent environmental and safety hazards, and understanding how CO_2 interacts with subsurface conditions such as pressure and temperature. In the present study, CO_2 monitoring is performed using seismic attribute analysis of time-lapse seismic data from the Sleipner gas field in the North Sea. 3D seismic data were obtained in 1994 before the injection began, and subsequently in 1999, seismic data were acquired after the CO_2 injection was performed in 1996. The seismic data show a series of bright, sub-horizontal reflections of the CO_2 plume that increase over time, with a noticeable pushdown in velocity underneath. However, it fails to provide detailed CO_2 movement in the subsurface. On the other hand, seismic attribute analysis involves extracting and examining different attributes or characteristics from seismic data generated by sending acoustic waves into the Earth's subsurface and recording their reflections. These attributes include amplitude, frequency, phase, envelope second derivative, etc. Most important attribute is frequency, which can reveal variations in the seismic data's frequency content and facilitate the recognition of lithological changes and reservoir properties. Phase attributes examine phase shifts in seismic data, which are crucial for identifying structural features such as anticlines and synclines. The analysis of seismic attributes provides many advantages in this study, such as monitoring subsurface CO_2 levels, its leakage, and movements. The analysis reveals evidence that seismic attributes can distinguish and monitor the CO_2 plume zone with enhanced resolution better than seismic amplitude alone and can provide very detailed information on CO_2 movement in the subsurface.

Keywords: Carbon capture and storage (CCS), Sleipner gas field, Time-Lapse seismic data, Seismic attributes

INTRODUCTION

Carbon dioxide sequestration is the process of capturing carbon dioxide from the atmosphere and storing it in natural reservoirs to prevent its contribution to global warming (Benson and Cole, 2008). It is crucial to monitor CO_2 levels to ensure the success of this method, preventing leaks and contributing to the long-term effectiveness of climate change mitigation (Riju and Singh, 2021). Statoil and the Sleipner partners launched the initial large-scale project targeting greenhouse gas emissions reduction through carbon dioxide injection at the Sleipner field in the North Sea (Baklid et al., 1996).

The Sleipner field is a significant offshore natural gas field located approximately 250 km off the coast of Norway in the North Sea (Santi, 2019). Equinor, formerly known as Statoil, operates the field in collaboration with its partners. The project focuses on separating carbon dioxide from the natural gas extracted at the Sleipner West reservoir. This isolated carbon dioxide is subsequently injected into the Utsira formation, a deep saline aquifer located beneath the North Sea seabed as part of the overall sequestration (Chadwick et al., 2004; Zweigel et al., 2004). The Sleipner project serves as an important reference point for similar initiatives worldwide and has contributed significantly to the development of carbon capture and storage technology.

Seismic data in three dimensions were acquired in 1994 before the commencement of the injection process. Following this, data were gathered in subsequent years, including 1999, 2001, 2002, and so on. In the present study, we aim to observe the CO_2 plume by conducting seismic attribute analysis on time-lapse seismic data from the Sleipner gas field in the North Sea using 1994 and 1999 seismic data only for simplicity. Seismic attributes refer to specific properties or characteristics derived from seismic data that provide valuable information about the subsurface geology. These attributes are calculated from seismic waves that are sent into the Earth and reflected to the surface (El-Nikhely et al., 2022). Some common seismic attributes include amplitude, which helps identify variations in rock properties such as lithology and fluid content, and frequency, which aids in the identification of geological elements like faults and stratigraphic boundaries. These attributes help in tracking the distribution of the CO_2 plume, identifying any potential migration pathways, and assessing the structural changes induced by the injected CO_2. Attribute analysis plays an important role in the context of CO_2 monitoring. Seismic attribute analysis is crucial for tracking the behaviour and movement of the CO_2 plume within the subsurface reservoir. Originally used for the interpretation of hydrocarbon reservoirs, seismic attribute analysis has developed into a valuable analytical method (Taner et al., 1979; Taner et al., 1994). Seismic attributes play a vital role as a qualitative interpretive tool, assisting in the interpretation of geological structures and stratigraphy, such as channels, pinch-outs, and meanders (Aarre et al., 2012). Hagset (2016) mapped the upper Cenozoic sequences using co-kriging interpolation for

petrophysical data using 3D seismic and well log data on Sleipner area focusing on depositional environments rather than attribute analysis for injected CO_2. While Bitrus et al. (2016) employed seismic attributes for gas chimneys and thin shales, their work centered on reservoir architecture and fluid flow paths, also not directly addressing the injected CO_2 zone and its monitoring. Cho and Jun (2021) examined CO_2 migration in Sleipner using time-lapse seismic and geostatistical methods, similarly Ghosh et al. (2015) modeled CO_2 distribution using PDEM theory with acoustic impedances. However, these studies focused on CO_2 migration and distribution, not utilizing other seismic attributes beyond impedance calculations. This highlights the gap addressed in our work, where the study specifically focusses on monitoring the CO_2-injected zone using various seismic attributes. In the present work, the main purpose of attribute analysis was to validate and evaluate its effectiveness in identifying the CO_2 injection site when compared to the seismic amplitude sections derived from the survey data.

STUDY AREA

The Sleipner Field is situated in the northern region of the North Sea bounded by the countries like Denmark and UK as illustrated in Figure 1. It comprises two distinct producing fields: Sleipner West and Sleipner East. These fields were initially discovered in 1974 and 1981, with Sleipner West commencing gas and gas condensate production in 1996 and Sleipner East in 1993. According to the Norwegian Petroleum Directorate's division map for the Norwegian Continental Shelf, the field is located within blocks 15/9 and 15/6. At the Sleipner gas field in the North Sea, carbon dioxide is extracted from natural gas and subsequently injected into the Utsira storage formation, a porous saline reservoir spanning 26,000 square kilometres (Chadwick et al., 2005). The Utsira formation serves as the reservoir for the carbon sequestration project at Sleipner. Utsira is identified as a highly permeable, porous, and thick saline aquifer, comprising uncontaminated, fine-grained, and easily crumbled sand (Chadwick et al., 2005; Arts et al., 2008). The reservoir is located within the late Cenozoic post-rift sequence of the northern North Sea Basin, forming an extensive basin-constrained deposit during a low stand period. The Utsira formation is bounded by stratigraphic on lap in the eastern and western directions, finer-grained sediment to the southwest, and a narrow, deepening channel to the north (Chadwick et al., 2004; Chadwick, 2013).

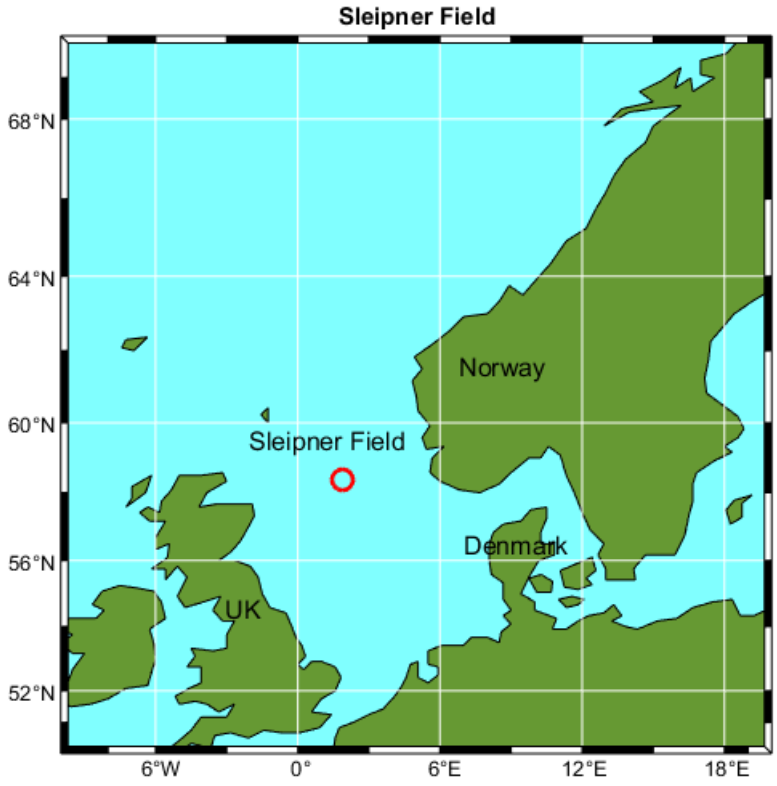

Figure 1. The study area map of the north-sea together with the location of Sleipner Field.

METHODOLOGY

Seismic attributes are essential properties that are directly measured, computed, or deduced from seismic data. These attributes serve as descriptive characteristics that help interpret subsurface geological features and properties (Taner et al., 1979, 1994). They are instrumental in revealing vital information about rock and fluid properties, subsurface structures, and stratigraphic variations, which may not be directly visible from the raw seismic data. By analyzing seismic attributes, one can discern subtle changes in seismic wave behaviour and derive valuable insights into the geological composition, such as lithology, porosity, and fluid content. Consequently, seismic attributes play a pivotal role in enhancing the understanding of subsurface geology and are crucial for making informed decisions during exploration and production activities in the oil and gas industry (Chen and Sidney, 1997; Behrens et al., 1998).

Seismic attributes can be classified into two categories: internal attributes, which are directly derived from the seismic data alone, and external attributes, which are obtained from seismic data by applying mathematical transformations or employing external information. External attributes can be derived from seismic inversion, well logs, geological models, etc. Some common external attributes include acoustic impedance, porosity and permeability. Seismic attributes serve as a crucial tool for interpreting seismic data. In this study, certain seismic attributes have been utilized on sleipner time-lapse datasets. Time-lapse seismic analysis, also known as 4D seismic monitoring, involves repeatedly acquiring seismic data over the same area at different points in time. This technique is widely used in various fields, including oil and gas exploration, reservoir management, and environmental monitoring. Time lapse survey helps to monitor the behavior of CO_2 injected into underground reservoirs over time. By comparing seismic images taken at different intervals, one can track the movement and distribution of CO_2 within the reservoir. This information is crucial for assessing the effectiveness of CO_2 storage and ensuring that the injected CO_2 remains contained within the target geological formations. To determine their efficacy in predicting and monitoring CO_2 behavior considered internal and external attributes are as follows:

(i) Instantaneous frequency

Instantaneous frequency is the time derivative of the phase, i.e., the rate of change of the phase (Cohen and Lee, 1990).

$$F(t) = \frac{d(\phi(t))}{dt} \qquad (1)$$

where $F(t)$ is instantaneous frequency, and $\phi(t)$ represents the phase of the seismic signal at time t. Instantaneous frequency is a seismic attribute that reflects the average frequency of a seismic wavelet at a given time. It is useful for identifying bed thickness and lithology, with high values indicating sharp boundaries or thin shale formations, and low values indicating sand-rich bedding. This distinction can be further enhanced by the presence of unconsolidated oil-bearing sands.

(ii) Instantaneous phase

The instantaneous phase attribute is derived from the formula

$$\phi(t) = \arctan\left|\frac{H(t)}{T(t)}\right| \qquad (2)$$

where H(t) is the Hilbert transform and T(t) is the seismic trace. This attribute helps to measure the phase angle of seismic data at a specific time point. The seismic trace T(t) and its corresponding Hilbert transform H(t) are related to the seismic envelope E(t) and the phase φ(t) through the equations

$$T(t) = E(t)cos\big(\varphi(t)\big) \qquad (3)$$

$$H(t) = E(t)sin\big(\varphi(t)\big) \qquad (4)$$

The instantaneous phase, derived from the Hilbert transform of the seismic trace, represents the instantaneous phase angle of a seismic wavelet at a given time. It is expressed in degrees (-π to π) **(**Chambers and Yarus, 2002**)** and is unaffected by amplitude changes. This attribute effectively displays event smoothness or abruptness, making it suitable for visualizing bedding structures. Ideal phase values along a seismic horizon are constant, but variations can occur due to picking errors or lateral alterations caused by geological phenomena like sinkholes.

(iii) Envelope second derivative

The second derivative of the seismic envelope is a seismic attribute that enhances the visibility of geological interfaces and reflection events in seismic data. It is derived from the second derivative of the seismic envelope, which measures the amplitude variations in the seismic signal over time (Chopra and Marfurt, 2005). The second derivative emphasizes the sharpness of seismic features by quantifying the rate of change of the seismic envelope. Higher values of the second derivative indicate more abrupt amplitude changes, suggesting the presence of distinct geological boundaries or interfaces. This attribute effectively highlights these interfaces within the seismic bandwidth, making them more readily identifiable in the seismic data.

(iv) Seismic inversion

Seismic inversion is a geophysical technique that utilizes seismic data to construct models representing the actual geological structure beneath the Earth's surface. It employs a mathematical approach to transform seismic reflectivity and well data into acoustic, shear impedance, or density parameters (Krebs et al., 2009). Unlike forward modeling, which involves constructing a synthetic seismogram from known geological parameters, inversion seeks to reverse this process, starting with the seismic trace and iteratively improving the model to match the observed seismic data. This process is non-deterministic, meaning there are multiple possible solutions for the acoustic impedance log. The forward modeling starts with a convolution process between the seismic wavelet and reflectivity series with added noise.

$$S(t) = X(t) * R(t) + N(t) \quad (5)$$

where $X(t)$ is the synthetic seismogram, $X(t)$ is the source wavelet, $R(t)$ is the reflection coefficient of the subsurface and $N(t)$ is additive noise (Adedeji, 2016). After that Earth's reflectivity series is calculated which is as follows:

$$R(t) = \frac{M_{i+1} - M_i}{M_{i+1} + M_i} \quad (6)$$

where layer i overlies layer $i+1$ and M_j is the acoustic impedance in the i^{th} layer. Using that impedance can be calculated which is a product of density and velocity.

$$M = V * \rho \quad (7)$$

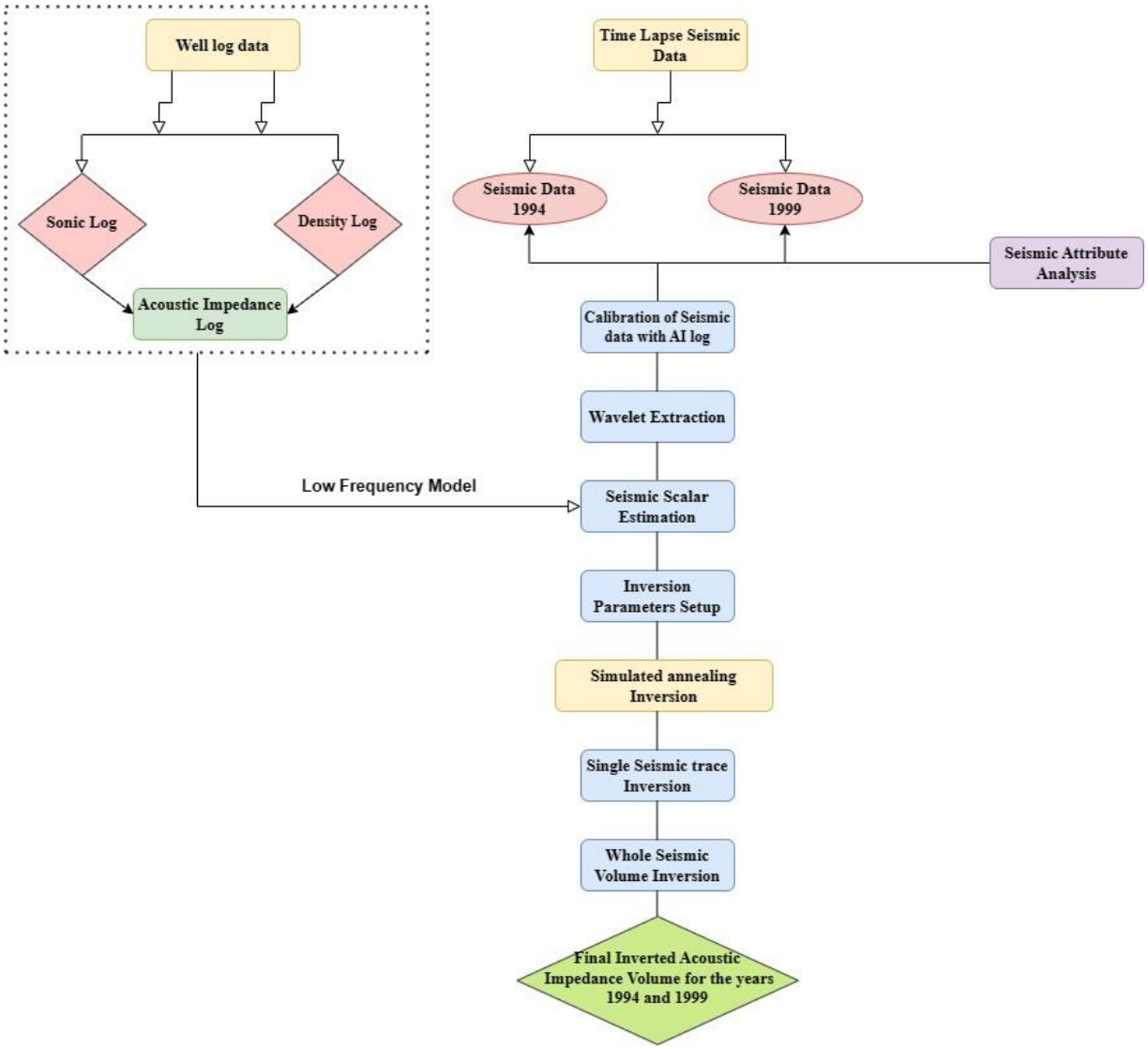

Figure 2. The procedural workflow employed for inverting time-lapse seismic data using the simulated annealing technique.

Seismic inversion is a technique used to estimate reservoir properties from seismic data. However, its limited bandwidth can lead to inaccurate results. Additional constraints, such as geological knowledge, are used to reduce ambiguity and improve accuracy. In this study global optimization based simulated annealing has been used to derive the acoustic impedance of the time-lapse data sets. Simulated annealing, is a method inspired by metallurgical annealing, is an effective method for seismic inversion, which aims to find optimal property combinations that minimize the differences between observed seismic data and model predictions. This technique is particularly useful for complex, nonlinear seismic inversion problems with multiple potential solutions (Goffe et al., 1994). As an iterative optimization algorithm, simulated annealing begins with an initial solution and iteratively refines it, sometimes accepting less favourable solutions to avoid local minima and explore a wider solution space (Metropolis et al., 1953). The algorithm's exploration decreases gradually, similar to the cooling process in metallurgy. Various versions of simulated annealing exist, with the original Metropolis algorithm as the foundation (Corona et al., 1987). By avoiding local minima and finding optimal solutions, simulated annealing effectively reduces discrepancies between models and observations. It uses random walking techniques enhanced with artificial intelligence and introduces a controlling parameter called temperature, which, although unrelated to the inverse problem, guides the optimization process (Hema and Maurya, 2023). Figure 2 displays the flowchart of simulated annealing adopted in this study.

RESULTS AND DISCUSSION

Several CO_2 monitoring techniques, each characterized by specific advantages and limitations, are currently available. However, the primary objective of this research is to examine the effectiveness of CO_2 monitoring through seismic attribute analysis. This methodology is particularly significant as it allows for direct derivation from seismic data. The study utilizes Sleipner datasets from 1994 as the baseline survey and 1999 as the monitor survey (Figure 3). The initial attribute applied to both datasets is the instantaneous frequency (Figure 4). Distinguishable thin lines, highlighted by black arrows, are visible within the frequency range of 20 – 50 Hz in the figures. These observations indicate the presence of sand formations, known as the Utsira Sand which is the chosen layer for CO_2 injection.

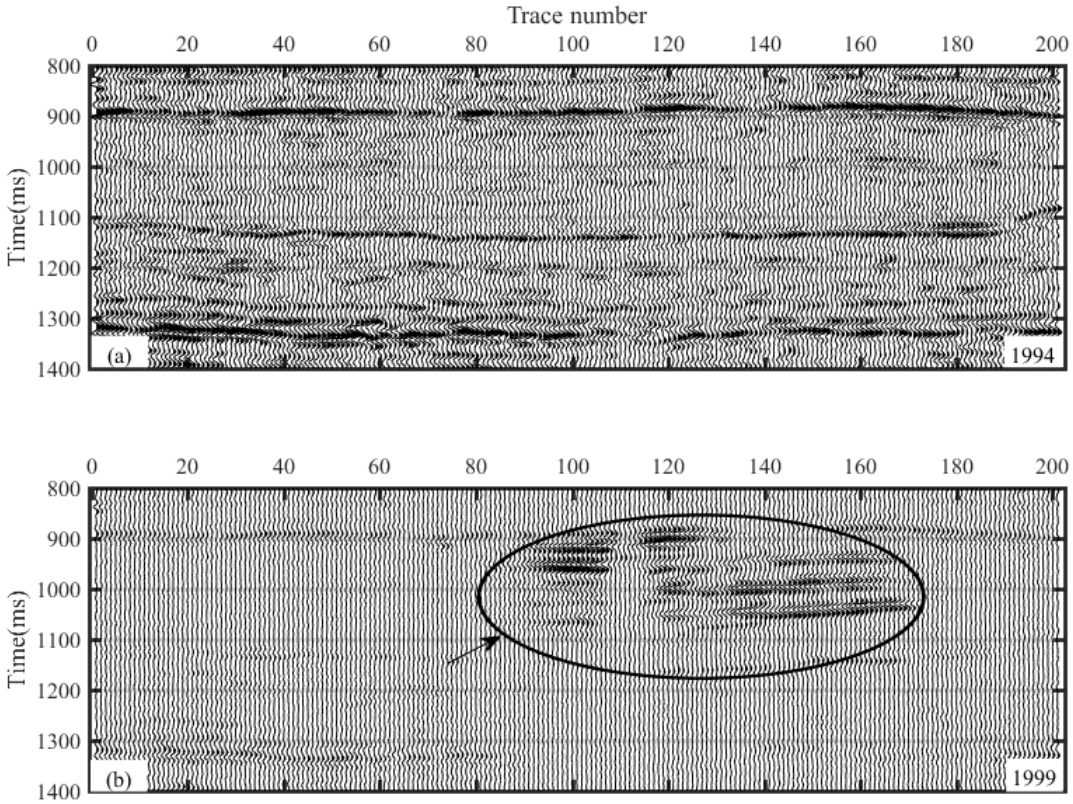

Figure 3. The seismic cross-sections from the post-stack 3D seismic volumes, recorded before and after injection, illustrated for the years **(a)** 1994, and **(b)** 1999, These images highlight a significant high-amplitude anomaly.

The second attribute employed in the study was the instantaneous phase (Figure 5). It enables the visualization of the lateral continuity across both datasets. The purpose of choosing this attribute is to see whether induced CO_2 effect the phase shift of the seismic section, or not. Through the analysis of the instantaneous phase, notable changes in the phase shift were observed, specifically attributable to the introduction of CO_2 in the monitor section. These changes were highlighted and represented in the figures, with the distinct indication of the altered phase shift denoted by the black circle.

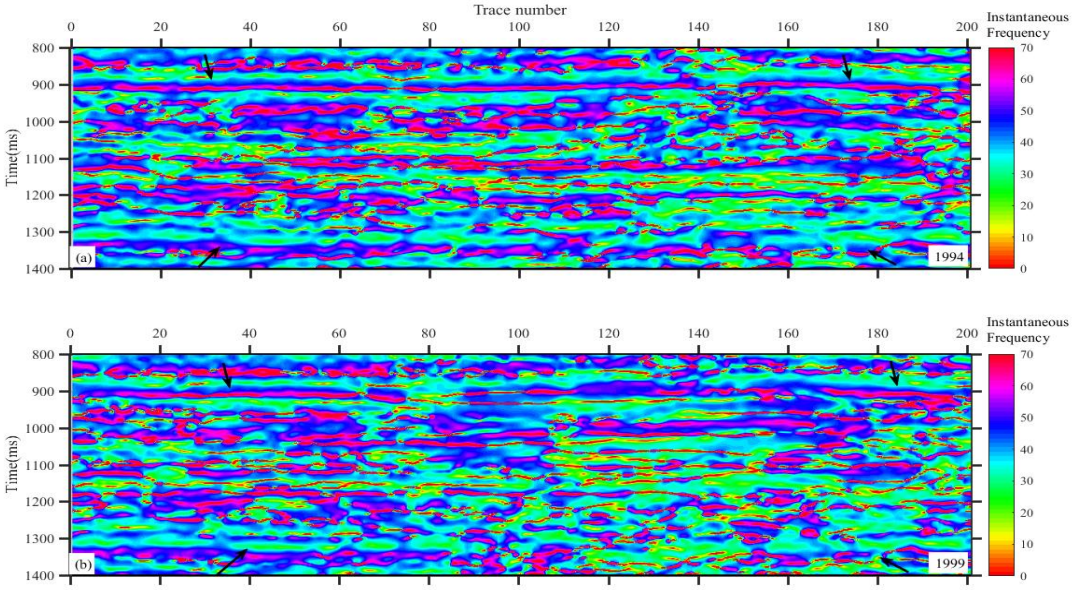

Figure 4. The instantaneous frequency cross-sections of seismic data for the years **(a)** 1994, and **(b)** 1999, displaying notable characteristics. Within the specified frequency range, thin lines highlighted by black arrows are identified, indicating the presence of sand formations.

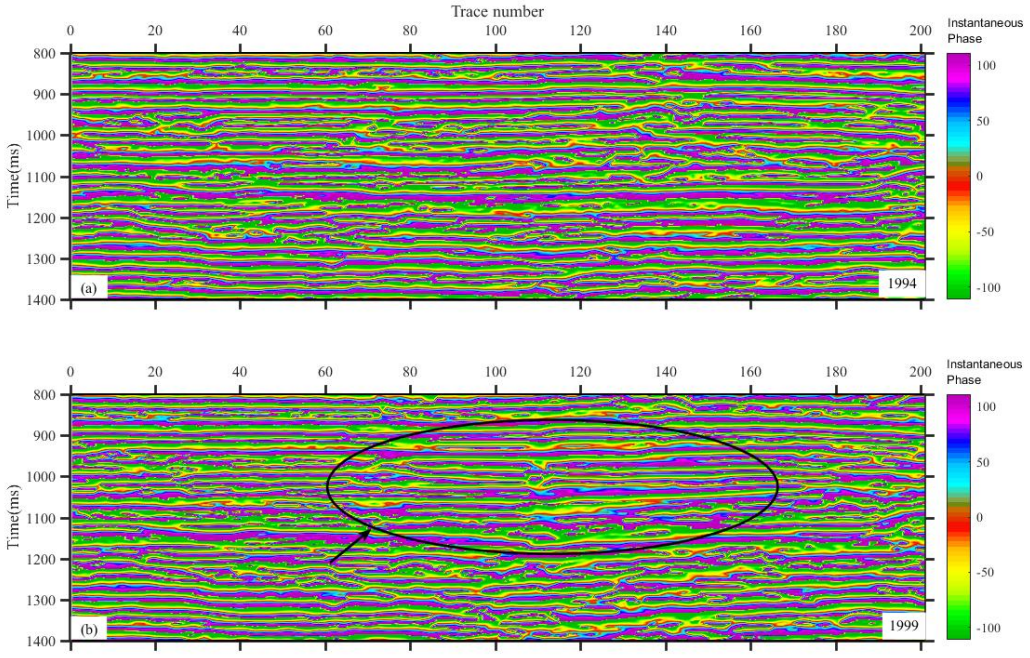

Figure 5. The instantaneous phase cross-sections of seismic data for the years **(a)** 1994, and **(b)** 1999. A notable phase shift denoted by black circle is evident in the post injection year.

The next attribute used in the study is the envelope second derivative, which serves as an indicator of the sharpness of the envelope peak and is notably useful as a primary attribute representation. Figure 6 demonstrates the application of this attribute in both sections. This application highlights abrupt changes or irregularities in rock properties, greatly enhancing the accuracy of reservoir characterization. This feature distinctly emphasizes the CO_2 plume area, making its boundaries clearer, as demonstrated in the figure. As a result, this method enables a more thorough analysis of CO_2 migration patterns and storage behaviors in the examined region. This characteristic effectively emphasizes the CO_2 plume region and enhances the clarity of the zone, highlighted by the black circle. Figure 7 shows the inverted impedance for the years 1994 and 1999, respectively.

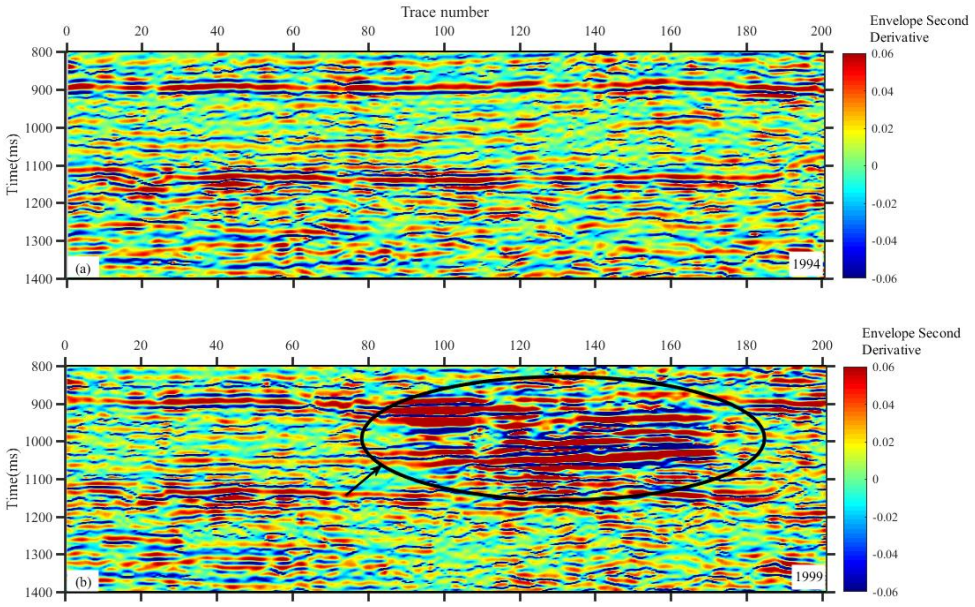

Figure 6. The cross-sections show envelope's second derivative for seismic data from the years **(a)** 1994 and **(b)** 1999. A sharpened delineation, highlighted by the black circle with arrow in Figures 5b, is particularly notable. This technique effectively enhances the clarity and sharpness of the CO2 plume zone.

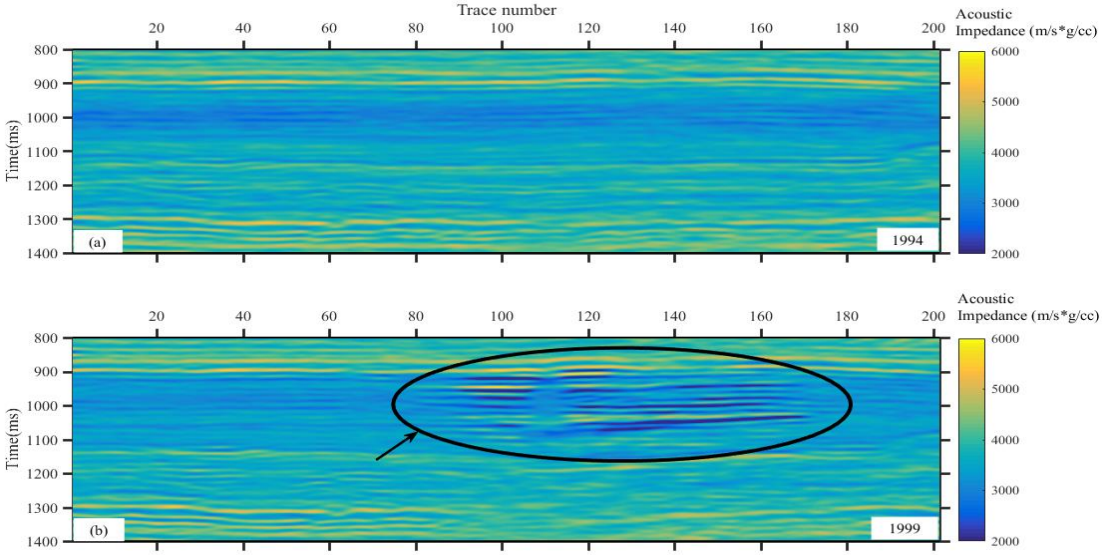

Figure 7. Inverted impedance for the years **(a)** 1994 and **(b)** 1999, focusing on the 0.85 to 1.10-second interval that corresponds to the Utsira formation. The identification of thin, low-impedance layers within these sections, prominently highlighted by the black circle in the figures, strongly suggests the presence of CO2.

The figure 7 focus on the 800 ms to 1400 ms interval, which corresponds to the Utsira formation. In both years, thin layers of low impedance are identified within this period, indicative of the presence of CO_2.The impedance within this zone is determined to be in the range of 2000 to 2400 m/s*g/cc. Notably, these low-impedance layers are found to be stacked with the high-impedance layers, highlighted by a black circle. These findings underscore the attribute's effectiveness in accentuating subtle variations in the underground area, contributing to a more comprehensive examination of CO_2 migration and storage dynamics in the studied region.

CONCLUSIONS

This study utilizes seismic attribute analysis of time-lapse seismic data from the Sleipner field in the North Sea to monitor CO2 injection. Three-dimensional seismic data were acquired in 1994, before injection began, and again in 1999, after injection commenced in 1996. Attributes that are used in this study are mainly, the instantaneous frequency, phase, and envelope second derivative. The instantaneous frequency effectively highlights variations in the frequency content of seismic waves, aiding in the detection of lithological changes and the delineation of stratigraphic boundaries such as thin beds. The instantaneous phase offers detailed insights into the signal's phase changes over time, helping identify subtle geological features like bed boundaries and faults. The envelope second derivative highlights the sharpness of seismic features by measuring how quickly the seismic envelope changes. Higher second derivative values indicate sharper amplitude changes, suggesting the presence of distinct geological boundaries or interfaces. This attribute enhances the detection of higher amplitude values, which typically indicate the presence of gas. Similarly, analysing acoustic impedance provides detailed insights into the composition and properties of rock formations. Acoustic impedance plays a crucial role in CO_2 sequestration project, as it reveals information about subsurface rock properties that influence seismic wave behaviour. Regarding CO_2 storage dynamics and monitoring, acoustic impedance analysis helps identify low impedance zones, distinguishing them from the surrounding high impedance zones and aiding in the monitoring of CO_2 migration. These attributes have effectively revealed the presence of sand formations, thinly bedded shale interlayers, and the CO_2 plume zone, enabling a detailed characterization of subsurface features and associated lithological variations. The comprehensive seismic attribute analysis has not only facilitated the monitoring of the CO_2 plume but has also enhanced the resolution and clarity of subsurface images, thereby contributing to a more precise and detailed understanding of CO_2 storage processes. The study concluded that seismic attributes have been effective in CO_2 monitoring, showing no observed CO_2 leakage and providing clearer, high-resolution images. This constitutes a valuable contribution to ensure safe and effective CO_2 storage offering a robust framework for monitoring CO_2 migration and the associated changes in reservoir properties.

ACKNOWLEDGEMENTS

The authors would like to express their gratitude to CGG Geo Software for generously providing the Hampson Russell software and data, which were instrumental in the success of this research. Additionally, one of the authors, S.P. Maurya extends heartfelt thanks to the funding agencies UGC-BSR (M-14-0585) and IoE BHU (Development Scheme no. 6031B) for their vital financial support, which enabled this study. Special acknowledgment is also given to www.mathworks.com for providing academic licenses for Matlab (2022b). These valuable resources were crucial to the successful completion of this research.

Author Credit Statement

G. Hema was involved in methodology, conceptualization, investigation and original draft writing. S.P. Maurya supervised throughout the research. Nitin Verma, Ravi Kant undertook thorough review and editing. and Ajay P. Singh conducted validation.

Data Availability

This study utilizes post-stack seismic data in conjunction with well-log data from the Sleipner field in Norway. The data was obtained from https://co2datashare.org.

Compliance with Ethical Standards

The authors declare that they have no conflict of interests and hence they adhere to copy write norms.

REFERENCES

Aarre, V., Astratti, D., Al Dayyni, T.N.A., Mahmoud, S.L., Clark, A.B., Stellas, M.J., Stringer, J.W., Toelle, B., Vejbæk, O.V. and White, G., 2012. Seismic detection of subtle faults and fractures. Oilfield review, 24(2), 28-43.

Adedeji, E. A., 2016. 3D Post-stack Seismic Inversion using Global Optimization Techniques: Gulf of Mexico Example. University of New Orleans Theses and Dissertations. https://scholarworks.uno.edu/td/2231

Arts, R. J., Chadwick, A., Eiken, O., Thibeau, S. and Nooner, S., 2008. Ten years' experience of monitoring CO2 injection in the Utsira Sand at Sleipner, offshore Norway. First break, 26(1), 65-72

Baklid, A., Korbol, R. and Owren, G., 1996. Sleipner Vest CO2 disposal, CO2 injection into a shallow underground aquifer. In SPE Annual Technical Conference and Exhibition.

Behrens, R. A., MacLeod, M. K., Tran, T. T. and Alimi, A. O., 1998. Incorporating seismic attribute maps in 3D reservoir models. SPE Reservoir Evaluation Engineering, 1(02), 122-126.

Benson, S.M. and Cole, D.R., 2008. CO2 sequestration in deep sedimentary formations. Elements, 4(5), 325-331.

Bitrus, P.R., Iacopini, D. and Bond, C.E., 2016. Defining the 3D geometry of thin shale units in the Sleipner reservoir using seismic attributes. Marine and Petrol. Geol., 78, 405-425.

Chadwick, R. A., 2013. Offshore CO2 storage: Sleipner natural gas field beneath the North Sea. In Geol. Stor. Carb. Diox. (CO2),227-253. Woodhead Publishing.

Chadwick, R. A., Zweigel, P., Gregersen, U., Kirby, G. A., Holloway, S. and Johannessen, P. N., 2004. Geological reservoir characterization of a CO2 storage site: The Utsira Sand, Sleipner, northern North Sea. Energy, 29(9-10), 1371-1381.

Chadwick, R.A., Arts, R. and Eiken, O., 2005. 4D seismic quantification of a growing CO2 plume at Sleipner, North Sea. In: Geological Society, London, Petroleum Geology Conference series ,6(1), 1385-1399.

Chambers RL and Yarus JM., 2002. Quantitative use of seismic attributes for reservoir characterization. CSEG Recorder, 27(6), 14–25.

Chen, Q. and Sidney, S., 1997. Seismic attribute technology for reservoir forecasting and monitoring. The Leading Edge, 16(5), 445-448.

Cho, Y. and Jun, H., 2021. Estimation and uncertainty analysis of the CO2 storage volume in the Sleipner field via 4D reversible-jump Markov-chain Monte Carlo. J. Petrol. Sci. and Engineering, 200, 108333.

Chopra, S. and Marfurt, K.J., 2005. Seismic attributes—a historical perspective. Geophysics, 70(5). https://doi.org/10.1190/1.2098670

Cohen, L. and Lee, C., 1990. Instantaneous bandwidth for signals and spectrograms. In: International conference on acoustics, speech, and signal processing, 2451–2454.

Corana, A., Marchesi, M., Martini, C., Ridella, S. 1987. Minimizing multimodal functions of continuous variables with the "simulated annealing" algorithm—Corrigenda for this article is available here. ACM Transactions on Mathematical Software (TOMS), 13(3), 262-280.

El-Nikhely, A., El-Gendy, N.H., Bakr, A.M., Zawra, M.S., Ondrak, R. and Barakat, M.K., 2022. Decoding of seismic data for complex stratigraphic traps revealing by seismic attributes analogy in Yidma/Alamein concession area Western Desert, Egypt. J. Petrol. Expl. and Production Technology, 12(12), 3325-3338.

Ghosh, R., Sen, M.K. and Vedanti, N., 2015. Quantitative interpretation of CO2 plume from Sleipner (North Sea), using post-stack inversion and rock physics modeling. Int. J. Greenhouse Gas Control, 32,147-158.

Goffe, W.L., Ferrier, G.D. and Rogers, J., 1994. Global optimization of statistical functions with simulated annealing. J. Econometrics, 60(1-2), 65-99.

Hagset, A.H., 2016. Seismic attributes, well correlation and geostatistical analysis for sequence variability prediction in the Sleipner area
https://api.semanticscholar.org/CorpusID:133563230

Hema, G. and Maurya, S.P., 2023. Monitoring of CO_2 Sequestration through Seismic Inversion Using Simulated Annealing: Insight from Synthetic Data Analysis. In: 2nd EAGE/Aqua Foundation Indian Near Surface Geophysics Conference & Exhibition, 23(1),1-5. European Association of Geoscientists & Engineers.

Krebs, J.R., Anderson, J.E., Hinkley, D., Neelamani, R. et al., 2009. Fast full-wave-field seismic inversion using encoded sources. Geophysics 74(6), 177–188.

Metropolis, N., Rosenbluth, A.W., Rosenbluth, M., Teller, A. and Teller, E., 1953. Simulated annealing. J. Chem. Phys., 21(161-162), 1087-92.

Riju, Linda, A. and Singh, H.P., 2021. Geological carbon capture and storage as a climate-change mitigation technology. Advances in Carbon Capture and Utilization, 33-55. DOI: 10.1007/978-981-16-0638-0_3

Santi, A.C., 2019. Factors impacting multi-layer plume distribution in CO2 storage reservoirs. pp.73

Taner, M. T., Koehler, F. and Sheriff, R. E., 1979. Complex seismic trace analysis. Geophysics, 44(6), 1041-1063.

Taner, M. T., Schuelke, J. S., O'Doherty, R. and Baysal, E., 1994. Seismic attributes revisited. In: SEG technical program expanded abstracts, 1104-1106.

Zweigel, P., Arts, R., Lothe, A.E. and Lindeberg, E.B., 2004. Reservoir geology of the Utsira Formation at the first industrial-scale underground CO2 storage site (Sleipner area, North Sea). Geological Society, London, Special Publications, 233(1), 165-180

Received on: 13-02-2024 ; Revised on: 25-06-2024; Accepted on: 05-07-2024

J. Ind. Geophys. Union, 28(5) (2024), 350-370

Insight into structural fabric and crustal architecture across Eastern Dharwar Craton, Southern India from combined analysis of gravity and magnetic Data

D.C. Naskar[1*], Pradip Kumar Yadav[2], Jayati Ray[2], Deepak Maurya[3]
[1]National Centre for Seismology (NCS), Ministry of Earth Sciences (MoES), Government of India, New Delhi-110003, India
(Formerly, Geological Survey of India, Sothern region, Hyderabad-500068, India)
[2]Geological Survey of India (GSI), Eastern Region, Kolkata- 700091, India
[3]Geological Survey of India (GSI), Northern Region, Lucknow- 226024, India
*Corresponding author: drdcnaskar@gmail.com

ABSTRACT

Gravity and magnetic surveys have been carried out to delineate the structural fabric and crustal architecture of the southern part of eastern Dharwar craton. Bouguer gravity anomaly map shows high gravity responses over Peninsular Gneissic Complex (PGC II) (relative to the adjacently located Cuddapah Supergroup) due to the occurrence of dominant rock types, like hornblende-biotite-granite-gneiss, hornblende-biotite-granite, hybrid granite-gneiss, migmatite-gneiss, which have higher densities than the Proterozoic sediments of the Cuddapah Supergroup. High gravity enclaves formed by the closed contours with values increasing towards centre within these zones, represents fault-bound antiformal structure signifying shallowing of the mantle. The low residual gravity anomalies are mostly represented by elongated structure interpreted as minor shears where mineralization has occurred. The prominent magnetic low zone, including some pockets of moderate to high magnetic anomalies, indicates deposition of rocks of high magnetite content rather than the disposition of mafic/ultramafic rocks. The density interface at the depth ~7 km as obtained from the spectral study, may indicate an average depth to the interface between amphibole-granulite facies rocks and the underlying high density granulitic crust. Similarly, the second density interface at ~3.6 km may be indicating an average depth to the bottom of the granitic-gneissic layer that rest over the amphibolite- granulite facies crust. Amplitudes of gravity and magnetic anomalies over the area are lower than those normally associated with ore bodies, and hence, not encouraging for major mineral prospecting. However, possibility of occurrences of a few isolated mineralised pockets, as apparent from discrete gravity and magnetic highs in some limited areas, especially in Elupuru-Nellatur (Toposheet 57O/14) and Ponnai-Melpadi (Toposheet 57O/8) sections, cannot be ruled out.

Keywords: Gravity, Magnetic, Mineral deposits, Exploration, Geological structures, Density, Susceptibility, Eastern Dharwar craton.

INTRODUCTION

Nowadays, classical prospecting geophysical methods refer to techniques that are used to explore and investigate subsurface features and resources. They pose problems for their effectiveness in mineral exploration in regions of poor outcrops or those subjected to intense and long mining activities (Gandhi and Sarkar, 2016). In this perspective, the geophysical methods are efficiently and increasingly used to prospect undercover deposits or inaccessible regions like forest and mountains (Moon et al., 2006). Geophysical methods are generally coupled with the geochemical and remote sensing approaches during mineral exploration program, in order to image the subsurface thus making them critical tools for the prospection of concealed deposits. For their higher sensibility to slight physical contrast, geophysical methods are capable to provide important geological information that might have been overlooked by the exploration geologist (Dentith and Mudge, 2014).

Generally, the direct and indirect surveys are the two different methods applied in mineral exploration depending on whether the surveys are conducted in smaller or larger scales. They are conducted in smaller scales if the targeted source is restricted to rocks that have direct correlation to mineralization called "anomaly". The defined anomalous regions are further and thoroughly examined in terms of their nature, size, shape and position to restrict the target to the more likely potential mineralized area for the incoming drilling stage. However, geophysical surveys carried out in larger scales correlate crustal deformation or deep-seated structures (faults, folds, lineaments) with mineralization (Marjoribanks, 2010). Relative to the effectiveness of the application of geophysical methods to a large spectrum of the deposit types, the magnetic and the gravity methods are more often used. The gravity method in particular, serve as a prime exploration tool to the search of numerous deposit types, especially precious and base metal deposits and it has played a key role on the discovery of the well-known deposits, namely Neves Corvo massive sulphide deposit in Portugal, the high-grade Hishikari epithermal gold deposit in Japan, the Olympic Dam and the Prominent Hill Iron Oxide-Copper-Gold (IOCG) deposits in Australia (Marjoribanks, 2010).

The recent geophysical studies involving seismic, gravity, magnetic, and magnetotelluric (MT), suggest that the Late Archean collision and Late Proterozoic extensional tectonics, played a significant role in the evolution of the tectonic zones over the Southern Granulite Terrain (SGT) (Rao et al., 2006) inferred by gravity high zones. The occurrence of mid-crustal high-density rock and thinning of crust are attributed for the gravity high; however, gravity models across the shear zone were revised and updated (Singh et al., 2003; Mishra et al., 2006; Singh et al., 2006). The seismic velocity model put forwarded by Rao and Prasad (2006) shows a four-layer

velocity sequence and almost flat Moho beneath SGT. The MT studies (Harinarayana et al., 2003, 2006; Naganjaneyulu and Santosh, 2010) revealed a conductive feature and it was interpreted as fragments of subducted oceanic crust. The previous geophysical studies mainly brought out the deeper crustal structure and its possible tectonic implications. However, studies revealing the shallow (~6-8 km) crustal architecture and their tectonic implications regarding evolution of the tectonic zones are scarce. The geophysical signature of a paleo-oceanic crust not yet reported.

The present study with denser and most updated data coverage of gravity and magnetic observations, brings out both shallow and deeper crustal fabrics, which may have a significant impact on the understanding of evolution of the tectonic zones. The goal of this manuscript is to delineate the subsurface structures which control mineralization both in shallow and deeper level. A total number of 1337 gravity and magnetic (TF) observations were recorded with an average station density of 2.5 sq km/station in parts of the Andhra Pradesh and Tamil Nadu (Toposheets: 57O/8, 57O/11, 57O/14, 57J/15 and 57J/16; Long: 78°45'-80°E, Lat: 13°-14°30'N) (Figure 1). In the present study, results are being presented for the areas covering three toposheets between Lat. 13°-13°45' N and Long. 79°15'-80°E, which lies south of the Cuddapah basin.

GEOLOGICAL SETTING

The Dharwar craton exposing one of the largest and deeply eroded Precambrian continental crust, is an assemblage of several crustal blocks ranging in age from Archean to Proterozoic (Ramakrishna and Vaidyanadhan, 2008) The area is mainly represented by rock types belonging to Archean and Proterozoic groups (Figure 2) (GSI, 1993, 1998).

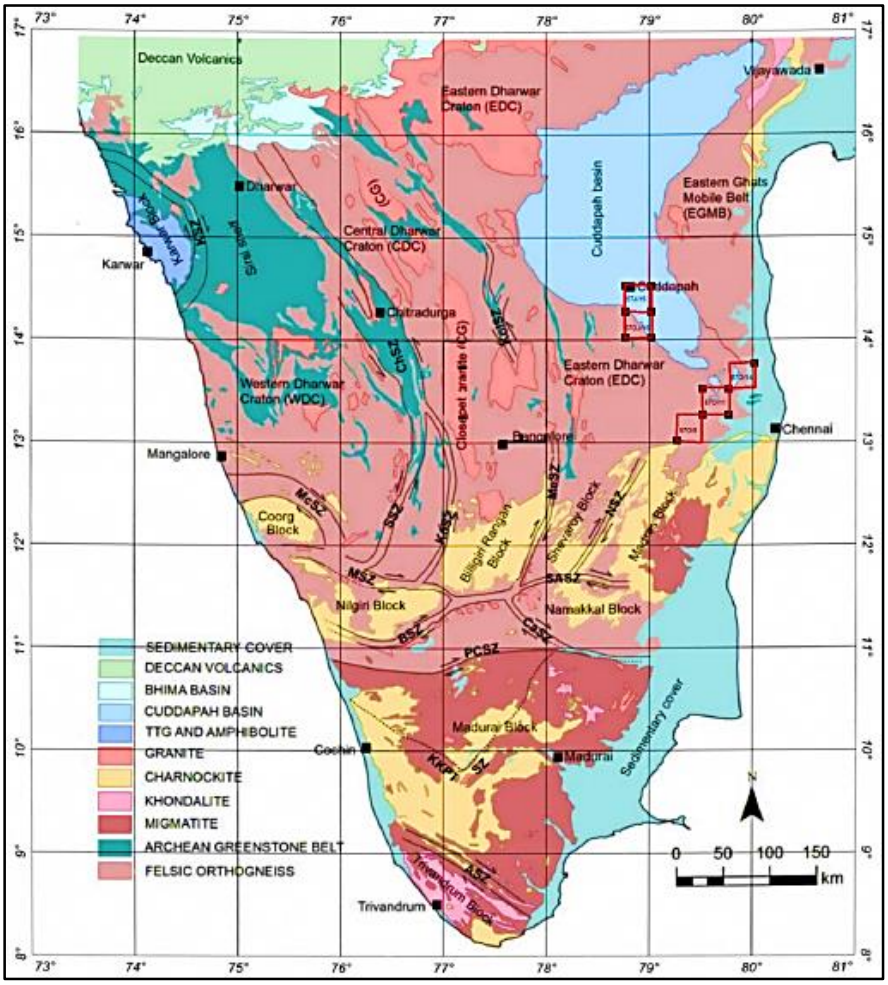

Figure 1. Generalized geological framework of the Dharwar craton, Southern Indian shield, Present study area is covered by three adjacent Toposheets (57O/8, 57O/11 and 57O/14) pertaining to areas located south of the Cuddapah basin and in the close vicinity of SGT (GSI, 2019).

The oldest lithounit represented by the amphibolites of the Satyamangalam Group of rocks of Archean age, quartz-chlorite-sericite-schist and chlorite-sericite-schist (Tsundu - palli schist belt) of Dharwar Supergroup of rocks of Archean age, the PGC (PGC-II Group) Supergroup consisting mainly of grey hornblende-biotite-granite-gneiss, grey hornblende-biotite-granite, hybrid granite-gneiss, migmatite-gneiss of Archean-Paleoproterozoic age

METHODOLOGY

Processing of gravity and magnetic data

The gravity data were acquired by Scintrex made CG-5 gravimeter (resolution 0.001 mGal) and magnetic data by total field proton precession magnetometer (accuracy ± 0.5 nT) (GSM-19T, GEM make, Canada). Differential Global Positioning System (DGPS) (Leica Geosystems AG, Switzerland; model: Viva) levelling instruments were used for measuring station elevation with respect to mean sea level, which is aided with GPS antenna (AS10), GPS receiver (GS10) and control unit (CS10). Data were processed with Leica Geo Office 10.3 software for determination of station coordinates and elevation. The drift correction was applied to the acquired data on a routine basis and then the entire data were tied to the IGSN-1971 gravity base established by Geological Survey of India. The standard gravity corrections, that is the free air (0.3048 mGal/m) and Bouguer plate corrections were applied to reduce the data to a single standard datum at mean sea level. Bouguer anomaly over the study area was computed for the standard crustal density of 2.67 gm/cc. For latitude correction international gravity formula 1980 was used.

Repeated magnetic observations were taken at each station to ensure noise-free data. The magnetic data were corrected for diurnal effect on a daily basis followed by diurnal and IGRF (2010, epoch) corrections. The gravity and magnetic data were gridded using minimum curvature technique with 1000 m grid spacing

Measurement of petrophysical properties of the rock samples

The gravity and magnetic anomaly map with present station density usually reflect averaged response from the geological bodies as compared to lithological variation from the outcrop scale (Garcia-Lobon et al., 2014). An extensive campaign was made to collect rock samples of the representative lithounits during gravity-magnetic data acquisition as the petrophysical properties provide fundamental constraints for interpretation of potential field data. Two properties, density and magnetic susceptibility were measured, along with their petrological identifications for each collected rock samples. Density is the petrophysical property which influences gravity data, and magnetic susceptibility is one of the key parameters that characterizes magnetic anomaly. A total of 100 unweathered samples were collected. The reliable estimate of petrophysical signature of density and susceptibility of the collected rock samples were made using Electronic Balance, FX-400, AFCOSET, India, and MS-2 Magnetic susceptibility meter, Bartington, UK respectively.

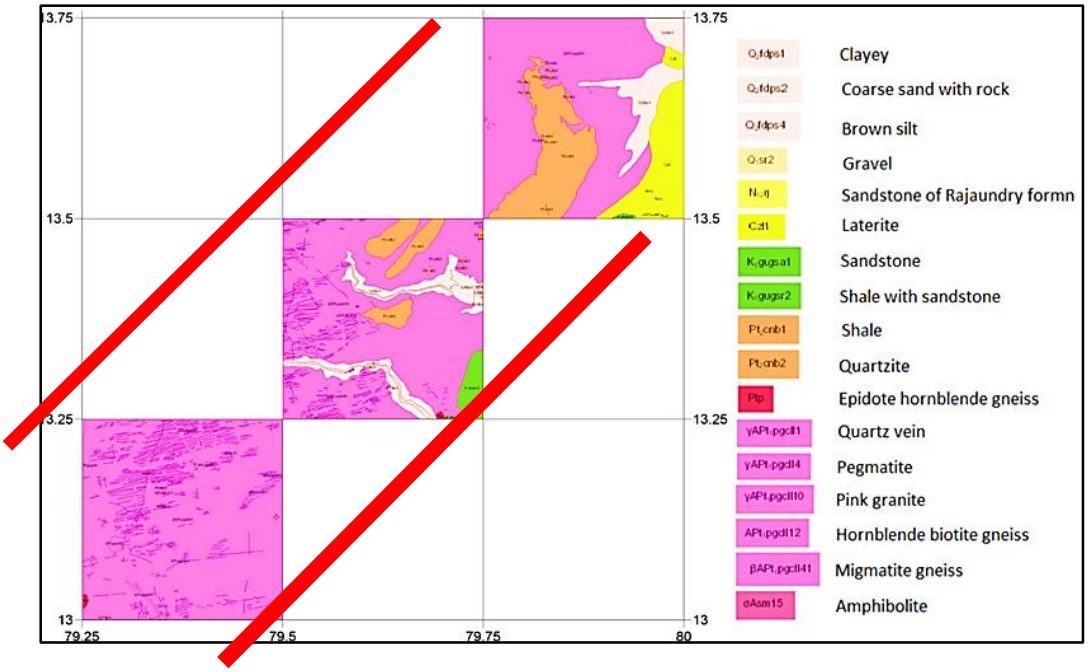

Figure 2. Geology map of the study area covered by Toposheets 57O/8, 57O/11 and 57O/14 (GSI, 1993).

The lithounits of the Archean age represented by biotite-gneiss, amphibolites, and banded magnetite quartzites (BMQ), exhibit higher density values in the order of 2.95 gm/cc. The rocks also reveal higher magnetic susceptibility values which indicate the mafic character of the rocks. However, the measured susceptibility values for each rock samples show wide scatter; hence average susceptibility values were not determined. The silicic units such as granites show moderate density (2.65-2.67 gm/cc) and diamagnetic to paramagnetic character. Similarly, anorthosite and vein quartz samples show lower density and lower susceptibility values. The granite gneiss is the most abundant rock type of the area that shows average density values of 2.70 gm/cc, but magnetic property varied widely (Table 1).

The petrographical analysis of several samples of mafic granulite was carried out by Saitoh et al. (2011) which indicate broadly identical mineral assemblage. The representative samples of mafic granulite show an assemblage of garnet (40-50%), pyroxene (20-30%), calcic amphibole (5-15%), and plagioclase (5%). Similarly, representative samples of amphibolite reveal broad assemblage of amphibole (40-50%) and plagioclase (20-30%). The high density and susceptibility of pyroxene granulites and amphibolites may indicate presence of pyroxene or amphibole-rich lithounits respectively. Yellappa and Rao (2018) have provided an average model composition of granitic plutons (Table 2). The paramagnetic and diamagnetic nature of the granites of the study may be due the abundance of quartz and K-feldspar.

RESULTS AND DISCUSSION

Bouguer gravity anomaly

For many years, gravity methods have been used to study geological structures, which vary in depth and size from very deep crustal blocks to near-surface ore bodies. In general, large regional variations in the Bouguer gravity field is related to changes in the thickness of the earth's crust or are due to large scale mass inhomogeneities, while local anomalous gravity values are attributed to near-surface inhomogeneities. Negative anomalies are identified with the sedimentary basins, salt, granitic bodies, and graben faults. Similarly, positive gravity anomalies are identified with uplifts, horsts, and underlying mafic rock masses. The gravity method could be applied on various problems related to regional and local subsurface structures. At the same time, despite the problem of ambiguity in interpretation, gravity anomalies can give highly meaningful information about the subsurface structures and density distributions (Sharma, 1986).

Table 1. Measured physical properties of the rock samples (GSI, 2019).

Lithounit	Average density (gm/cc)	Average susceptibility $\times 10^{-6}$ (cgs unit)
Dolerite	2.90	524
Granite	2.67	131
Granite-gneiss	2.73	135
Quartzite	2.60	0.82
Quartz vein	2.63	0.24
Pegmatite	2.63	2.55
Ferruginous sandstone	2.97	10.4
Ferruginous quartzite	2.56	2.9
Banded magnetite quartzite	2.95	1000
Biotite-gneiss	2.70	120
Shale	2.42	3.7

Table 2. Average model composition of granitic plutons (Modified after Yellappa and Rao, 2018). Total number of samples: 29.

Mineral	Volume (%)
Quartz	15.4-27.7
Plagioclase	7.7-22.7
K-feldspar	55.5-66.4
Biotite	1.1-5.8
Amphibolite	0-0.8

The Bouguer gravity anomalies obtained after various corrections to the observed field, represent the combined responses of various masses lying at depths below the ground surface. At this stage, the interpreter separates the effects which are likely to be associated with the geological features of interest or the target body from the rest of the response. In case of problems dealing with mineral and hydrocarbon exploration or the delineation of structures for engineering and foundation purposes, the interpreter is concerned with depths ranging from a few tens of metres to a few kilometres. There are also problems dealing with deep-seated structures at crustal or even Moho depths. Therefore, the zones of interest are different depending on the problems at hand (Mallick et al., 2012). Bouguer gravity anomaly map registered the density contrast amongst geological features and formations that enables to distinguish individual geological units from an assemblage based on their characteristic gravity signatures. The Bouguer gravity map (Figure 3) shows an overall variation of 33 mGal with the lowest value occurring in the northwest-southeast (NW-SE) (–89 mGal) alignment, while the highest value occurring at the northeast (NE) corner (–56 mGal) in the toposheet of 57 O/14 of the study area.

Such variation in Bouguer gravity anomaly is due to simultaneous effects of lithological diversity and contributions from subsurface crustal components. The anomaly map shows an occurrence of northsouth (N-S) gravity signature (H1) with values ranging from −67 to −56 mGal at the northeast part (Toposheet 57O/14) over migmatite-gneiss and laterite. High gravity antiformal or ridge like structure defined by a pattern of curvilinear or semi-elliptical contours is observed. The long wavelength anomaly H1 almost has an N-S trend and seems to be indicating an occurrence of high density at the deeper crustal level. High gravity enclaves formed by closed contours with values increasing towards centre within these zones, represents fault-bound antiformal structure, that perhaps resulted from shallowing of the mantle. The moderate amplitude anomaly H2 almost has an NE-SW trend and seems to be indicating an occurrence of high-density rock at very shallow depth in the upper crust in the southern portion of Toposheet 57O/11 over migmatite-gneiss. The H3 anomaly trending NW-SE and elliptical in nature seems to be indicating an occurrence of high-density rock at the upper crustal level over migmatite-gneiss in the western portion of the Toposheet 57O/8.

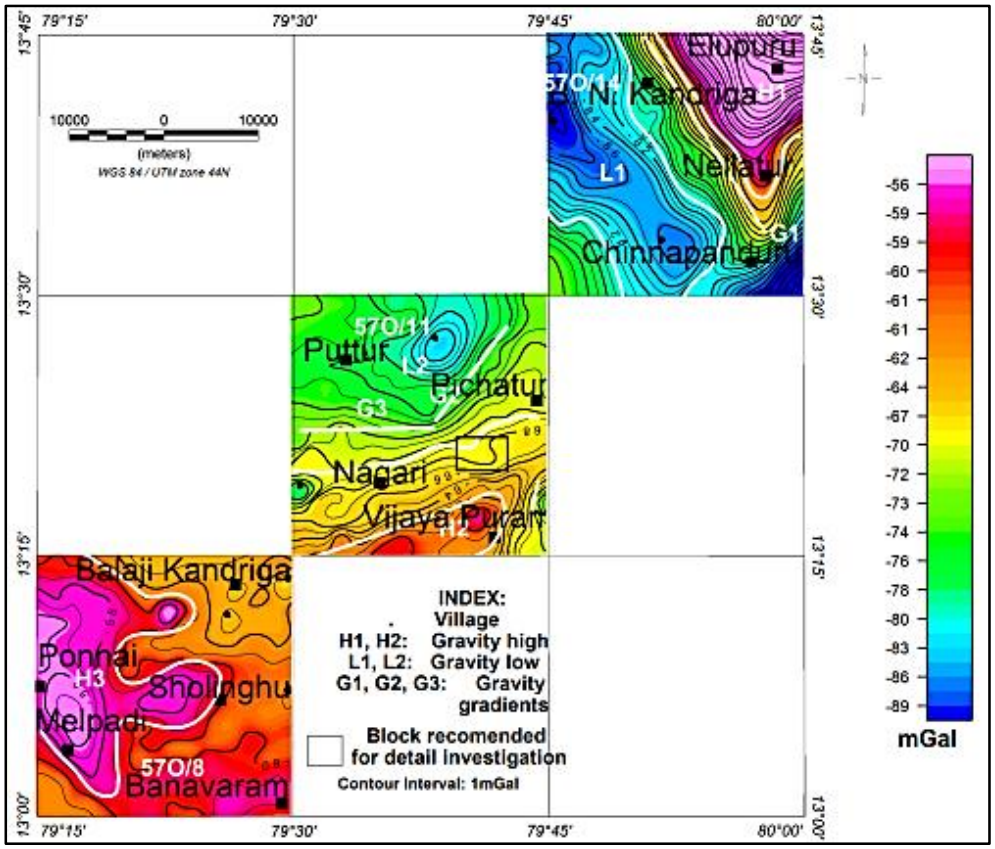

Figure 3. The gridded data of Bouguer gravity anomaly map. Gravity high anomaly: H1, H2 and H3; gravity low anomaly: L1 and L2; gravity gradient: G1, G2 and G3 (GSI, 2019).

The NW-SE aligned gravity low L1 (Toposheet 57O/14) with values ranging from −89 to −76 mGal and almost north south (N-S) aligned gravity low L2 (Toposheet 57O/11) with values ranging from −80 to −73 mGal, suggest the presence of three-dimensional low-density bodies discretized into multiple horizontal layers at the deeper crustal level that has no direct relationship with the exposed lithology. High gravity gradient (about 1.7 mGal/km) zone (G1) stretching over a large area manifested by crowding of contours in the northeast section (Toposheet 57O/14), reflects the existence of a shear/contact zone. Another two high gravity gradients G2 (NE-SW) and G3 (E-W) trends in the Toposheet 57O/11, cut across as it is indicated to form cross structural trends (Joints) representing faulting/shearing/contacts of hornblende-biotite-gneiss and quartzites. Apart from the primary anomaly pattern as discussed above, there are some shallow and deeper level features which will be studied through spectral analysis and potential field transformation in the subsequent sections.

Magnetic anomaly

Magnetic anomaly reflects spatial variation of the magnetic properties of rocks from an observation plane to several kilometres (~22-25 km). The magnetic field is bipolar in nature and induced magnetic field, shape, and magnetic properties of the causative source characterize the observed anomaly. The induced magnetic field is a function of latitude or magnetic inclination. Reduction to Pole (RTP) and Reduction to Equator (RTE) transformations, are used to overcome the complexities of magnetic interpretation (Blakely, 1996). For the present study, mean magnetic inclination (I) was 8.3° and RTE filter applied as in the case of lower magnetic latitudes, RTP is not suitable. We have observed that the RTP introduce some artefacts. The reduction to equator (RTE) operator relocates magnetic anomaly on the top of the causative source, and if induced magnetization is predominant, the bipolar anomalies are removed. It is to be noted that in the case of RTE, the geomagnetic field is predominantly horizontal. For the induced type of magnetization, the magnetic body near the magnetic equator will oppose the geomagnetic field of the earth and negative (low) anomaly will be recorded (Dobrin and Savit, 1988; Mishra, 2011; Ganguli et al., 2019, 2020; Naskar et al., 2020, 2021). Hence, in general, an increase in negative anomaly (magnetic low) indicates an increase in susceptibility and positive (magnetic high) anomaly will be observed over diamagnetic and paramagnetic bodies.

The present study area represents magnetically heterogeneous crust, and magnetic signal contains high frequency anomalies and noise, which can perturb the anomaly trend and mask the meaningful geological attributes. The gridded magnetic data was upward continued to an elevation of 100 m to suppress the high frequency features, or noise contents (Jacobsen, 1987; Hearst and Morris, 2001; Kumar et al., 2009; Ganguli et al., 2019, 2020; Naskar et al., 2022a, b) and then RTE filter was applied. This provides the removal of high frequency noise of the data without significantly smoothening, in context to the present aim and scale of the study. The resultant anomaly map is produced in Figure 4a.

Some distinct anomaly zones can be identified from the RTE map and from visual inspection, which are marked. The very prominent magnetic low zones (L1 to L7, Figure 4a), including some pockets of moderate to high magnetic anomalies, trending in an NW-SE, NE-SW, ENE-WSW and E-W direction respectively, indicates deposition of rocks of high magnetite content around low RTE zones rather than the disposition of mafic/ultramafic rocks. The trend of this zone almost follows the structural trend of the geologically marked features. In the map, these zones are bordered by moderate to high magnetic anomaly zones H1 to H5. The observation of moderate to high magnetic anomaly zones on both sides of magnetic lows indicates lithounits of felsic/acidic character. Pockets of magnetic highs of various sizes and shapes (elliptical/circular/elongated) occur in and around Balaji Kandriga, Ponnai, Melbadi, Banavaram, and Sholinghur that might have resulted from localised enrichment of magnetic minerals in the gneissic complexes around RTE lows (Toposheet 57O/8).

The Bouguer anomaly contour was superimposed further over total magnetic field intensity map using Poisson's relation between gravity and magnetic fields (Blakely, 1996; Mishra, 2011) as the gravity anomalies are more instructive and easier to interpret (Blakely, 1996) than the magnetic anomaly. Figure 4b reveals NW-SE and N-S trend in toposheet 57O/14; ENE-WSW and NE-SW in toposheet 57O/11; E-W and NNW-SSE in toposheet 57O/8. The study area is characterized by lithounits of magnetic nature (mafic/ultramafic) separating two crustal units of felsic/silicic nature.

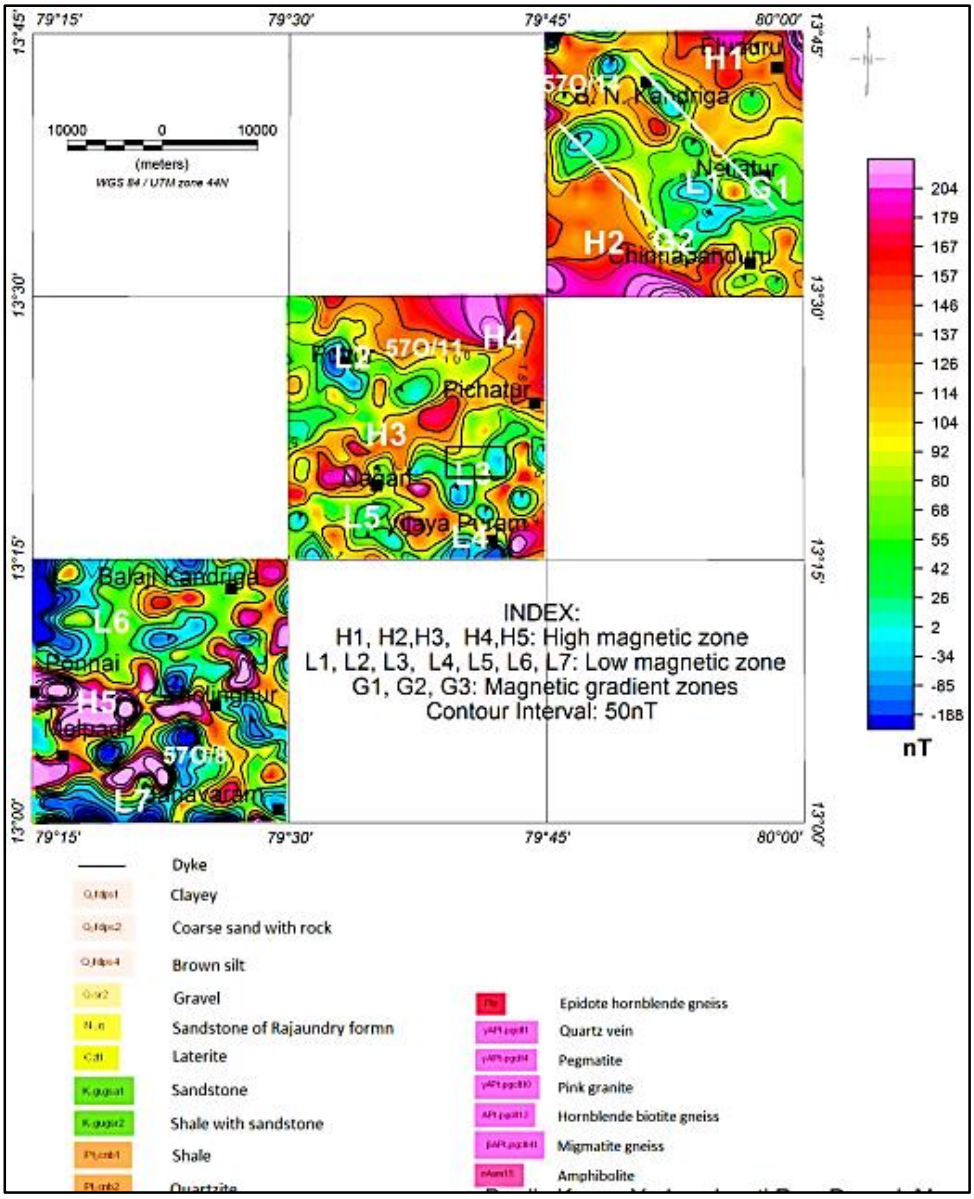

Figure 4. **(a)** Magnetic anomaly (RTE) map. L1 to L7, magnetic low anomaly. H1 to H5, magnetic high anomaly. G1 to G3, magnetic gradient zone (GSI, 2019).

Spectral analysis of gravity and magnetic data

Spectral analysis of gravity and magnetic data is a conventional technique which has wide applications in determination of depths of geological features, such as the basement (Maus and Dimri, 1996). Since, depth of anomalous body controls the shape of power spectrum, it can be determined directly from power spectrum of gravity/magnetic fields by Fast Fourier Transform (FFT) operation. The radially averaged power spectrum was calculated using MAGMAP from Oasis Montaj software.

Spectral analysis of potential field data provides a correlation, between finite depth of source bodies and finite range of wavelengths using the relationship $A(r) = CA_0(r)e^{-2dr}$, where A(r) = Power spectral density of the magnetic field, $A_0(r)$ = Power spectral density of magnetization, r is the wave-number, and d is depth to the magnetic interface (Spector and Grant, 1970; Bansal and Dimri, 2010; Mishra et al., 2012). If we consider, random distributions of stationary, uncorrelated sources (Bansal and Dimri, 2001), $A_0(r)$ becomes constant, and depth to the sources can be found from the slope of the straight line between the logarithmic of the power spectrum ln(A) and wave-number (r). The steepest slope, in the linear segment of the radially averaged power spectrum, identifies the regional signal. The extraction of the residual signal is achieved by

eliminating the wavelengths corresponding to the regional signal. The grid cell size influences the radially averaged power spectrum (Hearst and Morris, 2001). We have gridded the data in 500, 1000, and 2000 m spacing and derived the spectrums.

The depth of the causative source of the gridded gravity and total field magnetic data by radially averaged power spectrum is given by $h = -\frac{s}{4\pi}$, where s is the slope of the log spectrum and h is the depth of the layer interface.

For deepest interface (d1) in gravity data,

Slope of the linear line for layer, $s = -\frac{7-1.5}{0.06} = -91.67$

$$d1 = -\frac{91.67}{4\times3.14} = -7 \text{ km}$$

For middle interface (d2) in gravity data,

Slope of the linear line for layer, $s = -\frac{0.5-(-4)}{0.1} = -45$

$$d2 = -\frac{45}{4\times3.14} = -3.6 \text{ km}$$

For shallow interface (d3) in gravity data,

Slope of the linear line for layer, $s = -\frac{(-3)-(-8)}{0.3} = -16.7$

$$d3 = -\frac{16.7}{4\times3.14} = -1.3$$

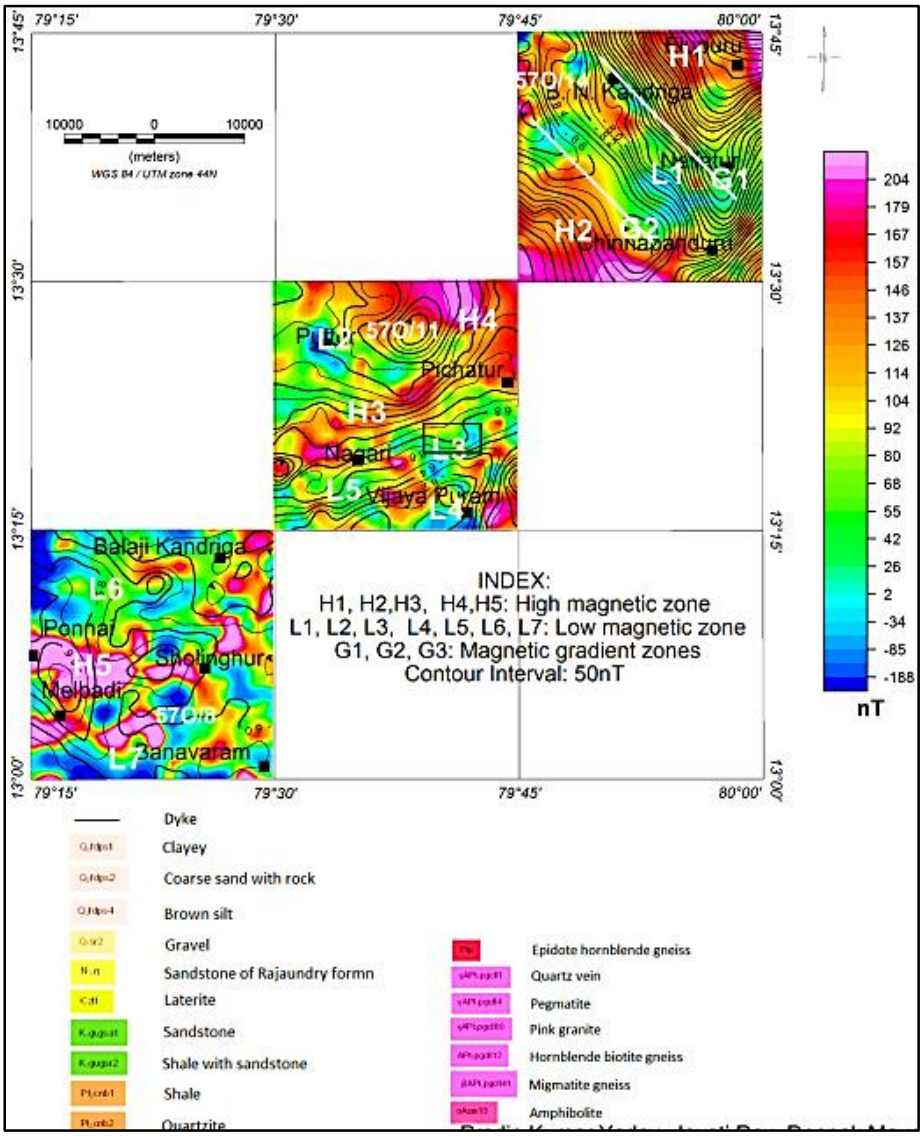

Figure 4b. Bouguer gravity anomaly contour over total field magnetic intensity (TMI) anomaly image map. H1 to H5, magnetic high anomaly zone. L1 to L7, magnetic low anomaly zone. G1 to G3, magnetic gradient zone (GSI, 2019).

Similarly, the depth of the layers in radially averaged power spectrum of magnetic field anomaly was calculated.

The spectrum (Figure 5a) for gravity data show three linear slope segments and corresponding depth values of the sources are provided in Table 3.

It shows that for gravity data, depth values derived for deepest and middle interface are corroborating well for two different grid cell size (500 and 1000 m); however, for the shallowest interface, there is considerable variation (30%) in the derived depth. The results for the grid cell size of 2000 m vary considerably for the middle and shallow interface; however, for the deepest interface result corroborates well (variation 4%). It appears that that grid cell size of 2000 m has excluded high-frequency anomalies caused by shallow sources; as a result, there is a considerable variation in the estimated depth for middle and shallow, it may be the effect of aliasing (Hearst and Morris, 2001). Further, the spectrum, rad-grav-2000, is more scattered than that of rad-grav-500 or rad-grav-1000. For simplicity, we have presented the data for grid cell size of 1000 m to ensure that the data points are adequately sampled, for accurate frequency domain analysis which facilitates depth estimation (Figure 5a)

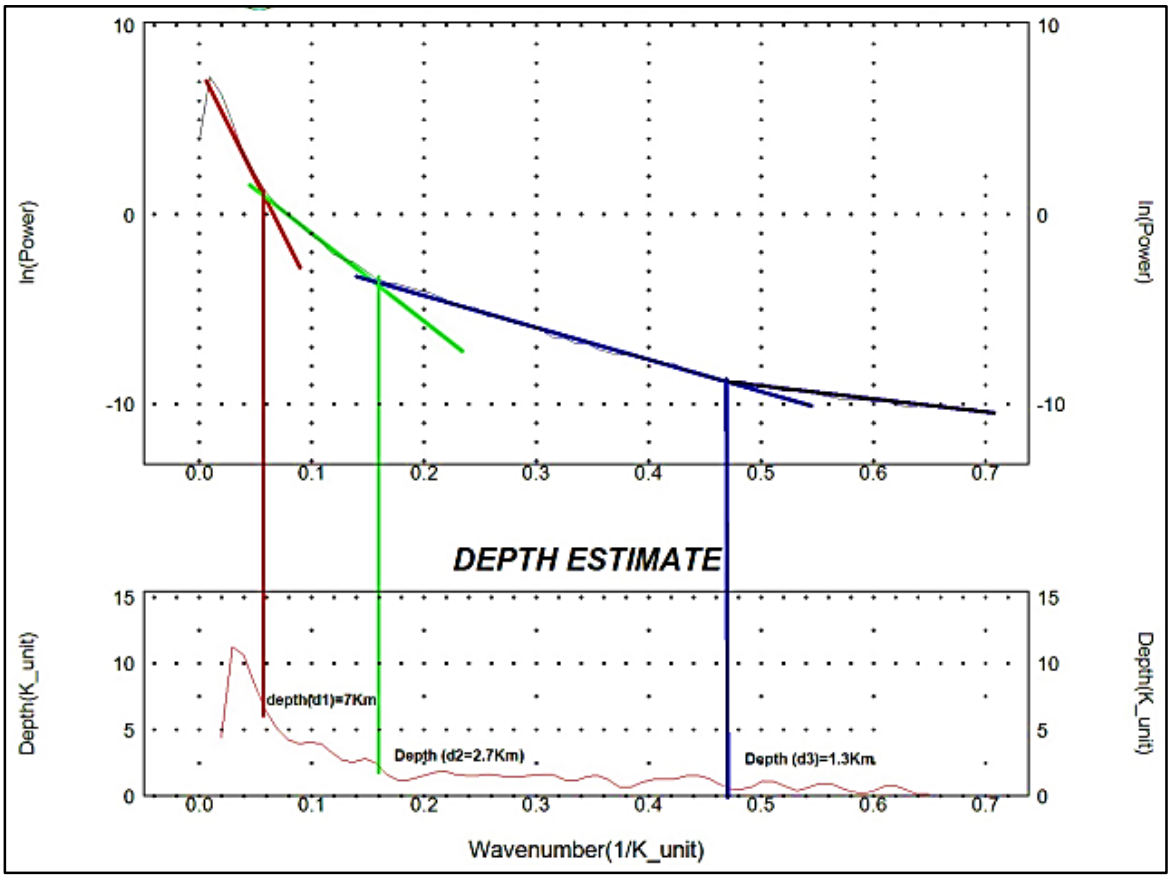

Figure 5a. Radially averaged power spectrum of gravity data for grid cell size 1000 m (GSI, 2019).

Table 3. Comparison of source depth derived from radially averaged power spectrum for different grid cell size (GSI, 2019).

	Depth to interfaces in km for different grid cell size		
Interfaces using gravity data	*500 m grid*	*1000 m grid*	*2000 m grid*
Deepest interface	7	6.88	5.91
Middle interface	3.6	3.58	5.8
Shallow interface	1.3	1.65	2.95
Interfaces using magnetic data	*500 m grid*	*1000 m grid*	*2000 m grid*
Deepest interface	4	3.87	9.1
Shallow interface	1	1.7	1.85

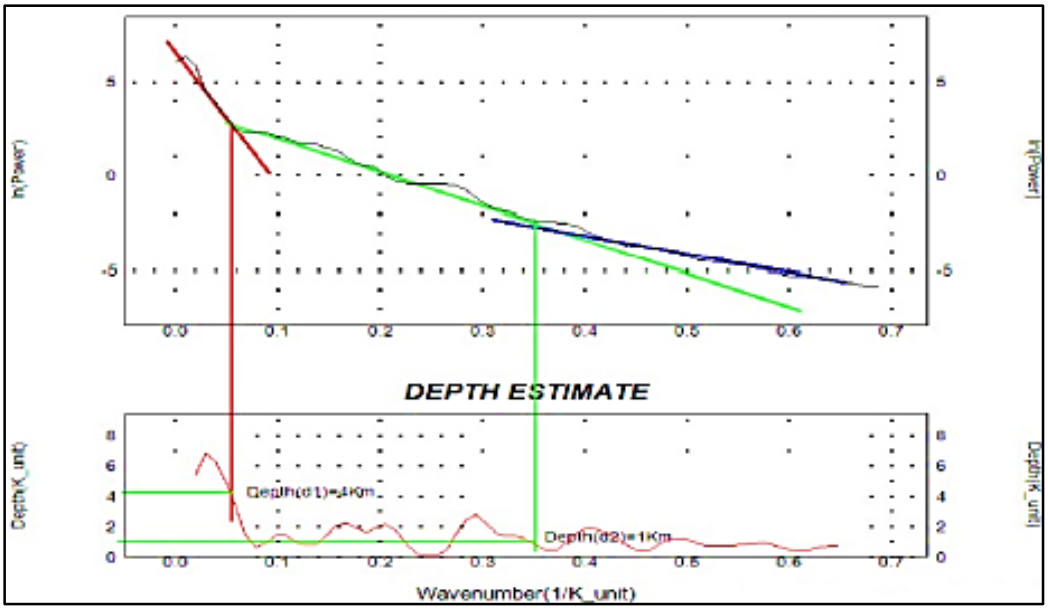

Figure 5b. Radially averaged power spectrum of magnetic data for grid cell size 1000 m (GSI, 2019).

The radially averaged power spectrum of magnetic data shows (Figure 5b and Table 3), two linear slope segments for three different grid cell sizes (500, 1000, and 2000 m). The depth value for deeper interface (d1) derived from grid cell size 500 and 1000 m are well corroborative (variation 2.5%) for the deepest interface, but the shallower interface (d2) exhibit appreciable amount of variation (30%) in the derived depth. Whereas, the depth values derived with grid cell size 2000 m vary more than 100% for the deepest interface (d1). It appears that grid cell size 2000 m is an improper choice for gridding the gravity and magnetic data for the present study. The grid cell size has a more pronounced effect on the depth estimated for shallow interface than the deeper interface from the radially averaged power spectrum.

The density interface at the depth of ~7 km may be indicating an average depth to the interface between amphibole-granulite facies rocks and the underlying high density granulitic crust. Similarly, the second density interface at ~3.6 km may be indicating an average depth to the bottom of the granitic-gneissic terrain that is underlain by the amphibolite- granulite facies crust. The estimated depth for shallowest interface varies with the grid cell size; however, we may take a clue that here exists a density interface at ~1-1.3 km depth. The magnetic interface at ~4 km coincides well with the density interface at ~3.6 km. Similar inferences have earlier been drawn by Agrawal and Pandey (2004) and Pandey (2020). It is to be noted that estimated depths are average and generally an overestimation of the true depth (Negi et al., 1992; Mishra et al., 2012), which can be considered as the upper bound of the depth estimates.

Analysis of regional and residual of gravity anomalies

In the exploration of minerals, hydrocarbons and other resources, the targets lie at shallower depths. Therefore, the deeper effects that mask the shallower effects need to be separated from the combined response. The amplitude and wavelengths of the observed gravity anomalies at the plane of observation represents contributions from anomalous sources at different depths with some noise component. Regional and residual separation is an attempt to isolate the field produced by near surface sources (residual) from those which are produced by deep-seated sources (regional). Now, it is evident that the shallower and deeper components need to be resolved before any further analysis of the Bouguer gravity data is carried out. On a Bouguer gravity residual map, the response of shallower feature appears sharp and narrow as closures or nosings in the contour patterns whereas, the regional component due to their deep-seated origin are broad and have a uniformly varying gradient. Rao (1996) observed over the continents that the Bouguer gravity anomalies, in general, have negative values. Over this regional field anomalies of special interest (residuals), caused by changes in subsurface geology, are superposed as highs and lows. Cause of these negative values of regional nature though is known to be related to compensation of topographic masses, no direct method is available to compute the regional field.

For the present study, wavelength analysis is applied for the spectral analysis of the potential field data (Spector and Grant, 1970; Telford et al., 2001; Mishra, 2011). The spectral analysis of gravity data indicates that the cut-off wavelength

separating deeper and shallower source is 0.03-unit wave number (Figure 5a). Residual anomaly is extracted by applying a Butterworth band pass filter to the gravity data with the wave number ranging from 0.03- to 0.8-unit in order to obtain specific frequency components of interest while attenuating frequencies outside that range. A low pass filter with wave-number 0.03-unit is applied to the Bouguer gravity data for deriving of the regional field.

The residual gravity anomaly map (Figure 6) brings out the disposition of shallow crustal structure which is otherwise subdued in the gravity anomaly map as deeper density sources producing long wavelength anomalies mask some short wavelength features. We have demarcated prominent residual high anomalies in the map (L1 to L5). The anomalies are generally showing a NW-SE trend. The NW-SE trending linear residual gravity highs (L1 to L5) are flanked by linear gravity lows. The low residual gravity anomalies are mostly represented by elongated fashion and are interpreted as minor shears where mineralization has occurred.

In the residual map two high closures IN1 (Toposheet 57O/8) and IN3 (Toposheet 57O/11)) respectively are recorded south of Balajikandriga and southwest of Vijaya Puram which are inferred as intrusion of high-density material. The circular positive residual gravity anomalies of the region may due to a major fault separating major positive and negative anomalies. Two low closures IN2 (Toposheet 57O/8) and IN4 (Toposheet 57O/11) respectively are observed around Balaji Kandriga and northeast of Vijaya Puram which are inferred as intrusion of low-density material.

The regional gravity map is derived by applying low pass filter with wave number 0.03-unit (Figure 7), and the generated map shows smooth isogals with high gravity imprints respectively in Elupuru (Toposheet 57O/14) and in Ponnai-Melpad section (Toposheet 57O/8). These signatures are the cumulative imprints of a deeper level source of the gravity high zone H1 (Figure 3).

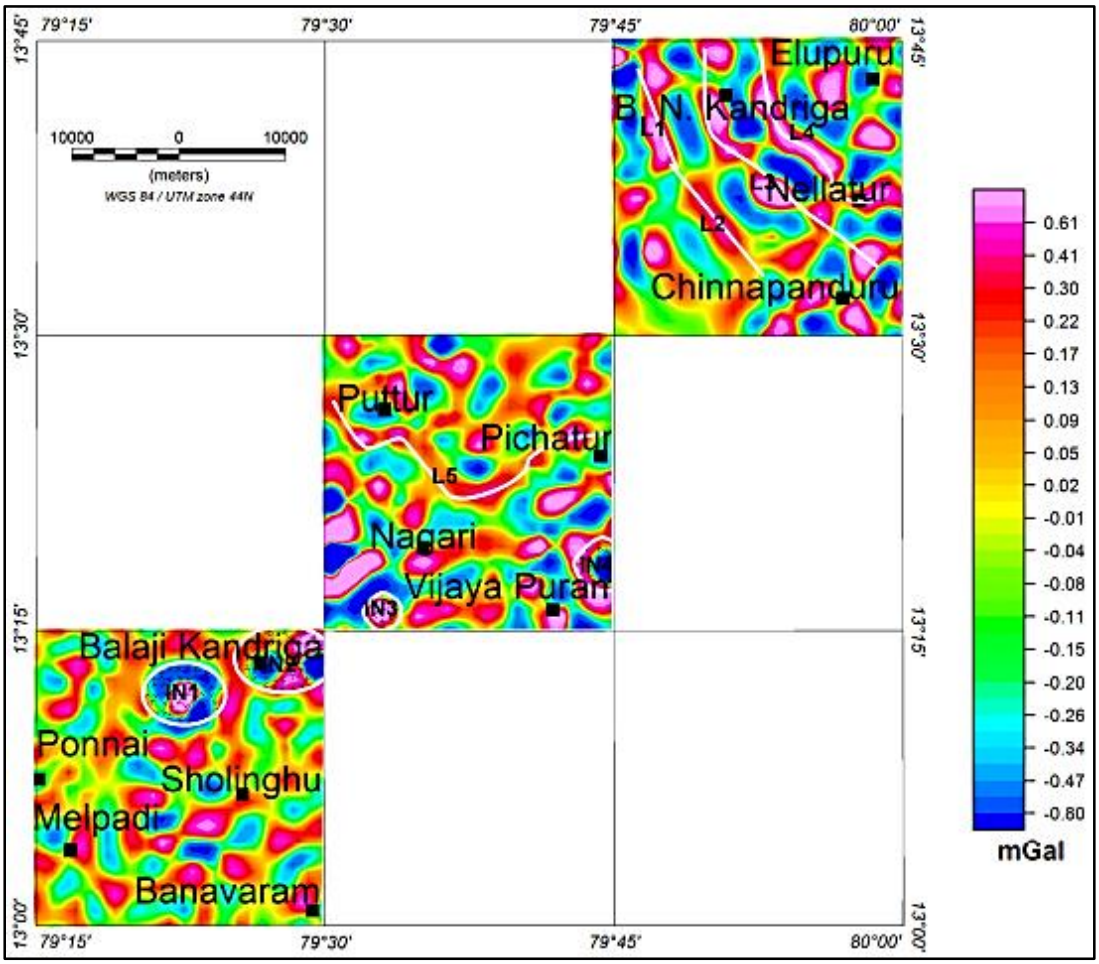

Figure 6. Residual Bouguer gravity map. Linear white line (L1 to L5) indicates tentative boundaries of residual gravity high and white closed circle indicates intrusive bodies (IN1 to IN4) (GSI, 2019).

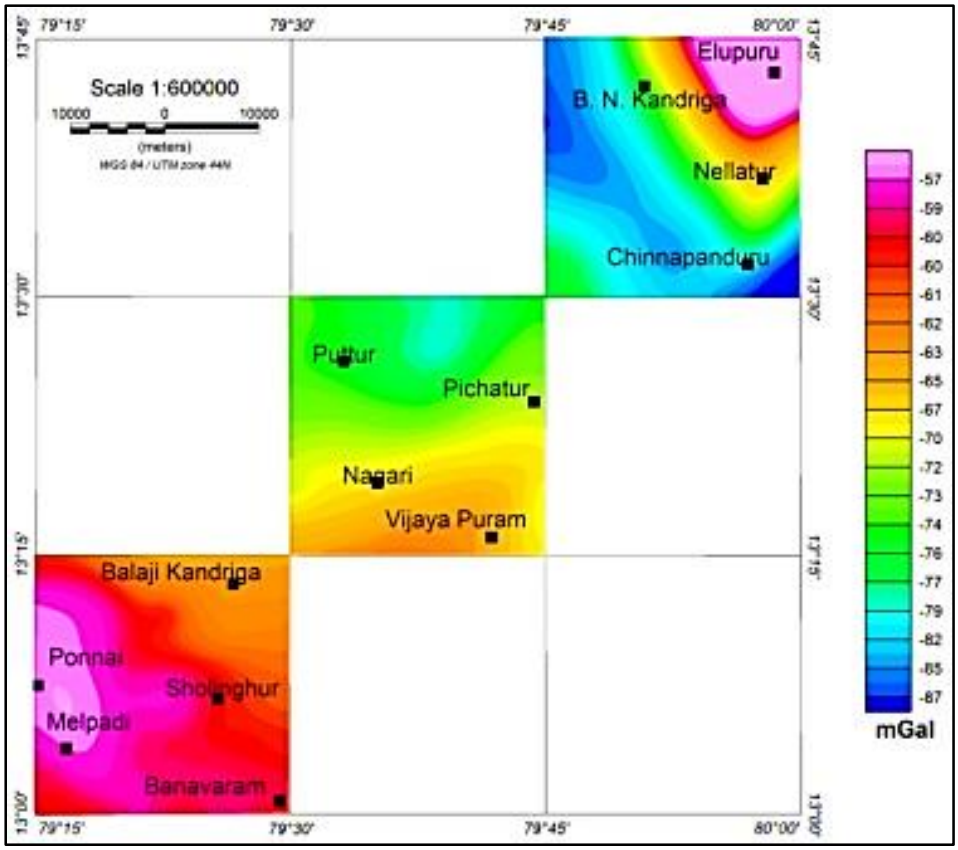

Figure 7. Regional Bouguer gravity anomaly map (GSI, 2019).

The residual gravity low at the southwest of L1 and L2 (Figure 6) corroborates well with the exposed granite/biotite gneiss and also coincides with the regional gravity low, indicating deeper depth extension of the exposed one. It may also indicate an increase in the crustal thickness.

It is interesting to note that the residual gravity high anomalies (e.g. L5) in Toposheet 57O/11 (Figure 6), are in good corroboration with the exposed high-density ultramafic bodies, which are eliminated in the regional map (Figure 7) indicating their limited depth extent. The upward continued map has also brought out long wavelength anomalies associated with the deeper part of PGC-II and Cuddapah Supergroup rocks. It is evident that there are two major lithological domains i.e. PGC-II and Cuddapah Supergroup depending on density contrasts. The elliptical/oval (Toposheets 57O/8 and 57O/14) shape of the gravity highs indicates that the causative high-density source was subjected to tectonic forces after emplacement due to the stretching of the crust leading to the formation of the elliptical anomaly

Horizontal gradient map of gravity and magnetic data

Horizontal gradient map is useful in delineating the boundaries of abrupt lateral changes in density or magnetization (Nabighian, 1972, 1984; Blakely, 1996; Kumar et al., 2011; Mishra, 2011). In this process, short wavelength anomalies are enhanced, and the gradient is located directly over the edges of the density/magnetic discontinuity (Pal et al., 2016; Narayan et al., 2017; Pal and Kumar, 2019; Kumar et al., 2020). The location of maxima of horizontal gradient magnitude can be simply identified by visual inspection (Pal and Majumdar, 2015; Pal et al., 2016; Sahoo and Pal, 2019; Chouhan et al., 2020). Derivative map, also known as gradient map, displays the highlighted features resulted from the horizontal or vertical derivatives of potential field (Alvandi and Asil, 2014).

In gravity interpretation, the edges come in many forms and shapes. They might be in the form of faults, contacts, and various structural boundaries (Blakely and Simpson, 1986). In order to highlight lineaments of gravity data, use of a truncated horizontal plate model is familiar. The truncated horizontal plate model is a popular structure for geophysical studies. This model, shown in xz cross-section in Figure 8, semi-infinite in the positive x axis direction, is bounded by upper and lower horizontal planes z_1 and z_2. Assuming uniform density distributions in the model and the surrounding medium, the gravity effect, and the first and

second horizontal derivatives, are given by, respectively (Telford et al., 1976),

$$g = 2k\Delta\rho\left\{x\log\frac{r_2}{r_1} + z_2\left(\frac{\pi}{2} + \theta_2\right) - z_1\left(\frac{\pi}{2} + \theta_1\right)\right\}$$

$$g_x = 2k\Delta\rho\left\{\log\frac{r_2}{r_1}\right\}$$

$$g_{xx} = 2k\Delta\rho\left\{\frac{x}{r_2^2} - \frac{x}{r_1^2}\right\}$$

where k is the gravitational constant, and ρ is the density contrast between the model and the surrounding medium. Here, g is the gravity data; g_x and g_{xx} are the first and second horizontal derivatives respectively in the x direction. Many filters are available to enhance subtle detail in potential field data, such as downward continuation, horizontal and vertical derivatives, and other forms of high pass filters. A commonly used edge detection filter is the total horizontal derivative (Cooper and Cowan, 2008). It can be used to enhance certain features, smooth out noise or highlight previously known shape in potential field data.

After gravity data are transformed into the gradient domain, a threshold can be given, and the gradient magnitude whose corresponding gradient values are greater than the threshold can then be obtained (Prewitt and Mendelsohn, 1966; Otsu, 1979; Pun, 1980; Tsai, 1985). These maxima indicate the strike of lineaments. This is the lineaments identification procedure. Enhancement, or attenuation of certain lineaments can be realized through non-maximum suppression. The edge map is obtained by taking the gradient of the input data and limiting it to an available threshold value. All values below the threshold are set to zero. However, it is difficult to choose a proper threshold. Because of this difficulty, in the edge map there may still be false edges if the threshold is too low or some edges may be missing if the threshold is too high (Peli and Malah, 1982; Hertz and Schafer, 1988; Chen and Shrestha, 2000; Sun et al., 2007; Chen and Ho, 2008). A double threshold can be applied to overcome this problem. Local maxima of the gradient magnitude determine edges in the input data. This approach can be used to extract geological features such as faults and contacts from a gravity anomaly map.

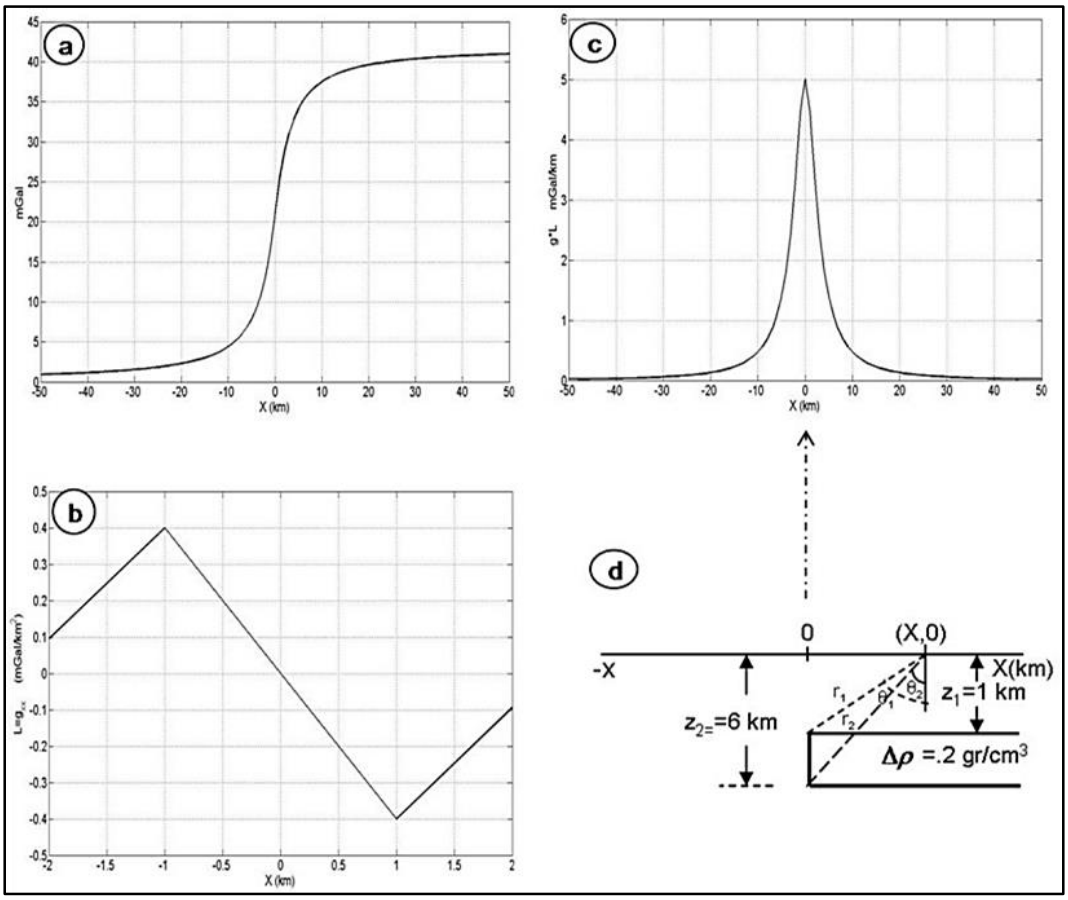

Figure 8. **(a)** Gravity profile of the truncated horizontal plate model shown in **Figure 8(d)**, **(b)** 1D gradient operator, **(c)** Convolution output and **(d)** Plain view of the truncated horizontal plate model, z_1 is the depth to the top of the model, z_2 is the depth to the bottom of the model, ρ is the density contrast (Aydogan, 2011).

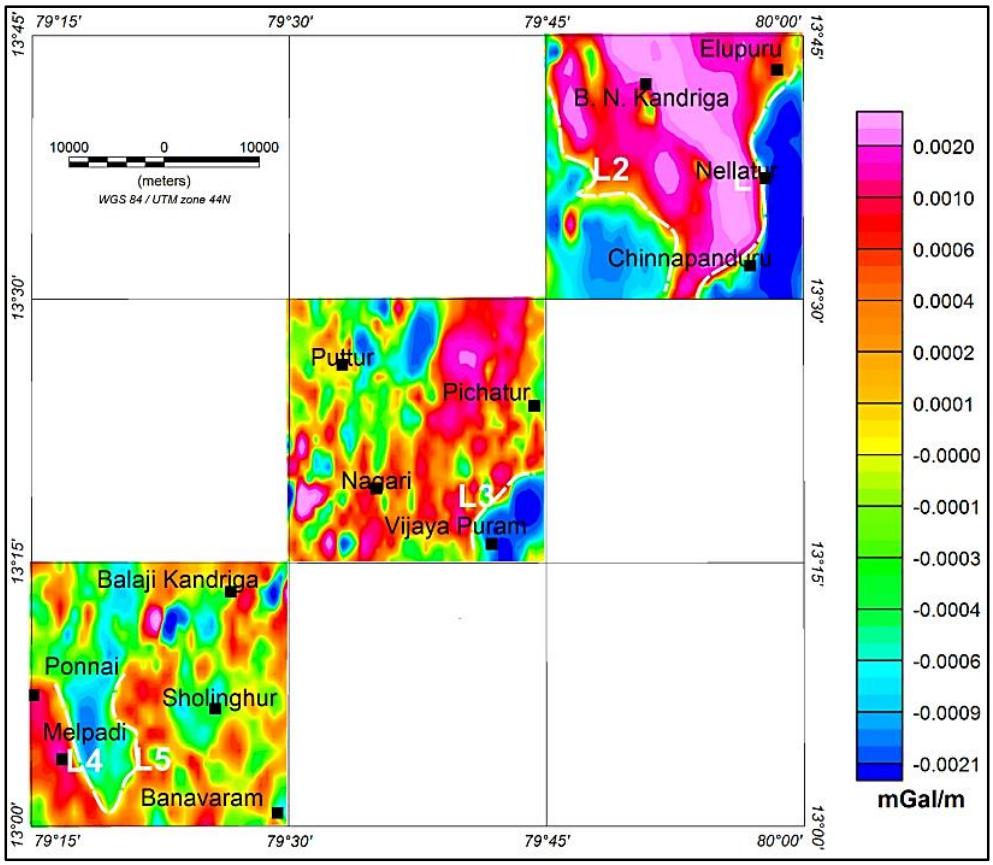

Figure 9a. Horizontal gradient of Bouguer gravity data (GSI, 2019).

The horizontal gradient gravity anomaly map is presented in Figure 9a. The general trend approximately varies from NE-SW to NNW-SSE. The N-S components in this map can be attributed to specific geological features and density variations.

The structural fabric derived from horizontal gradient of gravity data is in strong corroboration with the geological inferences. An NNW-SSE linear contact (L2) and NE-SW linear contact (L1) which resembles with the PGC-II and Cuddapah basin contact zone and contact between PGC-II and laterite of Cenozoic age and sandstone of Rajahmundry formation respectively. The NE-SW linear contact (L3) is interpreted as the contact of PGC-II and sandstone of Gondwana formation. Few minor contacts (L4, L5) with nearly N-S orientation also appear in the gradient map in the southern part.

Magnetic peaks appear around Ponnai, Banavaram, Sholingur in the southern part (Toposheet 57O/8), Puttur, Vijaya Puram in the middle part (Toposheet 57O/11) and Nellatur and west of B N Kandriga in the northern part (Toposheet 57O/14) of the area (Figure 9b) contrary to the magnetic anomaly map (Figure 4a), which shows low magnetic intensity in these areas because of effect of low magnetic latitudes. Maxima with nearly N-S (L4), NW-SE (L2, L3 and L4) trends represents high intensity which could be related to shallow contacts/structures of magnetic nature causative sources (Figure 9b). The contacts of PGC-II and Cuddapah basin (L1) and PGC-II and Gondwana formation (L4) are well reflected in the magnetic gradient map.

The abrupt changes in lithological properties in terms of density and magnetization are observed. The dominance of NE-SW and NW-SE structural fabrics is also observed. The analysis of gradient map enabled in establishing the NE-SW, NW-SE, N-S aligned linear as well as in identifying contacts of various lithounits and depicted their strike continuity of shallow geological features. Magnetic gradient map is useful in locating the edges of magnetic source bodies; particularly where magnetic latitudes and/or remnant magnetization low complicates the interpretation. The area under investigation lies in the low magnetic latitudes which may cause complexities in magnetic signatures due to low inclination of induced magnetic field.

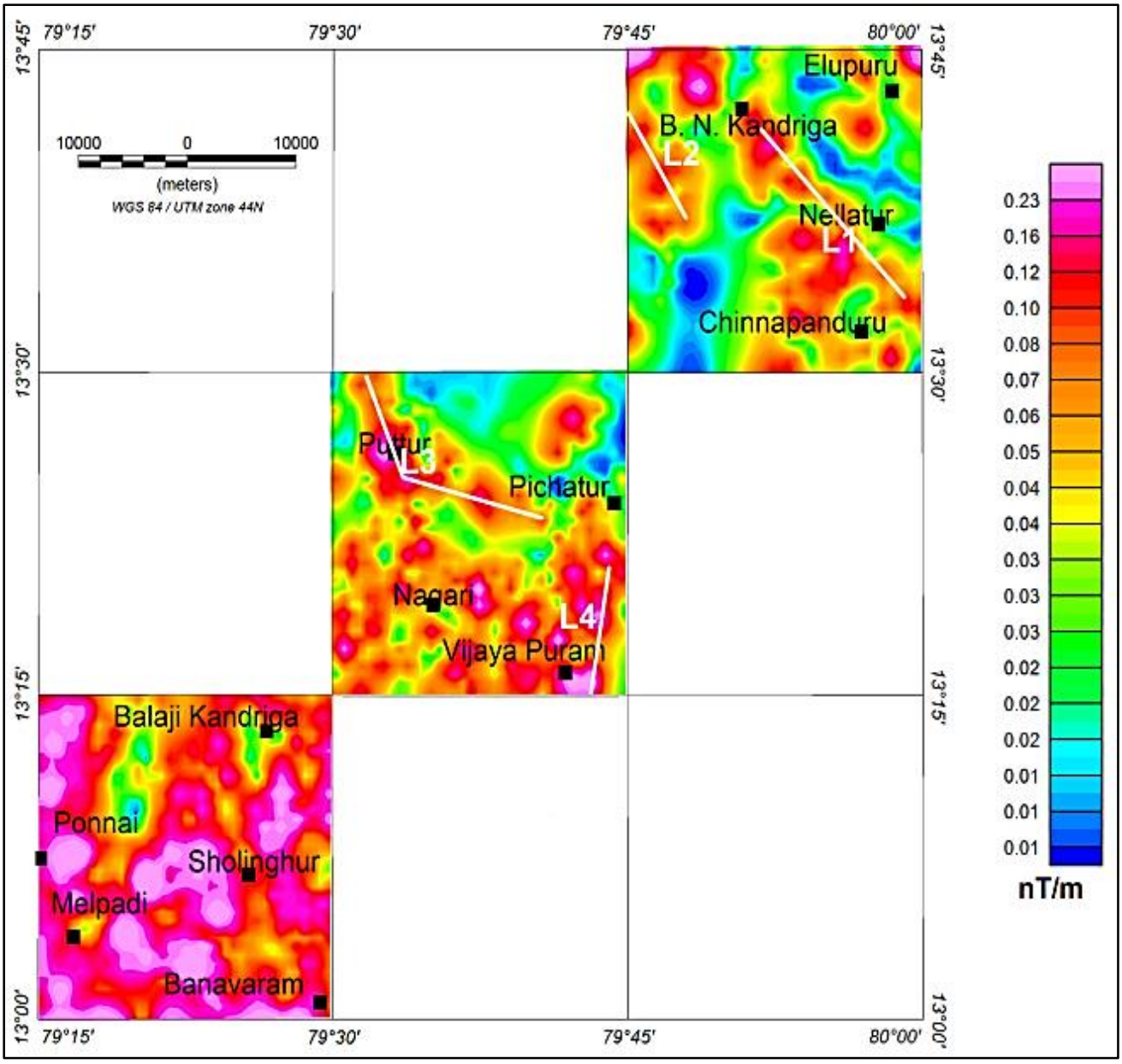

Figure 9b. Horizontal gradient of magnetic data (GSI, 2019).

Derivative map of Bouguer gravity anomaly

The second vertical derivative map of gravity anomaly has also been produced by FFT method. The result is an enhanced anomaly map or residual map which has amplified anomalous signals associated with shallow features while de-emphasizing regional features. Anomaly pattern in the northernmost part (Toposheet 57O/14) exhibits nearly N-S trending (L1, L2) high gravity gradients resembling the disposition of formational contacts, faults, shear zones or lineaments (Figure 10). The trend of signals forming the linear tracts with almost N-S alignment (L4) near Pichatur (Toposheet 57O/11) in the central part is indicative of contact between PGC-II and Cuddapah basin. Few NE-SW and NW-SE trending linear (L5, L7, L8, L9, L10) positive anomalies related to high density materials have also been enhanced north of Pichatur, around Vijaya Puram, near Sholinghur, near Melpadi and north of Banavaram respectively.

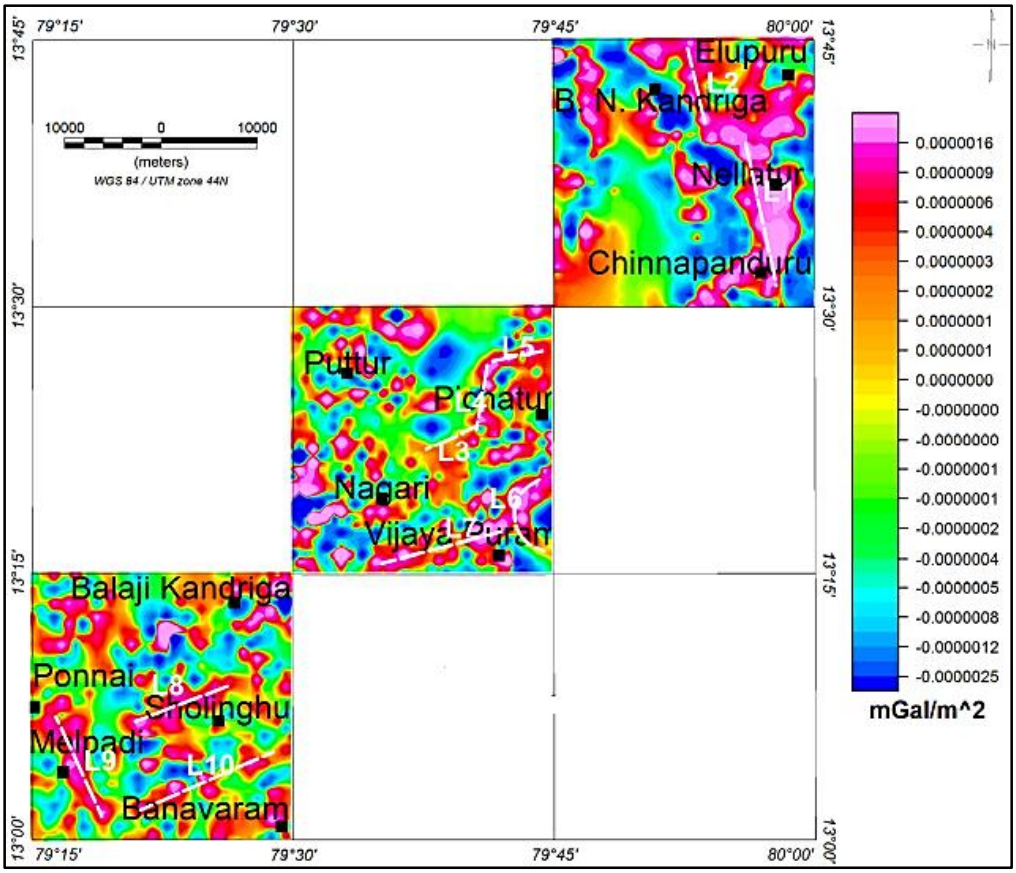

Figure 10. Second vertical derivative of Bouguer gravity anomaly map (GSI, 2019).

Table 4. Structural Index (SI) (Reid et al., 1990).

SI	Magnetic field	Gravity field
0	contact	sill/dyke/step
0.5	thick step	ribbon
1.0	sill/dyke	pipe
2.0	pipe	pipe/cylinder
3.0	sphere	sphere/circular bodies

3D Euler deconvolution for depth estimation

Euler deconvolution has come into wide use as an aid to interpreting profile or gridded magnetic survey data. It provides automatic estimates of source location and depth. In doing this, it uses a structural index (SI) (Table 4) to characterise families of source types. Euler deconvolution can be usefully applied to gravity data (Reid et al., 1990; Reid and Thurston, 2014).

The structural index (SI) is based on the concept of Euler homogeneity, a description of scaling behavior. It has found wide use in potential field depth estimation and is a constant integer for simple sources with single singularities (points, lines, thin-bed faults, sheet edges, infinite contacts).

In the present study, the technique has been applied to gravity and magnetic data for depth persistence of causative bodies. Data have been processed with Geosoft software to find depth solutions by Euler deconvolution technique. Each calculation has been run for grid cell sizes 1000 m, SI (0, 1, and 2) and window lengths (8 km and 4 km) to derive depth solutions for causative bodies. Logical solutions have been considered for interpretation of results. Best solutions for gridded data of Bouguer gravity anomaly have been obtained for grid cell size of 1000 m for SI = 0, window size = 4 km × 4 km, and depth tolerance = 8% (Figure 11a).

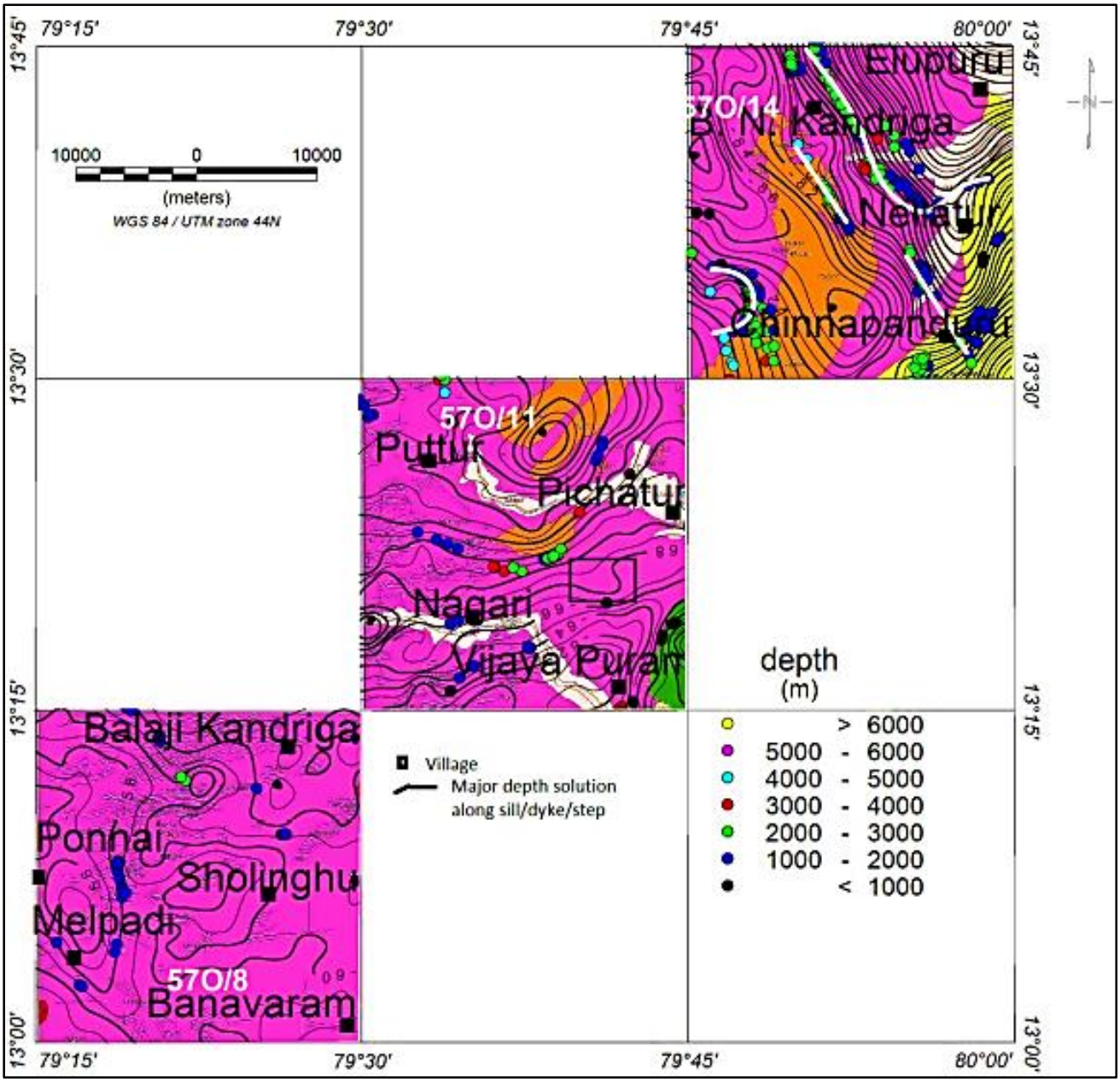

Figure 11a. Overlay of Euler depth solution (SI = 0) of gravity data on geological map (GSI, 2019).

The solutions have been superimposed on the combined geological and gravity contour map of the area which highlights some lithological/tectonic contacts with variable depths. Major number of solutions has been obtained for the signal source depth ranging from 1000-2000 m, 2000-3000 m and 4000-5000 m respectively. The linear distribution of plots of solution in NW-SE direction is observed over the exposed contact between PGC rocks and Cuddapah Supergroup of rocks around B N Kandriga and Nellatur section (Toposheet 57O/14).

Depth solutions derived from magnetic data for grid cell size 1000 m, SI (0), window size 6 km × 6 km, and depth tolerance 8%, have been plotted on the combined geological and magnetic anomaly contour map (Figure 11b). Both gravity and magnetic data plays complementary roles in geophysical exploration and using similar window sizes ensures consistency in data processing and interpretation.

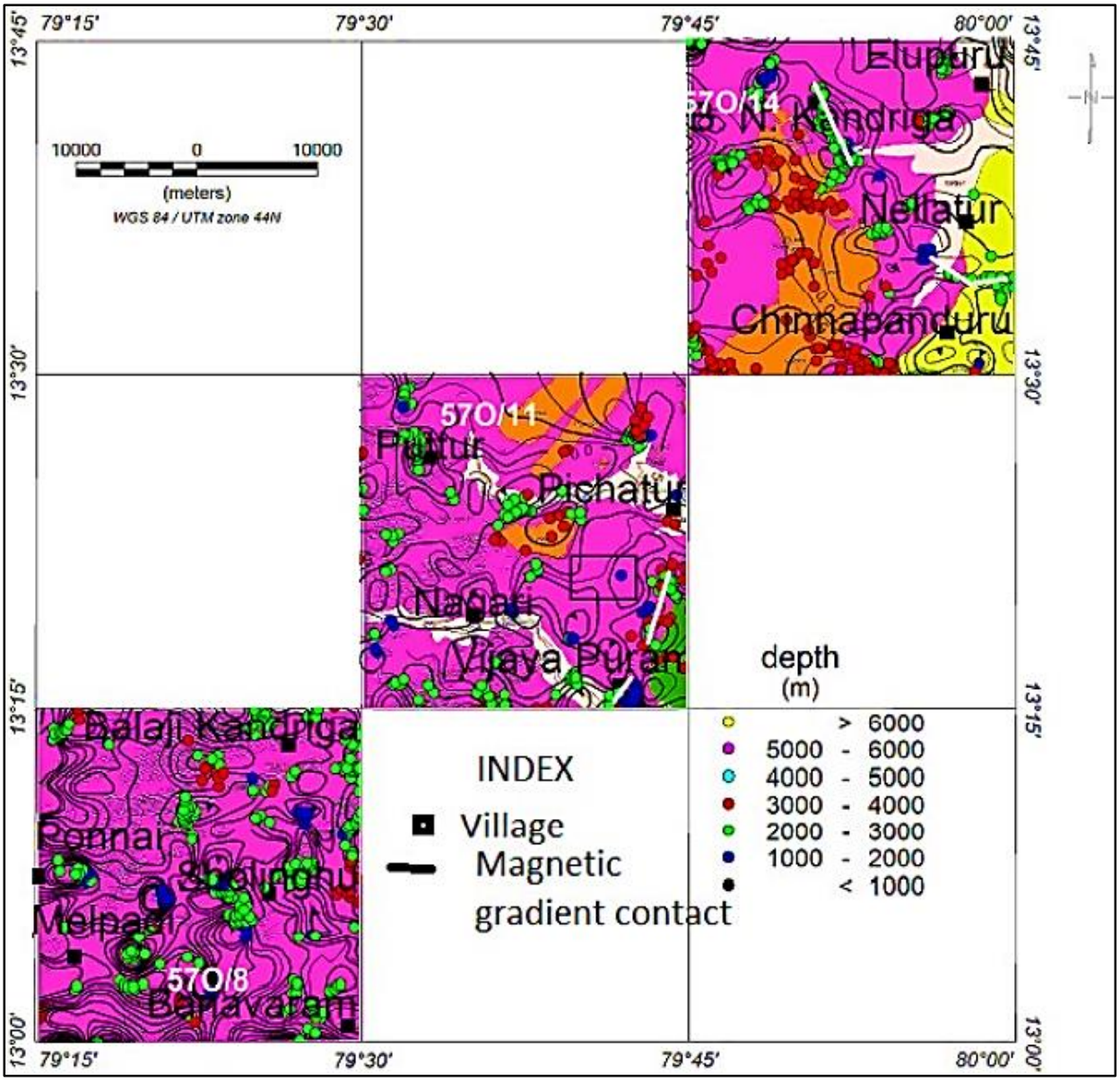

Figure 11b. Overlay of Euler depth solution (SI = 0) of magnetic data on geological map (GSI, 2019).

Major responses are from source bodies occurring at depth from 1000 m to 4000 m. In the middle (Toposheet 57O/11) and southern (Toposheet 57O/8) part, scattered depth solutions are observed due to lack of susceptibility contrast. Prominent linear contact between PGC II and Cuddapah Supergroup south of B N Kandriga is observed (Toposheet 57O/14). Major depth solution (3000-4000 m) is observed over exposed PGC II and Cuddapah Supergroup of rocks due to sharp contrast in susceptibility (Toposheets 57O/14 and 57O/11). Contact of Gondwana sediments and PGC II is also clearly demarcated with depth solution at (2000-3000 m) (Toposheets 57O/14 and 57O/11).

CONCLUSIONS

The present study deciphered the density and susceptibility contrasts between the anomalous mineral concentration and the host rock or the deep-seated crustal structures and adjacent rocks. The terrain corrected Bouguer gravity and IGRF corrected magnetic (Total field) maps prepared at 1 mGal and 50 nT intervals respectively, have shown distinct gravity and magnetic signatures over two major geotectonic domains namely PGC II and Cuddapah Supergroup, which represent two tectonic blocks separated by a nearly NW-SE trending crustal break extending in crustal level. Development of geophysical responses in these domains is

controlled by both formation lithology and crustal structures. Low to moderate gravity and low magnetic signals are associated with granite and metasediments (schists, phyllites, quartzite) while high signals are yielded mainly by biotite gneiss, granite-gneiss. Low gravity anomaly zones correspond to high crustal thickness while high gravity over low to moderate density materials, possibly implies the existence of an antiformal structure resulting from the shallowing of the mantle. Strong dipolar magnetic anomaly is associated with PGC II and Cuddapah Supergroup of rocks as well as Gondwana sediments depending on the susceptibility contrast. Formation contacts of PGC II-Cuddapah Supergroup and PGC II-Gondwana sediments are represented by gravity gradient zones and dipolar magnetic anomalies. Some intra-formational fracture and fault zones are also manifested by preferred orientation of crowded contours. Gravity and magnetic signatures in the area are mainly controlled by shallow crustal features. The area is composed of three major domains of contrasting densities and magnetic susceptibilities – amphibolites of the Archean basement, Cuddapah Supergroup of rocks and sequences of rock formation of Cenozoic period.

Acknowledgements

The authors express sincere thanks to the since Director General, Geological Survey of India (GSI), for his continuous encouragement and support and for the permission to publish this work. We also thank the two reviewers for their comments and suggestions that have helped to improve the quality of the manuscript. Authors also express their sincere gratitude to the Chief Editor of the journal for his effortless contribution to improve the quality control of the present work to publish in the Journal of Indian Geophysical Union (IGU), Hyderabad, India.

Author credit statement

Each author contributed commonly towards the preparation of the manuscript, conceptualization, methodology, software, validation, formal analysis, investigation, data curation, project administration and funding acquisition.

Data availability

The Geological Survey of India (GSI), Southern Region, Hyderabad, provides a wealth of geospatial and geoscientific data. This data is accessible through various platforms and initiatives like, National Geoscience Data Repository (NGDR) (which hosts a comprehensive collection of geoscientific data, including reports and maps generated by GSI) and National Geochemical Mapping (NGCM) (which includes seamless geochemical maps of 64 elements) and Open Geospatial Data through the data.gov.in portal, which includes datasets from various ministries, including the Ministry of Mines and the Geological Survey of India.

Compliance with ethical standards

The authors declare that they have no conflict of interest and adhere to copy right norms.

REFERENCES

Agrawal, P.K. and Pandey, O.P., 2004. Unusual lithospheric structure and evolutionary pattern of the cratonic segments of the south Indian shield. Earth Planets Space, 56, 139-150

Alvandi, A. and Asil, R.H., 2014. Edge detection process of Qom salt dome gravity anomalies using hyperbolic tilt angle. Int. J. Geomatics and Geoscience, 5(2), 209-224

Aydogan, D., 2011. Extraction of lineaments from gravity anomaly maps using the gradient calculation: Application to Central Anatolia. Earth Planets Space, 63, 903-913.

Bansal, A.R. and Dimri, V.P., 2001. Depth estimation from the scaling power spectral density of non-stationary gravity profile. Pure Appl. Geophys., 158(4), 799-812.

Bansal, A.R. and Dimri, V.P., 2010. Scaling spectral analysis: A new tool for interpretation of gravity and magnetic data. Earth Science India, 3, 54-68.

Blakely, R.J. 1996. Potential theory in gravity and magnetic applications. Cambridge, UK: Cambridge University Press.

Blakely, R.J. and Simpson, R.W., 1986. Approximating edges of source bodies from magnetic or gravity anomalies, Geophysics, 51, 1494-1498.

Chen, C.H. and Shrestha, B., 2000. Classification of multi-sensor remote sensing images using self-organizing feature maps and radial basis function networks. In: Proceedings of International Geosciences and Remote Sensing Symposium (IGARSS), Hawaii.

Chen, C.H. and Ho, P.G., 2008. Statistical pattern recognition in remote sensing. Pattern Recognition, 41, 2731-2741.

Chouhan, A.K., Singh, D., Pal, S.K. and Choudhury, P., 2020. Delineation of subsurface geological fractures in the Cambay rift and surrounding regions of NW India: An integrated approach using satellite derived EIGEN-6C4 gravity data. Geocarto Int., 1-16.

Cooper, G.R.J. and D. R. Cowan, D.R., 2008. Edge enhancement of potential field data using normalized statistics. Geophysics, 73, H1-H4.

Dentith, M. and Mudge, S.T., 2014. Geophysics for the mineral exploration Geoscientist. New York, NY, Cambridge University Press.

Dobrin, M.B. and Savit, C.H., 1988. Introduction to geophysical prospecting. New York, NY: McGraw-Hill.

Gandhi, S.M. and Sarkar, B.C., 2016. Essentials of mineral exploration and evaluation. 1st Edition Amsterdam, Netherlands, Elsevier.

Ganguli, S.S., Singh, S., Das, N., Maurya, D., Pal, S.K. and Rama Rao, J.V., 2019. Gravity and magnetic survey in south western part of Cuddapah Basin, India and its implication for shallow crustal architecture and mineralization. J. Geol. Soc. India, 93(4), 419-430.

Ganguli, S.S., Pal, S.K., Rama Rao, J.V. and Sunder Raj, B., 2020. Gravity magnetic appraisal at the interface of

Cuddapah Basin and Nellore Schist Belt (NSB) for shallow crustal architecture and tectonic settings. J. Earth Syst. Sci., 129, 92.

Garcia-Lobon, J.L., Rey-Moral, C., Ayala, C., Martín-Parra, L.M., Matas, J. and Reguera, M.I., (2014). Regional structure of the southern segment of Central Iberian Zone (Spanish Variscan Belt) interpreted from potential field images and 2.5 D modelling of Alcudia gravity transect. Tectonophysics, 614, 185-202.

GSI, 1993. Geological quadrangle map. Geological Survey of India Unpublished Report, Kolkata.

GSI, 1998. Geological map of India on 1:2000000 scale. Kolkata, India: Geological Survey of India Publication.

GSI, 2019. A report on regional gravity and magnetic (TF) surveys in Toposheet nos. 57J/15, 57J/16, 57O/8, 57O/11, 57O/14 in parts of Chittoor, Nellore, Prakasham districts in Andhra Pradesh and Vellore, Thiruvallur districts in Tamil Nadu under the project: National Geophysical Mapping (NGPM). Field Season: 2018-2019, Mission: I (Geophysical Mapping). Geological Survey of India Unpublished Report.

Harinarayana, T., Naganjaneyulu, K., Manoj, C., Patro, B.P.K., Begam, S.K., Murthy, D.N. and Virupakshi, G., 2003. Magnetotelluric investigations along Kuppam-Palani geotransect, south India, 2D modelling results. Mem. Geol. Soc. India, 50, 107-124.

Harinarayana, T., Naganjaneyulu, K. and Patro, B.P.K., 2006. Detection of a collision zone in south Indian shield region from magnetotelluric studies. Gondwana Res., 10(1-2), 48-56.

Hearst, R.B. and Morris, R.B., 2001. Regional gravity setting of the Sudbury structure. Geophysics, 66(6), 1680-1690.

Hertz, L. and Schafer, R.W., 1988. Multilevel thresholding using edge matching. Comput. Vision Graphics Image Process., 44, 279-295.

Jacobsen, B.H., 1987. A case for upward continuation as a standard separation filter for potential field maps. Geophysics, 52(8), 1138-1148.

Kumar, N., Singh, A.P. and Singh, B., 2009. Structural fabric of the southern Indian shield as defined by gravity trends. J. Asian Earth Sci., 34(4), 577-585.

Kumar, N., Singh, A.P. and Singh, B., 2011. Insights into the crustal structure and geodynamic evolution of the southern granulite terrain, India, from isostatic considerations. Pure Appl. Geophys., 168(10), 1781-1798.

Kumar, S., Pal, S.K., Guha, A., Sahoo, S.D. and Mukherjee, A., 2020. New insights on Kimberlite emplacement around the Bundelkhand Craton using integrated satellite-based remote sensing, gravity, and magnetic data. Geocarto Int., 1-23.

Mallick, K., Vasanthi, A. and Sharma, K.K., 2012. Regional and residual gravity anomalies: The existing issues. In: Bouguer gravity regional and residual separation: Application to geology and environment. Springer-Verlag, Dordrecht. © Capital Publishing Company, 9-18.

Marjoribanks, R., 2010. Geological methods in mineral exploration and mining, second edition. London, New York, Springer Publishing Company.

Maus, S. and Dimri, V.P., 1996, Depth estimation from the scaling power spectrum of potential fields. Geophys. J. Int., 124, 113-120.

Mishra, D.C., 2011. Gravity and magnetic methods for geological studies (pp. 1-938). Hyderabad, India: BS Publications.

Mishra, D.C., Vijaya Kumar, V. and Rajasekhar, R.P., 2006. Analysis of airborne magnetic and gravity anomalies of peninsular shield, India integrated with seismic and magnetotelluric results and gravity anomalies of Madagascar, Sri Lanka and East Antarctica. Gondwana Res., 10, 6-17.

Mishra, D.C., Kumar, M.R. and Arora, K., 2012. Long wavelength satellite gravity and geoid anomalies over Himalaya, and Tibet: lithospheric structures and seismotectonics of deep focus earthquakes of Hindu Kush-Pamir and Burmese arc. J. Asian Earth Sci., 48, 93-110.

Moon, J.C., Whateley, M.K.G. and Evans, A.M., 2006. Introduction to mineral exploration. 2nd Edition, Blackwell Publishing.

Nabighian, M.N., 1972. The analytical signal of two-dimensional magnetic bodies with polygonal cross-section properties and use for automated anomaly interpretation. Geophysics, 37, 507-517.

Nabighian, M.N., 1984. Toward a three-dimensional automatic interpretation of potential field data via generalized Hilbert transforms: Fundamental relations. Geophysics, 49, 780-786.

Naganjaneyulu, K. and Santosh, M., 2010. The Cambrian collisional suture of Gondwana in southern India: A geophysical appraisal. J. Geodynamics, 50(3-4), 256-267.

Narayan, S., Sahoo, S.D., Pal, S.K., Kumar, U., Pathak, V.K., Majumdar, T.J. and Chouhan, A., 2017. Delineation of structural features over a part of the Bay of Bengal using total and balanced horizontal derivative techniques. Geocarto Int., 32(1), 351-366.

Naskar, D.C., Majumdar, N., Ajay Kumar and Nikhil Kumar, 2020. Geophysical mapping in parts of Nuapada, Bolangir and Kalahandi districts of Odisha (India). J. Ind. Geophys. Union, 24(3), 10-24.

Naskar, D.C., Nagaraja, P.N., Purushotham Suru and Raja Babu, 2021. Geophysical studies in parts of Kolar, Dharmapuri, Chittoor and Thiruvannamalai districts, Karnataka and Tamilnadu. J. Ind. Geophys. Union, 25(4), 25-40.

Naskar, D.C., Chandrasekhar, S.V.N., Anshika Sharma and Purushottam, M., 2022a. Regional gravity and magnetic surveys in parts of Belgaum, Bijapur, Dharwar and Raichur districts, Karnataka (India). J. Ind. Geophys. Union, 26(1), 23-40.

Naskar, D.C., Nagaraja, P.N., Ramesh, M. and Suru, P., 2022b. Gravity and magnetic studies in parts of Odisha and Chhattisgarh (India): implications in regional geology. Bulletin Geophys. Oceanography, 63(2), 289-310.

Negi, J.G., Agrawal, P.K., Singh, A.P. and Pandey, O.P., 1992. Bombay gravity high and eruption of Deccan flood basalts (India) from a shallow secondary plume. Tectonophysics, 206(3-4), 341-350.

Otsu, N., 1979. A threshold selection method from gray-level histograms. IEEE Transactions on Systems, 9(1), 62-66.

Pal, S.K. and Majumdar, T.J., 2015. Geological appraisal over the Singhbhum-Orissa Craton, India using GOCE, EIGEN6-C2 and in-situ gravity data. Int. J. Appl. Earth Observations and Geoinformation, 35, 96-119.

Pal, S.K. and Kumar, S., 2019. Subsurface structural mapping using EIGEN6C4 data over Bundelkhand craton and surroundings: An appraisal on kimberlite/lamproite emplacement. J. Geol. Soc, India, 94(2), 188-196.

Pal, S.K., Majumdar, T.J., Pathak, V.K., Narayan, S., Kumar, U. and Goswami, O.P., 2016. Utilization of high resolution EGM2008 gravity data for geological exploration over the Singhbhum-Orissa Craton, India. Geocarto Int., 31(7), 783-802.

Pandey, O.P., 2020. Geodynamic evolution of the Indian shield. Springer Nature, Switzerland, 349pp.

Peli, T. and Malah, D., 1982. A study of edge detection algorithms. Comput. Graphics Image Process., 20, 1-21.

Prewitt, J.M.S. and Mendelsohn, M.L., 1966. The analysis of cell images. Ann. Newyork Academy Sci., 128, 1035-1053.

Pun, T., 1980. A new method for gray level picture thresholding using the entropy of the histogram. Signal Processing, 2, 223.

Ramakrishnan, M. and Vaidyanadhan, R., 2008. Geology of India. Geological Society of India, 1 & 2, p. 994.

Rao, D.V.S., 1996. Resolving Bouguer anomalies in continents – A new approach. Geophys. Res. Lett., 23(24), 3543-3546.

Rao, V.V. and Prasad, B.R., 2006. Structure and evolution of the Cauvery Shear Zone system, Southern Granulite Terrain, India: Evidence from deep seismic and other geophysical studies. Gondwana Res., 10(1-2), 29-40.

Rao, V.V., Sain, K., Reddy, P.R. and Mooney, W.D., 2006. Crustal structure and tectonics of the northern part of the Southern Granulite Terrane, India. Earth Planet. Sci. Lett., 251(1-2), 90-103.

Reid, A.B. and Thurston, J.B., 2014. The structural index in gravity and magnetic interpretation: Errors, uses, and abuses. Geophysics, 79(4), 1JA-Z105.

Reid, A.B., Allsop, J.M., Granser, H., Millett, A.J. and Somerton, I.W., 1990. Magnetic interpretation in three dimensions using Euler deconvolution. Geophysics, 55, 80-91.

Sahoo, S.D. and Pal, S.K., 2019. Mapping of structural lineaments and fracture zones around the Central Indian Ridge (10°S-21°S) using EIGEN 6C4 Bouguer gravity data. J. Geol. Soc. India, 94(4), 359-366.

Saitoh, Y., Tsunogae, T., Santosh, M., Chetty, T.R.K. and Horie, K., 2011. Neoarchean high-pressure metamorphism from the northern margin of the Palghat-Cauvery Suture Zone, southern India: Petrology and zircon SHRIMP geochronology. J. Asian Earth Sci., 42(3), 268-285.

Sharma, P.V., 1986. A geophysical method in geology. Second Edition, Elsevier Science Publishing Co. Inc., 1-442.

Singh, A.P., Mishra, D.C., Kumar, V.V. and Rao, M.B.S.V., 2003. Gravity and magnetic signatures and crustal architecture along Kuppam-Palani geotransect, south India. Mem. Geol. Soc. India, 50, 139-164.

Singh, A.P., Kumar, N. and Singh, B., 2006. Nature of the crust along Kuppam-Palani geotransect (South India) from Gravity studies: Implications for Precambrian continental collision and delamination. Gondwana Res., 10(1-2), 41-47.

Spector, A. and Grant, F.S., 1970. Statistical models for interpreting aeromagnetic data. Geophysics, 35, 293-302.

Sun, G., Liu, Q., Ji, C. and Li, X., 2007. A novel approach for edge detection based on the theory of universal gravity. Pattern Recognition, 40, 2766-2775.

Telford, W.M., Geldart, L.P. and Sheriff, R.E., 2001. Applied Geophysics (Second Edition). Cambridge University Press, United Kingdom, p. 860.

Telford, W.M., Geldart, L.P., Sheriff, R.E. and Keys, D.A., 1976. Applied Geophysics. Cambridge University Press.

Tsai, W., 1985. Moment preserving thresholding: A new approach. Comput. Vision Graphics Image Processing, 29, 377-393.

Yellappa, T. and Rao, J.M., 2018. Geochemical characteristics of Proterozoic granite magmatism from Southern Granulite Terrain, India: Implications for Gondwana. J. Earth Syst. Sci., 127(2), 22.

Received on: 17-01-2024 ; Revised on: 12-09-2024; Accepted on: 14-09-2024

J. Ind. Geophys. Union, 28(5) (2024), 371-384

Morphometric analysis of the Jalleru Vagu sub-basin of Yerrakalva River, Eluru district, Andhra Pradesh (India), using geo-spatial technology

Ch Ashok Kumar[1], S. Siddi Raju[2*] and V. Gope Naik[1]

[1]Department of Geology, S. V. University, Tirupati-517502, Andhra Pradesh, India
[2] Department of Geology, Indira Gandhi National Tribal university, Amarkantak-484887, Madhya Pradesh, India
*Corresponding author: ssiddiraju@gmail.com

ABSTRACT

Morphometric analysis is a valuable approach for studying groundwater reservoirs by systematically evaluating the diverse topographical features and intricate drainage networks within a specific basin. In this study, we categorized the extracted drainage framework using Strahler's scheme, revealing a dendritic to sub-dendritic drainage pattern within the 312 km^2 Jalleru vagu sub-basin, which is an integral part of the Yerrakaluva River system. High-resolution satellite imagery IRS Sat-2 - LISS IV, P – 102 / R - 60, 61 acquired from 20th March, 2023 was used to analyze linear, areal, and relief aspects. The Jalleru vagu sub-basin, which is a fifth-order basin, is primarily characterized by lower-order streams, with a mean drainage density of 1.17 km/km^2. The highest slope in the basin is 590 m, primarily due to regional geology and cycles of erosion. The basin is elongated, with steep inclines, and modest elevation variations (elongation ratio: 0.30). A high drainage texture value increases the risk of soil erosion, which according to the drainage texture analysis, comes to 4.15. The study demarcates low to medium flood and erosion prone zones, Overall, the study area is elongated with less structural control and low to medium flood and erosional potentials. However, owing to low to medium flood and erosional susceptibility, and high groundwater withdrawals, water harvesting structures like check dams, levees, percolation tanks, rock dam are recommended for replenishment of groundwater resources.

Keywords: Morphometric analysis, Jalleru vagu sub-basin, Geospatial technique, Groundwater reservoirs, Drainage network.

INTRODUCTION

Morphometry refers to measuring and analysing the shape, dimensions, and configuration of the earth's surface and landforms. Its main objective is to facilitate the description of particular relief features, like valleys, slopes, and erosion surfaces, as well as the relief's general characteristics. Since the concentrated flow of water only takes up a small percentage of the broader trough, it is primarily responsible for the development of valleys. The shape and characteristics of valleys are directly or indirectly influenced by the streams' activities at the trough's base. The stream determines the base level for valley formation through its erosion work. Topography development requires understanding river reactions to climatic, lithologic, and tectonic environments. A number of river-specific geomorphometric indices have been created to explain the stages at which landforms emerge. River longitudinal profiles, for example, are a promising way to understand the stages of drainage basin evolution (Gardner, 1983; Howard et al., 1994; Hurtrez et al., 1999; Whipple and Tucker, 1999; Kirby and Whipple, 2001; Ouimet et al., 2009; Vijith et al., 2015), because they provide details on the primary mechanism of the bedrock incision (Wobus et al., 2006; Kirby and Whipple, 2012). The basis for almost all studies on watersheds and fluvial systems is the drainage basin. A catchment or watershed, or singular drainage basin, is a constrained area where runoff is routed through a single exit. A drainage basin is essentially an area that funnels all runoff toward a stream's mouth. On a topographic map, drainage basins can be located by tracing their boundaries or drainage divides Drainage basins are distinct landforms that may be statistically, comparatively, and analytically analyzed. Therefore, several numerical and qualitative descriptions have been given.

Morphometric characteristics are an analytical and quantitative assessment of the earth's surface structure, encompassing the sizes and shapes of its landforms. A stretch of land where rainfall collects and flows to a common location, is called a watershed. Research on watersheds is essential for preventing soil erosion, conserving water, and ensuring sustainable development. Remote sensing and geographic information systems (GIS) are useful tools for evaluating the hydraulic process of the river basin. A quantitative catchment report is provided by morphometric characteristics, which is useful for research on watershed priority, management of water resources, to control floods and soil erosion. In areas with steep slopes of the valley sides, the number of first-order streams are higher, resulting in an increased bifurcation ratio. Conversely, the bifurcation ratio decreases in the river basin's middle or downstream sections. This characteristic has an impact on the formation of valleys, leading to the presence of gullies and broad 'V' shaped valleys in the lower part of the basin.

Many studies have used morphometric analysis of drainage basins to assess the basins' groundwater potential and to identify suitable sites for the construction of check dams and artificial recharge structures (Sreedevi et al., 2005; Kumar et al., 2011; Mishra and Tiwari, 2011; Jasmin and Mallikarjuna, 2012; Tiwari and Srinivas, 2023). Watershed

prioritization based on morphometric features has also been carried out, assisting in mapping high flood potential and erosion-prone zones (Patton and Baker, 1976; Diakakis, 2010; Javed et al., 2011).

Several studies in India have utilized morphometric techniques to describe the geomorphology of drainage basins quantitatively (Kumari et al., 2021; Raju et al., 2023; Shekar et al., 2023; Mishra and Siddi Raju, 2024). In the realm of geomorphology, morphometry is defined by the scientific examination and estimation of the arrangement, shape, and measurements of the earth surface and its landforms. Morphometric analysis, can be used to comprehend various imbalances in rock hardness, ongoing catastrophic events, structural geomorphological changes, and the history of land infiltration within the basin (Rajasekhar et al., 2018, 2020).

Quantitative techniques have also been used in India to study the morphometric analysis of various drainage basins (Vittala et al., 2004; Chopra et al., 2005; Rudraiah et al., 2008; Altin and Altin, 2011; Buccolini et al., 2012; Pareta and Pareta, 2012). The fast-emerging spatial information technology, remote sensing, GIS, and GPS are more effective instruments for land and water resource planning and management than the traditional data processing methods (Rao et al., 2010; Etikala et al., 2019; Golla et al., 2020; Naresh Kumar et al., 2023). Hence, we adopt geospatial approach for morphometric analysis of Jalleru vagu sub-basin of the Yerrakalva River flowing through Eluru district, Andhra Pradesh, India for sustainable management.

STUDY AREA

The Jalleru vagu sub-basin lies in the northeastern part of Aliveru village, Buttayagudam Mandal, Eluru district in the Nagavaram mutta protected forest that drains into the Yerrakalva River before joining the Bay of Bengal. The geographical coordinates are 17°10' to 17°20' N and 81°10' to 81°25' E (**Figure 1**). The proposed study area encompasses an area of about 312 square kilometers with a perimeter of 82 km, falling within the Survey of India toposheets 65 G/3, 65 G/4, 65 G/7, and 65 G/8 (scale 1:50,000). This sub-basin is part of the Yerrakaluva River basin. The Jalleru vagu joins with the Yerrakaluva River at the downstream, which ultimately debouches into the Bay of Bengal. The average annual rainfall and temperature of the study area are 1054 mm and 31°C, respectively. The relief values range between 77 m to 590 m with a median of 84 m above the mean sea level (MSL).

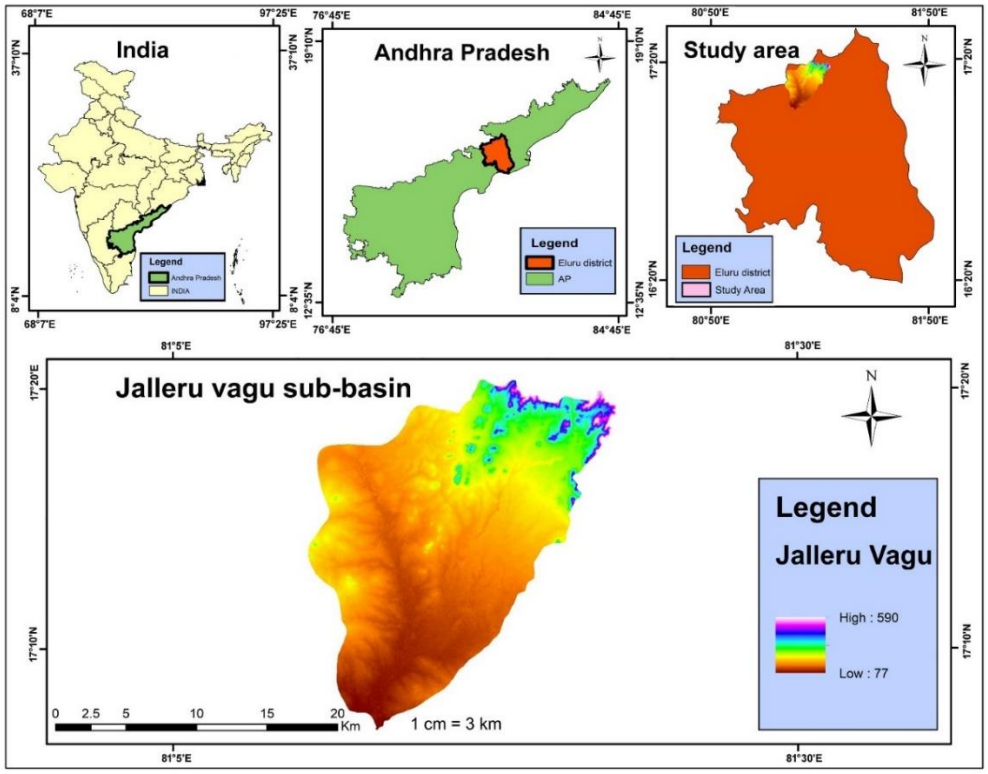

Figure 1. Location map of the Jalleru vagu sub-basin.

REGIONAL GEOLOGY

The geological formations of the Jalleru vagu sub-basin encompass a sequence ranging from the oldest Archeans to the upper Gondwana formations. The oldest rock variety is of the Archean age, associated with the Eastern Ghats Supergroup, exemplified by khondalite with patches of migmatite-gneiss, charnockite, and quartzite. The Barakar Formation (Raja Rao, 1982) belongs to lower Gondwana and comprises feldspathic sandstone occurring near the Beddadanur on the western margin of the Gondwana basin. The Kamthi Formation (King, 1881; Raiverman et al., 1985; Lakshminarayana and Murthi, 1990; Lakshminarayana et al., 1992; Rao, 1993; Ramamohan Rao et al., 1996, 1999; Burhanuddin, 2007; Mishra and Joshi, 2015) belongs to lower Gondwana and comprises ferruginous sandstone occurring in Jillelagudem village. Kota Formation (Sailaja et al., 2013) belongs to upper Gondwana and is represented by calcareous sandstone. The geological map of the study area is based on the Geological Survey of India (GSI, 1996) (Figure 2).

METHODOLOGY

Table 1 specifies the typical approaches for calculating the river basin's influential morphological qualities, whereas Figure 3 depicts the comprehensive process. The drainage network's morphometric study was conducted using two sources: SRTM-30 and SOI topographic maps (1:50,000 scale). A suite of GIS tools is used to extract the study area's drainage network from SRTM data (Figure 4). Two micro-basins are extracted. These micro-basins are referred to as Sangam vagu and Jalleru vagu. Morphometric parameters are computed for SRTM drainage and toposheet drainage in all micro-basins. SRTM data is intended for the creation of slope, hill shadow, and aspect maps. A quantitative analysis of the Jalleru vagu sub-basin has been executed to explore drainage characteristics employing the ArcGIS 10.7.1 software. Notable importance are the areal and linear characteristics, whose relationships with the following were studied: basin length, basin area, circularity ratio (Rc), elongation ratio (Re), drainage density (Dd), stream frequency (Fs), etc.

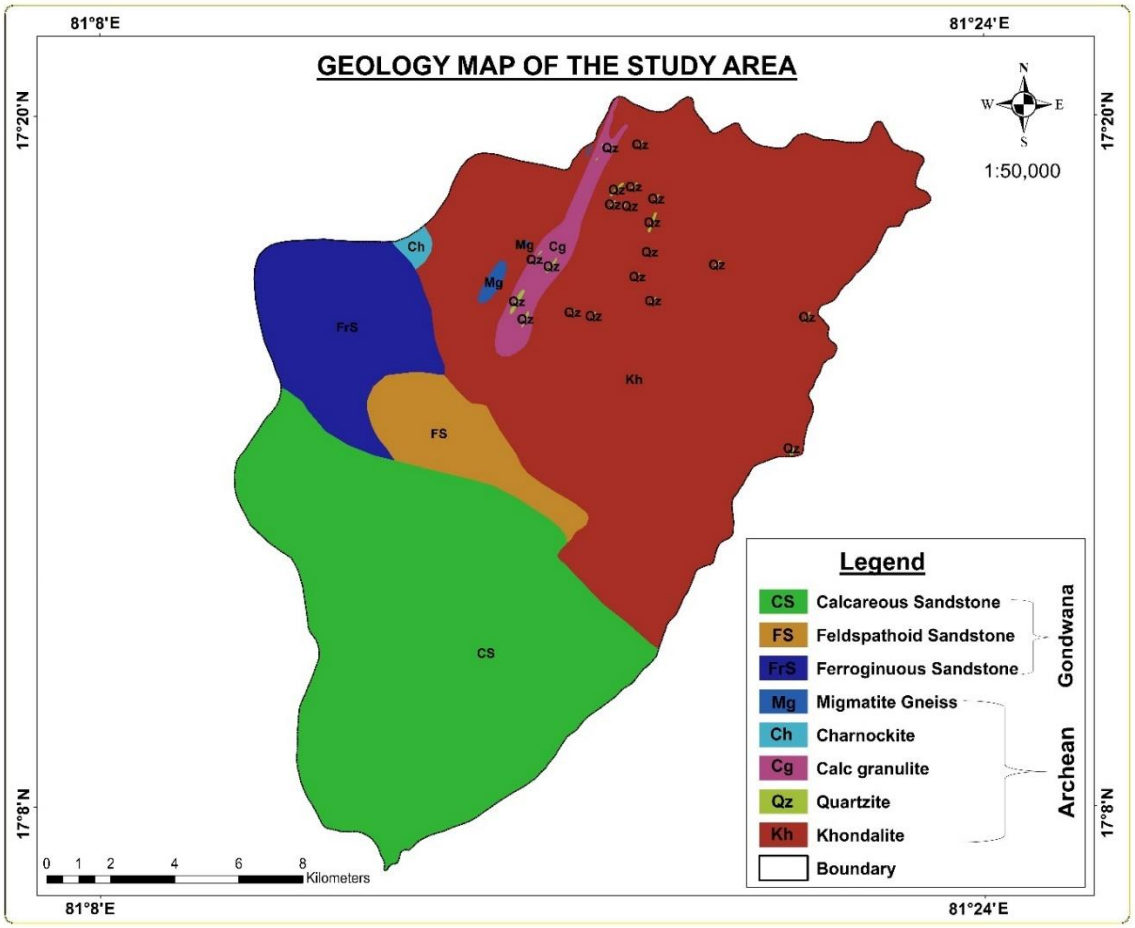

Figure 2. Geological map of the Jalleru vagu sub-basin (GSI, 1996)

Table 1. Details of morphometric parameters

S. No	Morphometric parameters	Symbol	Formula	References
Linear Aspects				
1	Watershed area (Km^2)	A	A	
2	Perimeter (Km)	P	P	Sreedevi et al. (2005)
3	Basin length (Km)	Lb	Lb	Sreedevi et al. (2005)
4	Strean order	U	u (Hierarchical Order)	Strahler (1964)
5	Stream number	Nu	Total no of stream segments of the order "u"	Strahler (1957)
6	Stream length	L	Length of the stream	
7	Mean stream length	Lsm	Lsm = Lu / Nu	Strahler (1964)
8	Stream length ratio	Rl	Rl = Lu / Lu - 1	Horton (1945)
9	Bifurcation ratio	Rb	Rb = Nu / Nu + 1	Schumm (1956)
10	Mean bifurcation ratio	Rbm	Average of the bifurcation ratios of all orders	Strahler (1964)
Areal Aspects				
11	Drainage density	Dd	Dd = Lu / A	Horton (1932)
12	Drainage texture	Rt	Rt = Nu / P	Smith (1950)
13	Stream frequency	Rs	Fs = Nu / A	Horton (1945)
14	Elongation ratio	Re	Re = 2/Lb x $(A/P)^{0.5}$	Schumm (1956)
15	Circularity ratio	Rc	Rc = 4 π A/P2	Strahler (1956)
16	Form factor	Ff	Ff = A/(Lb)2	Strahler (1956)
Relief Aspect				
17	Basin relief	Bh	Bh = Hmax - Hmin	Schumm (1956)
18	Relief ratio	Rh	Rh = Bh / Lb	Schumm (1956)
19	Ruggedness number	Rn	Rn = H/A x Dd	Melton (1965)
20	Slope			

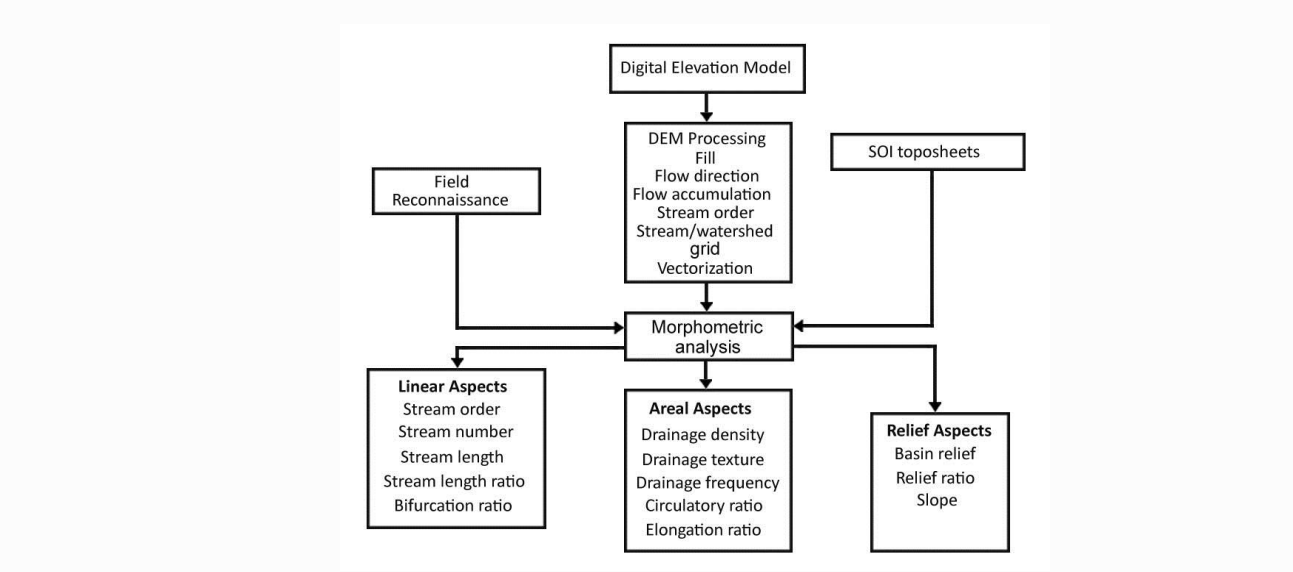

Figure 3. Aspects of morphometric Parameters.

RESULTS AND DISCUSSION

Area (A), perimeter (P) and basin length (Lb)

The total basin area estimated at Sangam vagu is 170.231 km^2 and Jalleru vagu is 140.308 km^2. The perimeter of Sangam vagu is 47.223 km and Jalleru vagu is 35.854 km (Table 2). Similarly, the greatest length of the basin is Sangam vagu i.e. 17.19 km and the lowest is Jalleru vagu i.e. 14.057 km (Table 2).

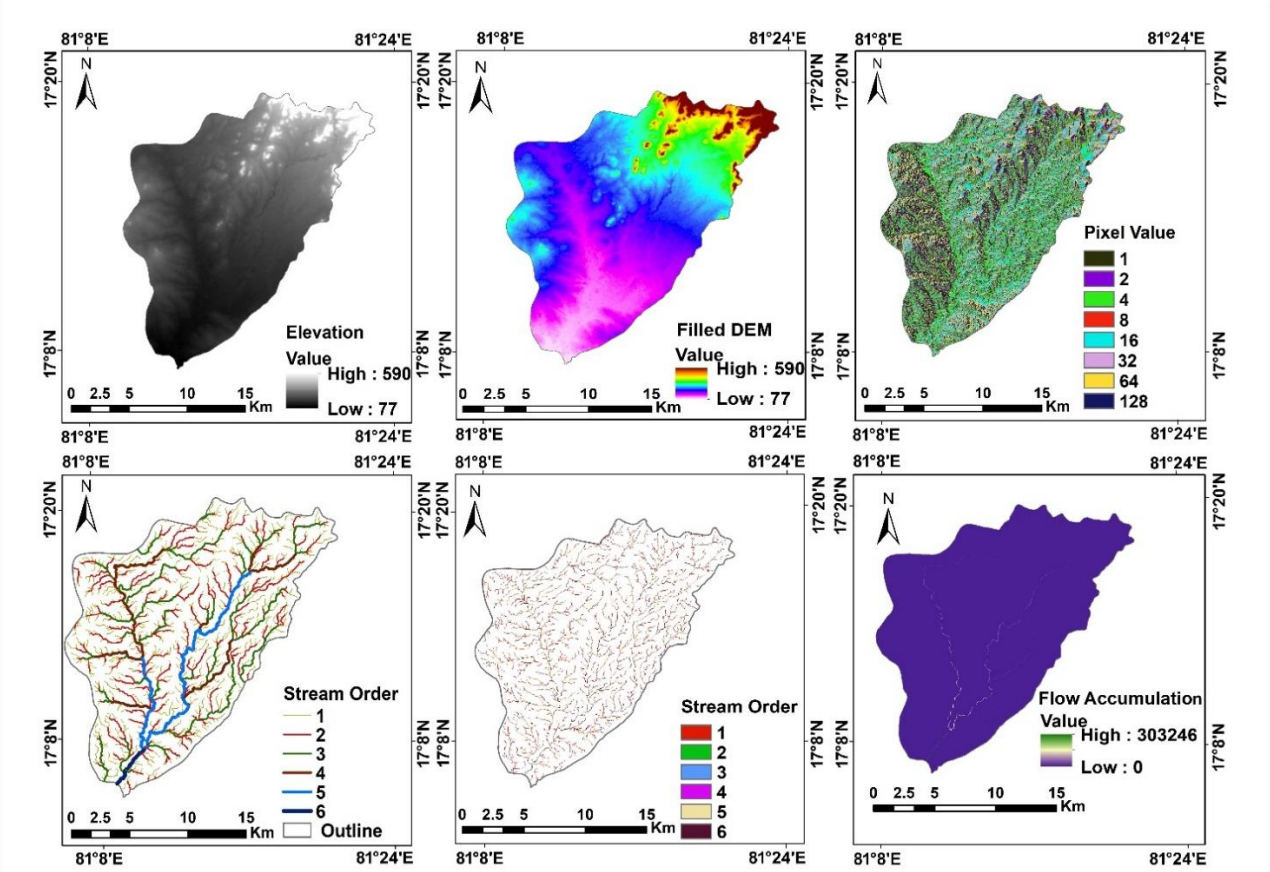

Figure 4. Automated extraction process of drainage network map of Jalleru vagu sub-basin.

Table 2. Length, area and perimeter of the Jalleru Vagu sub-basin.

Micro-Basins	Area (Km^2)	Perimeter(P) (km)	Length (km)
Sangam vagu	170.231	47.223	17.19
Jalleru vagu	140.308	35.854	14.057

Table 3. Drainage basin morphometry together with stream order and stream number.

Micro-basin	1^{st} order	2^{nd} order	3^{rd} order	4^{th} order	5^{th} order	Total
Sangam vagu	83	34	18	30	10	175
Jalleru vagu	80	42	17	27	--	166

Linear aspects

Stream Order (U)

The efficiency of drainage advancement is intertwined with the dimension of watercourses, thereby rendering stream order a pivotal metric in the linear facet of a drainage basin. Streams of the first order remain devoid of tributaries (Strahler, 1958). A section takes on the designation of third order when second-order channels converge. The confluence of two third-order sections culminates in the formation of a fourth-order channel, with this progression extending up to the fifth order (Strahler, 1964) (Figure 5). As a result, the Jaller vagu sub-basin has been assigned a fifth-order basin classification (Table 3). A higher number of streams in the I and II orders indicates continued topographical erosion, but fewer streams in the III and IV orders indicate a well-developed terrain surrounding the streams.

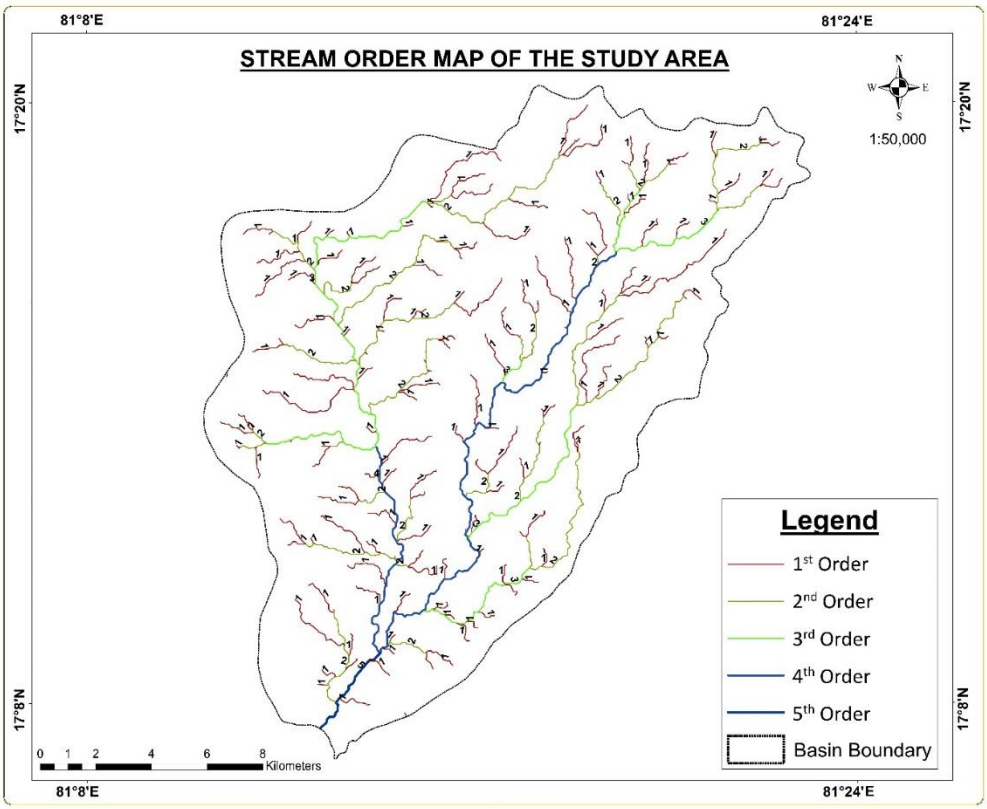

Figure 5. Stream order map of the Jalleru vagu sub-basin.

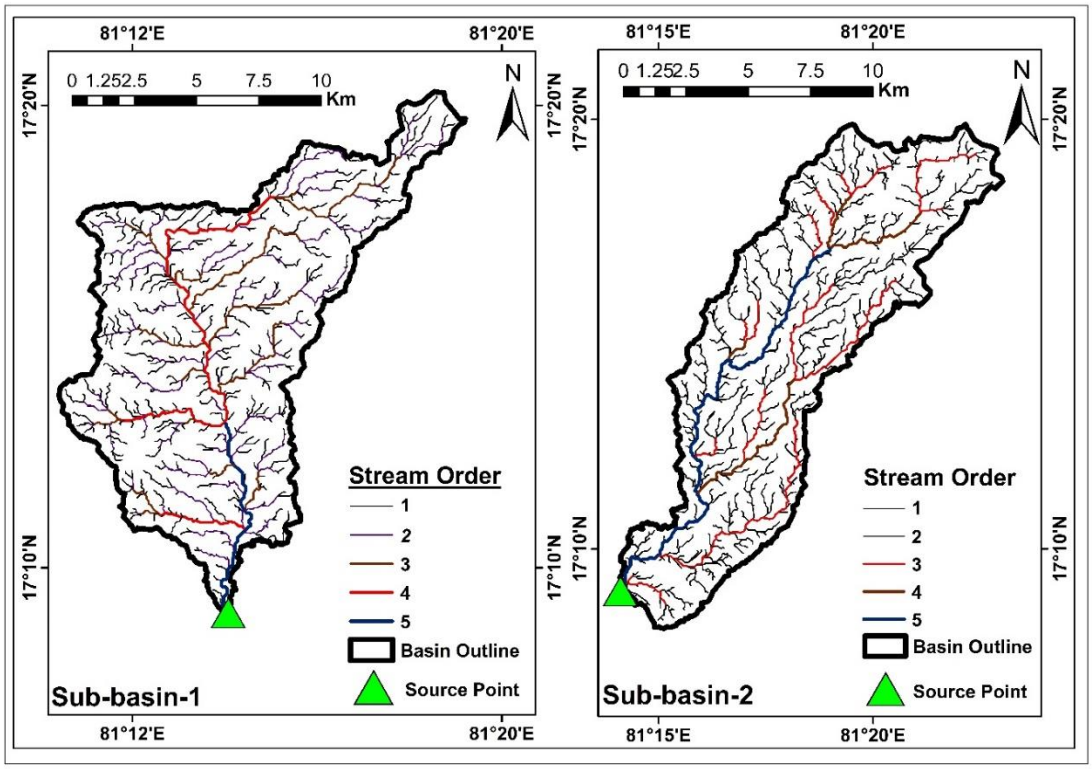

Figure 6. Micro-basins of the Jalleru vagu sub-basin.

Stream number (Nu)

Stream number (Nu) alludes to a hierarchical connection amongst individual segments coursing through a drainage arrangement. As the stream order escalates, the total number of streams, as well as their downward course, experiences a decrease (Rai et al., 2017). Within the study locality, an interconnected drainage framework prevails, characterized by uniform subsurface strata. This investigation introduced a proposed methodology for stream organization (Strahler, 1957; Das and Mukherjee, 2005). The delineation of streams encompassed the digitization process, drawing from topographic maps and satellite imagery sources. The Sangam vagu comprises 175 streams, with the highest fifth-order stream, and the Jalleru vagu has 166, with the highest fourth-order stream (Table 3). Figure 6 illustrates two micro-basins, namely Sangam Vagu and Jalleru Vagu.

Figures 7 and 8 depict a correlation plot of the number of stream orders in the Sangam vagu sub-basins on X-axis correlating to the stream number in the Y-axis. In a drainage basin, the number of streams decreases significantly as stream order increases. Here, the 5th order is the highest-ordered stream for the Sangam vagu, and the 4th is the highest order for the Jalleru vagu. The stream order (Strahler, 1964) observed that the number of stream segments of any given order is lower than that of the next higher order. It is also observed that normally, higher frequency is associated with a first-order stream. Fluctuation in stream order is observed due to the physiographic conditions. It is observed that areas that have undergone erosion generally have a larger number of streams than mature topography.

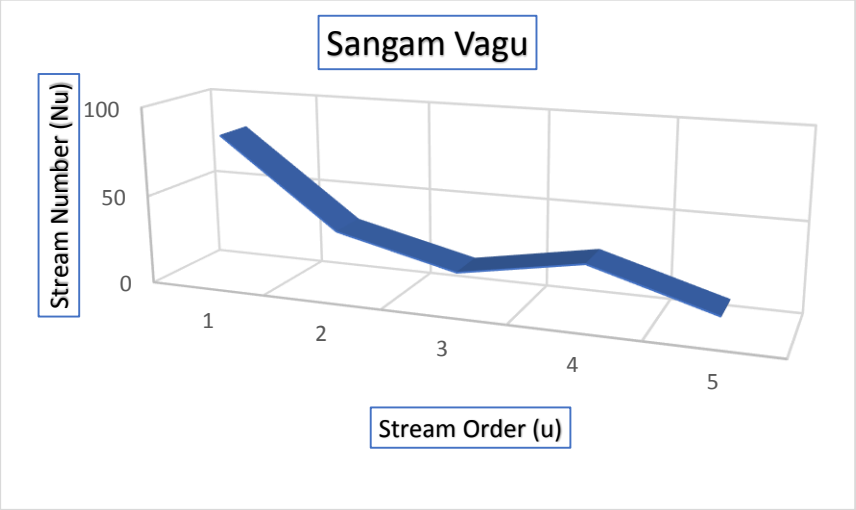

Figure 7. Stream order and stream number correlation in the Sangam vagu.

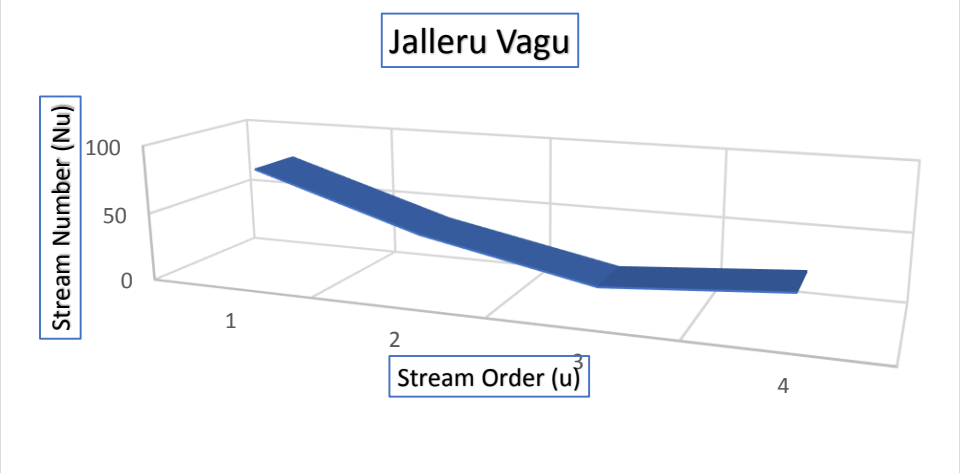

Figure 8. Stream order and stream number correlation of the Jalleru vagu.

Table 4. Drainage basin morphometry (stream length, mean stream length, and bifurcation ratio).

Micro-basins	1st order	2nd order	3rd order	4th order	5th order	Stream length km	Stream length ratio	Mean stream length	Bifurcation ratio
Sangam vagu	65.02	53.6	38.26	23.19	12.57	195.64	1.05	1.11	2.44
Jalleru vagu	62.51	45.6	34.93	28.04	--	171.12	1.06	1.21	1.91

Stream length (Lu)

The dimensions of the Stream length have been computed using the GIS-grounded arrangement recommended by Horton (1945). The total stream length value for Sangam vagu is 195.64 km and for Jalleru vagu, it is 171.12 km (Table 4). Consequently, it is noticeable that the extent of the primary category watercourse and the quantity of watercourses are distributed more effectively compared to other classifications. The initial order stream, constituting nearly half the watercourse length, experiences transitory flow during arid seasons and sustains a continuous flow during the rest of the year. Due to declining groundwater replenishment, the continuous span might diminish farther upstream and be briefer in dry seasons.

Mean stream length (Lsm)

Mean stream length is a fundamental attribute that pertains to the various elements of a drainage network and the corresponding basin surfaces (Strahler, 1964). It is calculated by dividing the number of streams in an order by the total length of streams in that order. Throughout the Jalleru vagu sub-basin basin, the mean stream length variation is 1.04. However, when the basin is divided into two micro-basins, Sangam vagu exhibits a mean stream length variation of 1.11, while Jalleru vagu shows a slightly higher variation of 1.21 (Table 4).

Stream length ratio (Rl)

The ratio of a higher order's overall stream length to the stream length of the stream fragment that is immediately below it is known as the stream length ratio. The overall stream length of a given order is exactly proportional to the stream number; that is, as the order of the stream fragment grows, the total stream length falls. There are erratic swings in the stream length ratio at the basin and sub-basin levels. Over the whole basin, the Jalleru vagu sub-basin's stream length ratios range from 1.05 to 1.06 (Table 4). Regarding the erosional stage and surface flow discharge of the basin, the stream length ratio is highly significant.

Bifurcation ratio (Rb) and mean bifurcation ratio (Rbm)

Horton (1945) and Strahler (1952) introduced the concept of bifurcation ratio, which refers to the ratio of the number of streams of one order to the number of streams of the next higher order. One dimensionless feature of a drainage basin is the bifurcation ratio (Rb). Numerous parameters, including drainage density, stream confluence angle, lithology, basin form, and basin area, are thought to have an impact. Different parts of the world's bifurcation ratio have been investigated by geomorphologist. In watersheds where geological structure does not significantly affect the drainage pattern, it is typically between 3.0 and 5.0 (Strahler, 1964). Theoretically, there is no upper bound on Rb and a minimum is 2.0. A fifth-order basin with a uniform bifurcation ratio for several orders is the Jalleru vagu. The bifurcation ratio (Rb) ranges between the whole Jalleru vagu sub-basin is 13.01, Sangam vagu 2.44 and Jalleru vagu 1.91 The mean bifurcation ratio (Rbm) is 3.25 (Table 4). Jalleru vagu sub-basin suggests that the area's geomorphology has a dominant control over structural control.

Areal aspects

Drainage density (Dd)

The term "drainage density" refers to measuring the amount of drainage progress in a basin. It reflects the closeness of channel intervals, which are explained by different erosion patterns between different layers, changes in elevation, and precipitation throughout the basin (Horton,1932). Smith (1950) and Strahler (1957) have categorized drainage compactness values below 5 as coarse, from 5 to 13.7 as intermediate, between 13.7 and 155.3 as refined, and surpassing 155.3 as exceedingly refined. Chow (1964), asserts that regions with highly penetrable subterranean constituents are inclined toward diminished drainage compactness. In line with Horton's methodology, the computed drainage compactness within the Jalleru vagu sub-basin is 1.17, Sangam vagu 0.269, and for Jalleru vagu 0.301 (Table 5). This implies low drainage compactness, indicative of permeable subsurface layers, abundant vegetation cover, and modest relief. Figure 9 shows drainage density and drainage texture of correlation bar graph.

Table 5. Drainage basin morphometry of the Jalleru vagu sub-basin.

Micro-basins	Drainage density (km)	Drainage texture (km)	Stream frequency (km)	Elongation ratio (R_e)	Circularity ratio (R_c)	Form factor (R_f)
Sangam vagu	0.269	0.350	0.072	0.353	0.130	0.098
Jalleru vagu	0.301	0.403	0.080	0.431	0.185	0.146

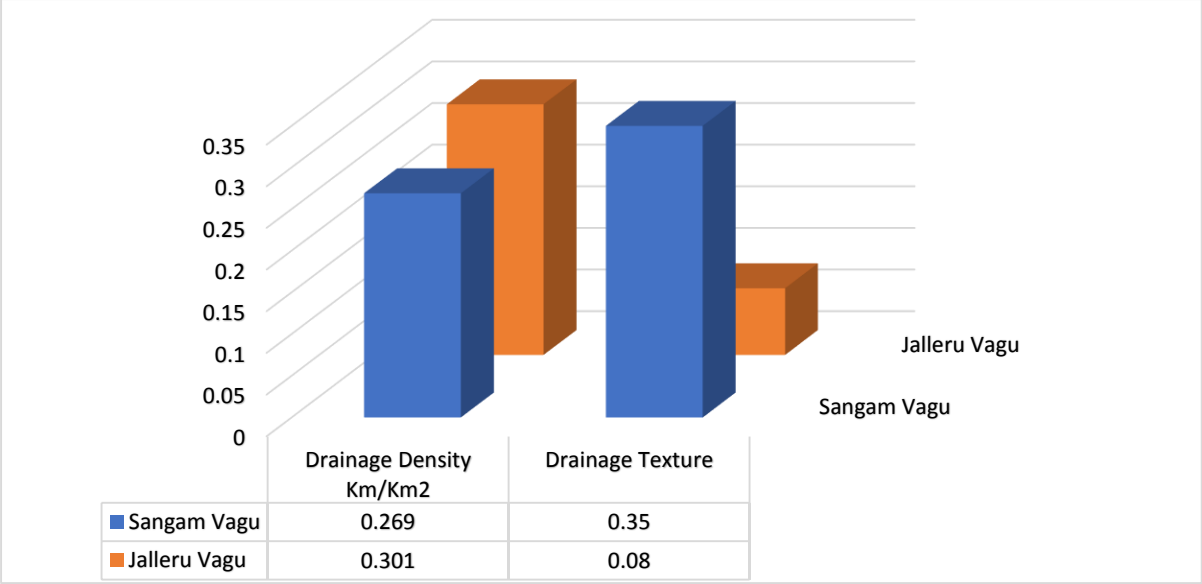

Figure 9. Drainage density and drainage texture correlation bar graph of the Jalleru vagu sub-basin

The Jalleru vagu sub-basin's correlation plot between drainage density and drainage texture is displayed in Figure 9. Fine drainage texture is indicated by a high drainage density value, and coarse grain drainage texture is suggested by a low drainage density value. A high drainage texture value in that particular basin raises the possibility of soil erosion (Strahler, 1964).

Stream frequency (Fs)

The quantity of stream frequency per given expanse is called watercourse prevalence. Horton introduced the term "stream frequency" in 1932. According to Melton (1965), a higher stream frequency value suggests reduced permeability and increased surface runoff, while fractures influence a lower stream frequency value. The stream frequency of the total study area is 1.09, Sangam vagu 0.072, and Jalleru vagu 0.080 (Table 5), showcasing a constructive relationship with the density of the drainage region.

Elongation ratio (Re)

The elongation ratio is the proportion amid the width of a circle possessing the equivalent expanse as the drainage basin and the utmost span of the basin (Schumm, 1956). Strahler (1964) asserts that the elongation ratio spans from 0.6 to 1 across various climatic and geological structures. Elongation ratio values proximate to 1 are observable in typical areas with exceedingly minimal elevation changes. In contrast, values ranging from 0.6 to 0.8 are generally linked with pronounced elevation disparities and steep inclines (Pakhmode et al., 2003). The elongation ratio value for total study area is 0.304, Sangam vagu, 0.353 and for Jalleru vagu, 0.431 (Table 5), which gives an idea about the more elongation in nature with a low relief environment.

Circularity ratio (Rc)

The circulatory ratio depends upon the length and frequency of streams, land use, land cover, the slope of the basin, and geologic units (Patel et al., 2013). An understanding of the many phases of a basin's evolution can be gained from the circulatory ratio's value, which ranges from low to high, indicating the young stages of the basin's evolution. As shown in Table 5, the calculated numerical values of the circularity ratio for the entire research region are 0.30 and 0.130 for the Sangam vagu, and 0.185 for the Jalleru vagu, indicating a significantly more elongated nature. The ratio

of roundness points toward the initial stages of advancement in the terrain.

Form factor (Ff)

The ratio of basin area to basin length squared is known as the form factor. The quantity representing the basin's influencing factor on its discharge is dimensionless. Ff can be defined as the ratio of the area of a basin and the square of the basin length (Sreedevi et al., 2005). The length of time it takes to pass through the outflow is greater for an extended basin than for a circular basin. The form factor of Sangam vagu 0.098 and Jalleru vagu 0.146 which means it is circular (Table 5).

Relief aspect

Basin relief (Bh)

The difference in elevation between the highest and lowest points in a basin is known as basin relief (Bh). According to Burrough et al. (2015), the parameter 'Bh' controls the stream order gradient, which affects flood patterns, the amount of transported material, and the characteristics of landforms and geomorphic activity. It includes information on the amounts of kinetic and potential energy that are expressed in runoff from surface water, precipitation, and flooding in the basin. The basin relief value for Sangam vagu is 340 m and Jalleru vagu 590 m, indicating medium to high flooding (Table 6).

Relief ratio (Rh)

The utmost elevation variation over the horizontal span along the lengthiest measurement of the basin, delineated along the primary watercourse route, is identified as a relief ratio (Rh) (Schumm, 1956). The Rh embodies a comprehensive gradient encompassing the catchment area and acts as an indicator of the erosion mechanism's potency on the basin's operational incline (Schumm, 1956). Elevated Rh values correlate with rugged topography, while reduced Rh values correspond with a relatively level plateau or a valley setting (Maathuis and Wang, 2006). Grasping the arrangement of slopes holds fundamental significance, as it provides insights into urban planning, agricultural potential, afforestation prospects, and blueprints for engineering projects. The relief ratio of the study area is 5.34 for Sangam vagu and 6.99 for Jalleru vagu sub-basins (Table 6).

Ruggedness number (Rn)

The ruggedness number is defined as the product of drainage density and basin relief/total relief (Strahler, 1956). It also shows the structural complexity of the terrain. The low relief ratio value and ruggedness number of particular basins give an idea about the existence of groundwater zones. Higher Rn values indicate steeper and more dissected terrain, suggesting a higher potential for soil erosion and rapid runoff. Lower Rn values indicate gentler slopes and less dissection, suggesting lower erosion potential and slower runoff. Hence, the value of ruggedness number is very low of 0.220 for Sangam vagu and 0.229 for Jalleru vagu is (Table 6), indicating gentler slopes and less dissection, suggesting lower erosion potential and entrapment of flooded water.

Slope

It is crucial for terrain analysis to comprehend the natural processes in topography, geology, soils, hydrogeology, infrastructure development, and hazard management both at the surface and below, reliable estimation of the stability of slopes and foundations is however extremely difficult. Knowledge of slope is essential to grassroots decentralized planning.

The slope, which can be expressed in either degrees or percentages, is used to quantify changes in surface values over a given distance. A raster formatted digital elevation model (DEM) is a grid with values assigned to each cell based on a shared reference point. By computing the slope, we may determine the values of the greatest difference and slope. The results from mapping are utilized to generate a biased neighbourhood usage map using ArcGIS 10.7.1 spatial analyst tools. The western region has a higher elevation (590 m) and north-western region has the lowest elevation (77 m) from the mean sea level which causes more outflow and less opportunity for precipitation infiltration. The research area map is categorized as follows using tilt as a dividing factor: 1-3° (gentle), 3-5° (moderate), 5-10° (steep), 10-35° (very steep), and >35° (especially steep). A large section of the Jalleru vagu sub-basin area is seen to have mildly sloping terrain, suggesting that the area's topography is primarily flat (Figure 10). Gentle slopes are considered favourable for groundwater control due to their flat terrain.

Table 6. Drainage basin morphometry.

Micro-basins	Maximum relief	Minimum relief	Relief ratio	Ruggedness number (Rn)
Sangam vagu	340	77	5.34	0.220
Jalleru vagu	590	92	6.99	0.229

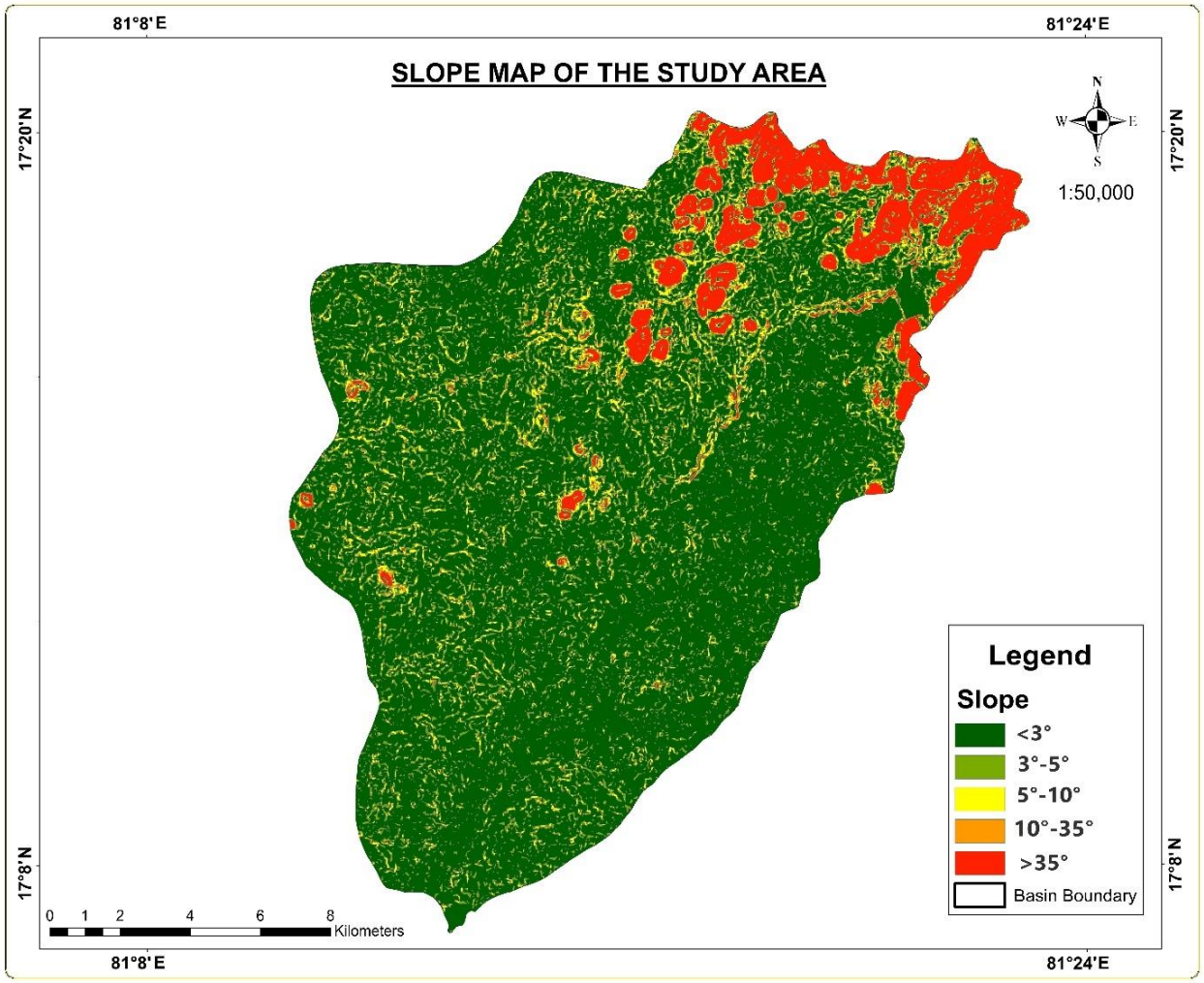

Figure 10. Slope map of the study area.

Moderate slopes fall within an accurate range as they contribute to partial runoff. Steep slopes, characterized by excessive surface runoff and minimal infiltration, are categorized under precise areas for dam construction and similar purposes.

CONCLUSIONS

The morphometric analysis of the study area, namely Sangam vagu and Jalleru vagu, were carried out by combining geographic information systems (GIS) and remote sensing (RS) methods, which has enabled to precisely measure and analyze the morphometric characteristics by providing insight into the linear, areal and relief aspects. The overall number of streams decreases with increasing stream order, suggesting a more hierarchical and ordered drainage network. Moreover, the study area implies low drainage compactness, which is indicative of permeable subsurface layers. Sangam vagu exhibited an elongation ratio of 0.353, while Jalleru vagu had 0.431, indicating a more elongated nature with low relief, which suggests that the drainage has to travel a wide range of distance to reach the basin outlet and is less prone to sediment erosion and floods. Moreover, the basin relief value for Sangam vagu is 340 m and Jalleru vagu is 590 m, indicating low to medium flooding. The circular ratio values of Sangam vagu (0.130) and Jaleeru vagu (0.185) indicate short lag times and a more elongated stream. Stream length and mean stream length parameters are crucial for understanding drainage network and basin characteristics. Overall, the streams (Jalleru and Sangam vagu) have relief, that are more elongated, and are in the initial stage of evolution. Moreover, it has less structural control less sediment erosional capacity, and low to medium flooding frequency. However, due to its low to medium flood and low erosional susceptibility, and critical groundwater extracts in recent times, water replenishing structures like check dams, levees, percolation tanks, and rock dams are recommended for sustainable development of Jalleru Vagu sub-basin, Andhra Pradesh, India.

Acknowledgements

The authors wish to thank the reviewers for their invaluable feedback and the Department of Geology, Indira Gandhi National Tribal University, India, for providing access to the Remote Sensing and GIS laboratory.

Author Credit Statement

Collection of the data (SRTM DEM, SOI toposheets, IRS Sat-2 - LISS IV) preparation of the maps and calculation of the morphometric parameters were done by Ch. Ashok Kumar. Drafting of the manuscript, software resources and figures were done by V. Gope Naik. Referencing and submission of the Manuscript was done by S Siddi Raju. All authors read and approved the final manuscript.

Data Availability

Data used in this manuscript is sourced from the global climate database (https://globalweather.tamu.edu), hydrological data from https://indiawris.gov.inwris and Digital Elevation Model (DEM) from https://www.usgs.gov/centers/eros/science/usgs-eros-archive-digital-elevation-shuttle-radar-topography-mission-srtm-1-arc

Compliance with Ethical Standards

The authors declare that they have no conflict of interest and adhere to copy right norms

REFERENCES

Altin, T. B. and Altin, B. N., 2011. Development and morphometry of drainage network in volcanic terrain, Central Anatolia, Turkey. Geomorphology, 125, 485-503.

Buccolini, M., Coco, L., Cappadonia, C. and Rotigliano, E., 2012. Relationships between a new slope morphometric index and calanchi erosion in northern Sicily, Italy. Geomorphology, 149-150, 41-48.

Burhanuddin. M., 2007. Textural analysis in interpreting the depositional environmental of Lower Gondwana sandstones in central part of Godavari basin, Andhra Pradesh. J. Geol. Soc. India, 69, 1335-1341.

Burrough, P. A., McDonnell, R. A. and Lloyd, C. D., 2015. Principles of Geographical Information Systems. Oxford University Press, Oxfrod.

Chopra, R., Dhiman, R. D. and Sharma, P. K., 2005. Morphometric analysis of sub-watersheds in Gurdaspur district, Punjab using remote sensing and GIS techniques. J Indian Soc. Remote Sens., 33, 531-539.

Chow, V. T., 1964. Handbook of hydrology. McGraw-Hill Book Co. Inc, New York.

Das, A. K. and Mukherjee, S., 2005. Morphometry using satellite data and GIS in Raigad district, Maharashtra. J. Geol. Soc. India, 65, 577-586.

Diakakis, M., 2010. A method for flood hazard mapping based on basin morphometry: application in two catchments in Greece. Nat. Hazards, *56*(3), 803-814.

Etikala, B., Golla, V., Li, P. and Renati, S., 2019. Deciphering groundwater potential zones using MIF technique and GIS: A study from Tirupati area, Chittoor District, Andhra Pradesh, India. Hydro. Res., 1, 1–7.

Gardner, T. W., 1983. Experimental study of knick point and longitudinal profile evolution in cohesive, homogeneous material. Geol. Soc. Am. Bull., 94(5), 664-672.

Golla, V., Etikala, B., Veeranjaneyulu, A., Subbarao, M., Surekha, A. and Narasimhlu, K., 2018. Data sets on delineation of groundwater potential zones identified by geospatial tool in Gudur area, Nellore district, Andhra Pradesh, India. Data in Brief, 20, 1984–1991.

GSI, 1996. District Resource map, West Godavari District, Andhra Pradesh.

Horton, R. E., 1932. Drainage basin characteristics. Trans. Am. Geophys. Un., 13, 350-370.

Horton, R. E., 1945. Erosional development of streams and their drainage basins; hydro physical approach to quantitative morphology. Bull. Geol. Soc. Am., 56. 275-370.

Howard, A. D., Dietrich, W. E and Seidl, M. A., 1994. Modeling fluvial erosion on regional to continental scales. J. Geophys. Res., Solid, 99(B7),13971-13986.

Hurtrez, J., Sol, C. and Lucazeau, F., 1999. Effect of drainage area on hypsometry from an analysis of small□scale drainage basins in the Siwalik Hills (Central Nepal). Earth Surf. Process Landforms, 24(9), 799-808.

Jasmin, I. and Mallikarjuna, P., 2012. Morphometric analysis of Araniar river basin using remote sensing and geographical information system in the assessment of groundwater potential. Arab. J. Geosci., 6(10), 3683-3692.

Javed, A., Khanday, M. Y. and Rais, S., 2011. Watershed prioritization using morphometric and land use/land cover parameters: A remote sensing and GIS based approach. J. Geol. Soc. India, 78, 63-75.

King, W., 1881: Geology of the Pranhita-Godavari Valley. Mem. Geol. Surv. India, 19, 158-311.

Kirby, E. and Whipple, K., 2001. Quantifying differential rock-uplift rates via stream profile analysis. Geology, 29(5), 415-418.

Kirby, E., and Whipple, K., 2012. Expression of Active Tectonics in Erosional Landscapes. J. Structural Geol., 44, 54-75.

Kumar, A., Jayappa, K. S. and Deepika, B., 2011. Prioritization of sub-basins based on geomorphology and morphometric analysis using remote sensing and geographic information system (GIS) techniques. Geocarto. Int., 26(7), 569-592.

Kumari, P., Kumari, R. and Kumar, D., 2021. Geospatial approach to evaluate the morphometry of Sabarmati River Basin, India. Arab. J. Geosci., 14, Article 206.

Laksminarayana. G. and Murti. K. S., 1990. Stratigraphy of the Gondwana Formations in the Chintalapudi sub-basin, Godavari Valley, Andhra Pradesh. J. Geol. Soc. India, 36, 13–35.

Lakshminarayana. G., Murti, K. S. and Rama Rao, M., 1992. Stratigraphy of the Upper Gondwana sediments in the Krishna-Godavari coastal tract, Andhra Pradesh. J. Geol. Soc. India, 36, 13-27.

Maathuis, B. H. P. and Wang, L., 2006. Digital Elevation Model based hydro-processing. Geocarto. Int., 21(1), 21-26.

Melton, M. A., 1965. The Geomorphic and Palaeo climatic Significance of Alluvial Deposits in Southern Arizona. J. Geol., 73, 1-38.

Miller, V.C., 1953. Technical report. Quantitative Geomorphic Study of Drainage Basin Characteristics in the Clinch Mountain Area, Virginia, and Tennessee, Vol. 3. Department of Geology, Columbia University..

Mishra, A. and Tiwari, R. N., 2011. Morphometric analysis of tons basin, Rewa District, Madhya Pradesh, based on watershed approach. Earth Sci. India, 4(3), 171-180.

Mishra, S. and Joshi, H., 2015. Palyno biostratigraphy and Floral Biodiversity of Late Permian Sediments from Godavari Graben, Andhra Pradesh. Int. J. Geol, Earth & Env. Sci., 5(3), 43-54.

Mishra, S. and Siddi Raju, S., 2024. Morphological and hydrological analysis of Kantamal sub-basin of the Mahanadi River Odisha (India), using QSWAT model. J. Indian Geophys. Union, 28(3), 194-206

Naresh Kumar, D., Venkateswara Rao, T., Veerla, V. K., Etikala, B., Mohana Prasada Rao, Y. and Jujjuvarapu, A. 2023. Systematic Approach of Groundwater Resources Assessment Using Remote Sensing and Multi-influence Factor (MIF) Techniques in Medchal Mandal, Telangana State, India. In: Balaji, E., Veeraswamy, G., Mannala, P., Madhav, S. (eds) Emerging Technologies for Water Supply, Conservation and Management. Springer Water. Springer, Cham, 1, 1-384

Ouimet, W. B., Whipple, K. X. and Granger, D. E., 2009. Beyond threshold hillslopes: Channel adjustment to base-level fall in tectonically active mountain ranges. Geology, 37(7), 579-582.

Pakhmode, V., Kulkarni, H. and Deolankar, S. B., 2003, Hydrological – drainage analysis in Watershed-program planning: a case from the Deccan basalt, India. Hydrogeol. J, 11(5), 595-604.

Pareta, K. and Pareta, U., 2012. Quantitative geomorphological analysis of a watershed of Ravi River Basin, H.P. India. Int. J. Remote Sens, & GIS, 1, 41-56.

Patel, D. P., Gajjar, C. A. and Srivastava, P.K., 2013. Prioritization of Malesari mini-watersheds through morphometric analysis: a remote sensing and GIS perspective. Environ. Earth Sci., 69 (8), 2643-2656.

Patton, P. C. and Baker, V. R., 1976. Morphometry and floods in small drainage basins subject to diverse hydrogeomorphic controls. Water Resour. Res., 12, 941-952.

Rai, P. K., Mishra, V. N. and Mohan, K., 2017. A study of morphometric evaluation of the Son basin, India using geospatial approach. Remote Sens. Appl. Soc. Environ., 7, 9-20.

Raiverman, V., Rao, M. R. and Pal, D., 1985. Stratigraphy and structure of Pranhita-Godavari graben. Petrol. Asia J., 8(2), 174-290.

Raja Rao, C. S., 1982. Coal Resources of Tamilnadu, Andhra Pradesh, Orissa and Maharashtra, Bull. U.S. Geol. Surv India, 45, 41-52.

Rajasekhar, M., Raju, G. S., Raju, R. S., Ramachandra, M. and Kumar, B.P., 2018. Data on comparative studies of lineaments extraction from STER DEM, SRTM, and Cartosat for Jilledubanderu River basin, Anantapur district, India by using remote sensing and GIS. Data in brief, 20, 1676-1682.

Rajasekhar, M., Gandhiraju, S. R., Kadam, A. and Bhagat, V., 2020. Identification of groundwater recharge–based potential rainwater harvesting sites for sustainable development of a semiarid region of southern India using geospatial, AHP, and SCS – CN approach. Arab. J. Geosci., 23 (2), 24.

Raju, R. S., Raju, G. S. and Rajasekhar, M. A., 2023. Study on hydro-geological characterization through Dar-Zarrouk parameters in hard rock terrain of Mandavi River Basin, Andhra Pradesh, India. Arab. J. Geosci., 16, 453.

Ramamohana Rao, T., Venkateswara Rao. Y., Prasad, G. J. S. and Tirumala Rao, P., 1996. Tectonics of Chintalapudi and the adjoining sub-basins of Gondwanas of Godavari Valley and the east coast of India. Proceedings of IX International Gondwana Symposium, Oxford IBH, New Delhi, 755-781.

Ramamohana Rao, T. Siaram, K. and Rao, Y. V., 1999. Sedimentological and Geochemical Characters of the Lower Gondwana rocks of Chintpalapudi Sub-basin of the Godavari Valley of Andhra Pradesh. Ind. Mineral, 33, 151-168.

Rao. G. N., 1993. Geology and hydrocarbon prospects of east coast sedimentary basins of India with special reference to Krishna-Godavari Basin. J. Geol. Soc. India, 41, 444-454.

Rao, N. K., Swarna, L. P., Kumar, A. P. and Krishna, H. M., 2010. Morphometric analysis of Gostani River Basin in Andhra Pradesh State, India using spatial information technology. Int. J. Geomat. Geosci., 1(2), 179-187.

Rudraiah, M., Govindaiah, S. and Vittala, S.S., 2008. Morphometry using remote sensing and GIS techniques in the sub-basins of Kagna river basin, Gulburga district, Karnataka, India. J. Indian Soc. Remote Sens., 36, 351-360.

Sailaja. V., Reddy, K. S. N., Harsha., E. and Murthy. K., 2013. Textural Analysis and Depositional Environment of Sandstone of Kota Formation near Jangareddigudem, West Godavari District, Andhra Pradesh. Gond. Geol. Mag., 28(2), 141-148.

Schumm, S.A., 1956. Evolution of drainage systems and slopes in Badlands at Perth Amboy, New Jersey. Geol. Soc. Am. Bull.. 67, 597-646.

Shekar, P. R., Mathew, A., Abdo, H. G., Almohamad, H., Dughairi, A. A, and Al-Mutiry, M. 2023. Prioritizing sub-watersheds for soil erosion using geospatial techniques based on morphometric and hypsometric analysis: a case study of the Indian Wyra River basin. Appl. Water Sci., *13*(7), 160.

Smith, K. G. 1950. Standards for grading texture of erosional topography. Am. J. Sci.. 248, 655-668.

Sreedevi, P. D., Subrahmanyam, K. and Ahmed, S., 2005. Integrated approach for delineating potential zones to explore for groundwater in the Pageru River basin, Cuddapah District, Andhra Pradesh, India. Hydrogeol. J., 13(3), 534-543.

Strahler, A.N., 1952. Hypsometric analysis of erosional topography. Bull. Geol. Soc. Am., 63, 111.

Strahler, A.N., 1956. Quantitative Slope Analysis. Geol. Soc. Am. Bull., 67, 571-596. https://doi.org/10.1130/0016-7606(1956)67 [571: qsa]2.0.co;2

Strahler, A. N., 1957. Quantitative Analysis of Watershed Geomorphology, Eos. Trans. AGU, 38, 913-920.

Strahler, A. N., 1958. Dimensional analysis applied to fluvially eroded landforms. Geol. Soc. Am. Bull., 69, 279-300.

Strahler, A. N., 1964. Quantitative geomorphology of drainage and channel networks. Handbook of Applied Hydrology. (Ed. By Ven Te Chow) Me Graw Hill Book Company. New York. 4-39-4-76.

Tiwari, V.M. and Srinivas, N., 2023. Surface and groundwater studies in India during 2019-2022. J. Indian Geophys. Union, 27(5), 377-391.

Vijith, H., Prasannakumar, V., Krishnan, M. V. N. and Pratheesh, P., 2015. Morphotectonics of a small river basin in the South Indian granulite terrain: An assessment through spatially derived geomorphic indices. Geo. Ass. Man. Ris. Eng. Sys. Geo., 9(3), 187-199.

Vittala, S. S., Govindaih, S. and Gowda, H. H., 2004. Morphometric analysis of sub-watershed in the Pavada area of Tumkur district, South India, using remote sensing and GIS techniques. J. Indian Soc. Remote Sens., 32, 351-362.

Whipple, K.X. and Tucker, G.E., 1999. Dynamics of the stream□power river incision model: Implications for height limits of mountain ranges, landscape response timescales, and research needs. J. Geophys. Res., Solid, 104(8), 17661-17674.

Wobus, C., Crosby, B. T. and Whipple, K. X. 2006. Hanging valleys in fluvial systems: Controls on occurrence and implications for landscape evolution. J. Geophys. Res., 111. F02017.

Received on: 07-05-2024 ; Revised on: 23-08-2024; Accepted on: 04-09-2024

GUIDE FOR AUTHORS

The Journal of Indian Geophysical Union (JIGU), published bimonthly by the Indian Geophysical Union (IGU), is an inter disciplinary journal from India that publishes high-quality research in earth sciences with special emphasis on the topics pertaining to the Indian subcontinent and the surrounding Indian Ocean region. The journal covers several scientific disciplines related to the Earth sciences such as solid Earth geophysics, geology and geochemistry, apart from marine, atmosphere space and planetary sciences. J-IGU welcomes contributions under the following categories:

*Research articles, short notes and students section reporting new findings, results, etc.

*Review articles providing comprehensive overview of a significant research field.

In addition, JIGU also welcomes short communications, after communications and report on scientific activity, book reviews, news and views, etc.

The manuscript should be submitted electronically as a single word format (.doc file) including the main text, figures, tables, and any other supplementary information along with the signed "Declaration Letter". The manuscript should be submitted by email (jigul1963@ gmail.com) to the Chief Editor.

After acceptance of the manuscript the corresponding author would be required to submit all source files (text and Tables in word format) and figure in high resolution standard (*.jpg, *.tiff, *.bmp) format. These files may be submitted to JIGU as a single *.zip file along with the "Copyright Transfer Statement".

IMPORTANT INFORMATION

Ethics in publishing; J-IGU is committed to ensuring ethics in publication and takes a serious view of plagiarism including self-plagiarism in manuscripts submitted to the journal, Authors are advised to ensure ethical values by submitting only their original work and due acknowledgement to the work of others used in the manuscript. Authors must also refrain from submitting the same manuscript to more than one journal concurrently, or publish the same piece of research work in more than one journal, which is unethical and unacceptable. Editor of JIGU is committed to make every reasonable effort to investigate any allegations of plagiarism brought to his attention, as well as instances that come up during the peer review process and has full authority to retract any plagiarized publication from the journal and take appropriate action against such authors if it is proven that such a misconduct was intentional.

Similarly, Editor and Reviewers are also expected to follow ethical norms of publishing by ensuring that they don't use any unpublished information, communicated to them for editorial or review purpose, in their own research without the explicit written consent of the author. They are also expected to keep manuscript' data/ observations/ any other information related to the peer review confidential to protect the interest of the authors. Reviewers should refrain from reviewing the manuscripts in which they have conflicts of interest resulting from competitive, collaborative, or other relationships or connections with any of the authors, companies, or institutions connected to the manuscript.

Conflict of interest

All authors are requested to disclose any actual or potential conflict of interest including any financial, personal or other relationships with other people or organizations within three years of beginning the submitted nor that could inappropriately influence, or be perceived to influence, their work.

Submission declaration

Submission of a manuscript implies that the work has not been published previously and it is not under consideration for publication elsewhere, and that if accepted it will not be published elsewhere in the same or any other form, in English or in any other language, without the written consent of the publishers. It also implies that the authors have taken necessary approval from the competent authority of the institute/organization where the work was carried out.

Copyright

After acceptance of the manuscript the corresponding author would be required to sign and submit the "Copyright Transfer Statement".

MANUSCRIPT PREPARATION

The corresponding author should be identified (include E-mail address, Phone/Mobile number). Full affiliation and postal address must be given for all co-authors.

Abstract:

An abstract of not more than 300 words must be included.

Text:

The manuscript should be structured to include a front page containing the title, Author(s) name, affiliation and address of the institute, where the work was carried out, and 5-to-6 Key words. Author(s) present address, if different from the above mentioned address, may be given in the footnote. The corresponding author should be identified with an asterisk and his/her email ID should be provided. This page should be followed by the main text consisting of Abstract, Introduction, Methods/ Techniques/ Area description, Results, Discussion, Conclusions, Acknowledgements, and References. Tables and Figures with captions should be inserted at the end of main text. It should not be inserted in the body of the text.

Figures/ Illustrations:

figures should be provided in camera-ready form, suitable for reproduction (which may include reduction) without retouching. Figures in high-resolution (at least 300 dpi) standard formats (*.jpg, * tiff, *.bmp) are acceptable. Figures should be numbered according to their sequence in the text. References should be made in the text to each figure. Each figure should have a suitable caption.

Tables:

Authors should take note of the limitations set by the size and layout of the journal. Table should not exceed the printed area of the page. They should be typed on separate sheets and details about the tables should be given in the text. Heading should be brief. Large tables should be avoided and may be provided as supplementary information, if required.

Equations:

Equations should be numbered sequentially with Arabic numerals and cited in the text. Subscripts and Superscripts should be set off clearly.

Equation writing software that presents each equation as an object in MS Word will be accepted. Style and convention adopted for the equations should be uniform throughout the paper.

References:

All references to publications cited in the main text should be presented as a list of references in order following the text and all references in the list must be cited in the text. References should be arranged chronologically, in the text. The list of references should be arranged alphabetically at the end of the paper.

References should be given in the following form:

Kaila, K.L., Reddy PR., Mall D.M., Venkateswarlu, N., Krishna V.G. and Prasad, A.S.S.S.R.S., 1992, Crustal structure of the west Bengal el eon deep seismic sounding investigations. Geophys. J. Int., 1,45-66.

REVIEW PROCESS:

All manuscripts submitted to the journal are peer-reviewed. It is advisable to send the contact details of 4 potential reviewers along with the manuscript to expedite the review process. Editor has the option to select reviewers from the list or choose different reviewers. The review process usually takes about 3 months. All enquiries regarding the manuscript may be addressed to the Chief Editor.

GALLEY PROOF:

Technical editing of manuscripts is performed by the editorial board. The author is asked to check the galley proof for typographical errors and to answer queries from the editor. Authors are requested to return the corrected proof within two days of its receipt to ensure uninterrupted proceedings The editor will not accept new material in proof unless permission from the editorial board has been obtained for the addition of a "note added in proof". Authors are liable to be charged for excessive alterations to galley proof.

PUBLICATION CHARGES:

There are no page charges for publication. The corresponding author will receive a soft copy (pdf format) of his/her published article. Should the author desire to purchase reprints of his/her publication, he/she must send the duly signed Reprint Order Form (accompanies the galley proof and contains price details) along with the corrected galley proof to the Editor. The reprint charges must be paid within one month of sending the Reprint Order Form.

Any payment related to printing or purchase of reprints should be made in the form of a Demand Draft in the name of Treasurer, Indian Geophysical Union, payable at Hyderabad.

You may download the pdf file from:
http://iguonline.in/journal/instructions.php